

INVESTIGATING THERMO-FLUIDIC PERFORMAMNCE OF  
SI-BASED EMBEDDED MICROCHANNELS-3D MANIFOLD  
COOLING SYSTEM FOR HIGH POWER DENSITY  
ELECTRONIC APPLICATIONS

A DISSERTATION

SUBMITTED TO THE DEPARTMENT OF MECHANICAL ENGINEERING

AND THE COMMITTEE ON GRADUATE STUDIES

OF STANFORD UNIVERSITY

IN PARTIAL FULFILLMENT OF THE REQUIREMENTS

FOR THE DEGREE OF

DOCTOR OF PHILOSOPHY

Ki Wook Jung  
June 2020

© 2020 by Ki Wook Jung. All Rights Reserved.

Re-distributed by Stanford University under license with the author.



This work is licensed under a Creative Commons Attribution-Noncommercial 3.0 United States License.

<http://creativecommons.org/licenses/by-nc/3.0/us/>

This dissertation is online at: <http://purl.stanford.edu/zb171kw6421>

I certify that I have read this dissertation and that, in my opinion, it is fully adequate in scope and quality as a dissertation for the degree of Doctor of Philosophy.

**Kenneth Goodson, Primary Adviser**

I certify that I have read this dissertation and that, in my opinion, it is fully adequate in scope and quality as a dissertation for the degree of Doctor of Philosophy.

**Mehdi Asheghi**

I certify that I have read this dissertation and that, in my opinion, it is fully adequate in scope and quality as a dissertation for the degree of Doctor of Philosophy.

**Debbie Senesky**

Approved for the Stanford University Committee on Graduate Studies.

**Stacey F. Bent, Vice Provost for Graduate Education**

*This signature page was generated electronically upon submission of this dissertation in electronic format. An original signed hard copy of the signature page is on file in University Archives.*

# Abstract

High performance and economically viable cooling solutions must be developed to reduce weight and volume, allowing for a wide-spread utilization of hybrid electric vehicles. However, the continued drive for higher device and packaging densities has led to extreme heat fluxes on the order of  $1 \text{ kW/cm}^2$  that requires aggressive microchannel cooling strategies in order to maintain the device junction temperature  $\sim 200 \text{ }^\circ\text{C}$ . The traditional embedded microchannel cooling heat sinks suffer from high pressure drop due to small channel dimensions and long flow paths in 2D-plane. Utilizing direct “embedded cooling” strategy in combination with top access 3D-manifold strategy reduces the pressure drop by nearly an order of magnitude. In addition, it provides more temperature uniformity across large area chips and it is less prone to flow instability in two-phase boiling heat transfer.

This dissertation presents a series of studies to develop an effective microchannel-based heat exchanger with a fluid router system, the Embedded Microchannels-3D Manifold Cooler (or EMMC). The overall microfabrication efforts for the EMMCs are presented. The configuration of the target EMMC design is introduced and two major fabrication challenges are discussed.

For single-phase flow, thermo-fluidic behavior of the EMMC is experimentally examined and validated by a conjugate numerical simulation model. DI water and R-245fa are used as working fluids and the maximum heat transfer rate of  $100 \text{ kW/m}^2\text{-K}$  was measured with DI water. Furthermore, the conjugate numerical simulation modeling is heavily used to predict the geometric effect on the thermo-fluidic performance of different EMMCs and used to develop correlations to predict friction factor and Nusselt number of the system.

For two-phase flow, forced-convective subcooled boiling is confirmed by the experiments and a systematic trial to calculate exit vapor quality has been made based on a few assumptions. The highly pressurized subcooled boiling delays onset-of-nucleate boiling in the microchannels and this strong condensation effect allows the EMMC to remove higher heat fluxes with low void fraction inside of the channels.

The present research motivates further study into flow visualization and different types of boiling heat transfer. The better understanding to the underlying physics of the EMMC will be a key to develop more effective heat exchanger design for high-power density applications.

# Acknowledgements

I appreciate all the opportunities to pursue my graduate study at Stanford. There had been a lot of ups and downs during my graduate study and I am very grateful to arrive at this moment.

Through all these years, I have had failed many times during my graduate program. However, every fail that I made makes me stronger, tougher, and wiser at the end. Of course, I'm still making mistakes again and again, but people around me always give me their trust and wait for me. On this page, I'd like to give my special thanks to every single one of them in person.

I deeply appreciate what have been done by my wonderful two co-advisors in our group, Professor Kenneth E. Goodson, and Professor Mehdi Asheghi. I did not start my Ph.D. program at the Nanoheat group but joined the group back in late 2014. I was an apprentice researcher at that time, (some call it a rotation student, but I think that terminology is too young to explain my position at that moment), and I just started my new Ph.D. research at that time. Unfortunately, an unexpected medical leave stopped me from continuing my research for more than 6 months from early 2015 and I was doubtful of my future in the group. However, one email held me back up which is written here:

Ki Wook – you need to take care of your health first, this is the only priority. Glad to hear that there is no spreading, and I share your concern for the status of the original tumor in your shoulder. From my point of view a leave is not required.

Rest well as you handle these difficult treatments,

Ken

Sometimes people have to understand that even this short three-lines of letter can be your life saving boat in the middle of desperate ocean.

Professor Asheghi also expressed his trust many times, and that has been my biggest motivation to make all these hard works possible in the group. His academic intuition has been always a key to handle the problems and I really admire you for serving a guru in the group.

I also give my special love to my wife, Eunhae Park, for living with me for the last five years. We have been through all these difficult times together and will always be together in the world full of wonders. Also, I would like to thank to my parents, In-Sik Jung and Jung-Hee Ha, and my parents-in-law, Bong Cheol Park and Mija Kim, for supporting my works for all those years.

There have been a lot of wonderful people around me at Stanford and I would like to mention their names one-by-one to express my thanks: Tanya Liu, Hyoungsoon Lee, Chirag Kharangate, Heungdong Kwon, Sougata Hazra, Alisha Piazza, Chi Zhang, Chris Perez, Qianying Wu, Farid Soroush, Sangwook Park, and Hyun Jin Kim, you have been my best colleagues and I really appreciate your helps to finish my Ph.D. program.

Also, I'd like to thank my Ph.D. defense chair, Professor Roger T. Howe. He is always open and friendly to others. I haven't met him for a long time after taking his class, but he still remembered what I did during the class and he encouraged my works all the time. That really helped when I prepared my defense presentation. Also, I would like to express my thanks to other committee members, Professor Debbie Senesky, and Professor Juan G. Santiago to gratefully accept my invitation to the defense committee.

I would like to deliver my special thanks to Dr. Ercan M. Dede, and Dr. Feng Zhou, at Toyota Research Institute of North America, who had been working together for a few years. Eric has been always an amazing resource and I really appreciate his advice to the issues that I encountered. Feng is my cleanroom buddy back in 2017, and we struggled together at the LNF in the University of Michigan Ann Arbor. Sometimes I miss your sense of humor and appreciate your helps at that time.

Lastly, I would like to close my appreciation comments with these words:

May he give you the desire of your heart and make all your plans succeed.

[Psalm 20:4]

# Table of Contents

<b>Abstract.....</b>	<b>iv</b>
<b>Acknowledgements .....</b>	<b>vi</b>
<b>List of Tables .....</b>	<b>xi</b>
<b>List of Figures.....</b>	<b>xii</b>
<b>Chapter 1 Introduction.....</b>	<b>1</b>
1.1 Motivation and overview of current strategies .....	1
1.2 Description of dissertation .....	6
<b>Chapter 2 Fabrication of Si-based Embedded Microchannels-3D Manifold Coolers (EMMCs) .....</b>	<b>8</b>
2.1 Design of Embedded Microchannels-3D Manifold Cooler .....	8
2.2 Description of microfabrication process .....	12
2.3 Fabrication achievement 1: Double-sided anisotropic Si etching process.....	13
2.3 Fabrication achievement 2: Au-Si eutectic bonding .....	16
<b>Chapter 3 Experimental methodology .....</b>	<b>21</b>
3.1 Description of a closed-loop flow system.....	21
3.1.1 Hardware configuration .....	21
3.1.2 Software configuration.....	24
3.1.3 Test section configuration.....	25
3.2 Surface temperature measurement by Infra-red (IR) camera .....	29
<b>Chapter 4 Conjugate CFD simulations for single-phase study .....</b>	<b>31</b>
4.1 CFD simulation domains and boundary conditions.....	32
4.1.1 Description of Embedded Microchannels-3D Manifold Cooler (EMMC) design .....	32

4.1.2 Governing equations of CFD simulations.....	33
4.1.3 Computational domains and boundary conditions.....	34
4.1.4 Characterization of thermo-fluidic behavior of EMMCs.....	36
4.2 Results and discussion of parametric study in EMMCs .....	38
4.2.1 General guidelines for the EMMC design improvement.....	38
4.2.2 A summary of the parametric study in EMMCs.....	39
4.2.3 More detailed analyses of the parametric study of the EMMCs.....	40
<b>Chapter 5 Results and discussion .....</b>	<b>46</b>
5.1 Theoretical analysis for data reduction .....	46
5.2 Test results with EMMCs .....	49
5.2.1 Single-phase DI water.....	50
5.2.2 Single-phase R-245fa.....	71
5.2.3 Two-phase R-245fa.....	78
<b>Chapter 6 Conclusion and future works.....</b>	<b>86</b>
6.1 Summary of results and contributions to the field.....	86
6.2 Directions for future work .....	90
<b>Appendix A .....</b>	<b>93</b>
A.1 Experimental test conditions.....	93
A.2 Test conditions for conjugate CFD simulations.....	93
A.3 Mesh dependence study .....	94
A.4 Summarized CFD simulation results .....	96
<b>Appendix B .....</b>	<b>98</b>
B.1 Uncertainty study in EMMC .....	98
B.2 Onset-of-Nucleate Boiling study in EMMC .....	101
B.3 Estimation of pressure drop and its uncertainty in EMMC.....	103
<b>Appendix C .....</b>	<b>105</b>
C.1 Study of nonlinear Joule-heating effect .....	105
<b>Appendix D.....</b>	<b>107</b>

D.1 Mesh independence study of the conjugate numerical simulations .....	107
D.2 Additional information on Designs D4 to D9 .....	109
D.3 Discussion of thermo-fluidic behavior in D5 and D6 .....	110
D.4 Further discussion of frictional pressure drop in CP microchannels (D6 – D9)..	112
<b>Bibliography .....</b>	<b>113</b>

# List of Tables

<b>Table 2. 1</b>	Dimensions of structures in the cold-plate and the manifold.....	11
<b>Table 3. 1</b>	Sources of measurement uncertainties for data analysis.....	23
<b>Table 4. 1</b>	Geometry of different cold-plate designs.....	32
<b>Table 4. 2</b>	Geometry of different manifold designs .....	32
<b>Table 4. 3</b>	Simulation conditions.....	36
<b>Table 4. 4</b>	Key geometries and CFD results (D4/D5).....	42
<b>Table 4. 5</b>	Key CFD results (D5/D6) .....	42
<b>Table 4. 6</b>	Key CFD geometries and results (D6-D9).....	45
<b>Table 5. 1</b>	Previous friction factor correlations for rectangular ducts.....	62
<b>Table 5. 2</b>	Previous Nusselt number correlations for rectangular ducts.....	68
<b>Table 5. 3</b>	Gradual increase in the saturated fluid outlet temperature.....	72
<b>Table 5. 4</b>	Prandtl and Reynolds numbers, and thermal conductivity of R-245fa at given heat fluxes with 0.3 l/min flow rate .....	75
<b>Table 5. 5</b>	Rough estimation of fluid velocities and Reynolds numbers within the gradual contraction region at the constant heat flux of 100 W/cm <sup>2</sup> .....	77
<b>Table A. 1</b>	Experimental test conditions with single-phase DI water.....	93
<b>Table A. 2</b>	Experimental test conditions with single-/two-phase R-245fa .....	93
<b>Table A. 3</b>	Test matrix for the conjugate CFD simulations with single-phase DI water .	94
<b>Table A. 4</b>	Experimental test conditions with single-phase R-245fa.....	94
<b>Table A. 5</b>	Experimental test conditions with single-phase R-245fa.....	96
<b>Table A. 6</b>	Numerically predicted thermo-fluidic information in single-phase DI water test cases, $Q_{total,in} \leq 0.10$ l/min.....	97
<b>Table B. 1</b>	Sources to estimate the uncertainties of $\Delta P_{2,est}$ , $\Delta P_{3,est}$ .....	104
<b>Table D. 1</b>	Mesh independence study for different EMMC designs (D4, D7) .....	107
<b>Table D. 2</b>	Important input/output parameters for meshing.....	108
<b>Table D. 3</b>	Key CFD results (D4 – D9) .....	109

# List of Figures

**Figure 1. 1** Chronological changing trend in commercial CPUs’ computation capability and power dissipation rate [1]..... 1

**Figure 1. 2** One of the schematic from US Patent 7,000,684, by Goodson, et al. [33,34], Kenny, et al. [35], illustrating distributed manifolding for a microchannel heat sink. This patent was the basis for commercialized chip-normal fluid routing..... 3

**Figure 2. 1** Conceptual design of an Embedded Microchannel-3D Manifold (EMMC), (a) representation of the fluid flow pattern inside the EMMC, (b) a SEM image of cross-sectional view of the actual EMMC device ..... 9

**Figure 2. 2** Geometric parameters of microfeatures, (a) Ti/Au serpentine heater with RTDs are placed on a  $5 \times 5 \text{ mm}^2$  center area of the cold plate. RTDs are diagonally placed in between the heater lines and only RTD5, 6, 7, and 9 (highlighted) were used for actual temperature measurement. Measured temperature coefficient of resistance (TCR) of RTDs was  $3.1 - 3.3 \times 10^{-3} \text{ }^\circ\text{C}^{-1}$  and the thicknesses of the heater and the RTD are 500 nm, and 50 – 55 nm, respectively. A closed-loop flow system is used for RTD calibration by varying the temperature of the liquid and recording corresponding electrical resistance for individual RTDs (b) & (c) Design of various anisotropically etched structures in (b) the cold plate and (c) the manifold, see Table 5.1 for geometry details. A set of pin fin arrays at the entrance and exit plenums are utilized to create uniform flow distribution. 10

**Figure 2. 3** Overall microfabrication process of the embedded microchannel-3D manifold cooler. *Step 1*: double-polished Si substrates with thickness of 500  $\mu\text{m}$ , and 1000  $\mu\text{m}$  were prepared for the cold plate and the 3D manifold structures, respectively. *Step 2*: Microchannels and other microscale features were anisotropically etched in the cold plate and the 3D manifold substrates. Double-sided anisotropic Si etch technique was used to define the microstructures with different etch depth in the 3D manifold. *Step 3*: Au-Si eutectic bond layers were deposited on the cold plate and the 3D manifold substrates. Ti/Au layer thickness on each substrate is denoted in Figure 2. As the Ti layer on the cold plate functioned as a native oxide getter, Au-Si eutectic reaction was

activated from the cold plate surface. 720 nm of SiO<sub>2</sub> layer on the manifold substrate insulated Si from the Au layer and it helps to induce better Au-Si eutectic reaction [68].

*Step 4:* A serpentine heater and RTDs were deposited on top of Si<sub>x</sub>N<sub>y</sub>/SiO<sub>2</sub> electric passivation layer. Since Ti reacts with SiO<sub>2</sub> at high temperatures, it is recommended to deposit a thin Si<sub>x</sub>N<sub>y</sub> layer between Ti and SiO<sub>2</sub> layers to prevent further reaction ..... 12

**Figure 2. 4** (a) The overall double-sided anistropic Si etching process to fabricate manifold structures, masking-frontside etch-masking-backside etch steps are depicted, (b) timelapse images captured during the backside Si etch, (c) a finished microchannels-3D manifold sample in SEM, yellow etch stop line consists of 200-300 nm Al sputtered after the frontside etch..... 14

**Figure 2. 5** One of the finished manifold substrates, the dimensions of inlet and outlet conduit are checked under microscope and the measured dimensions are almost identical to the target values, see Table 2.1. .... 16

**Figure 2. 6** Head-to-head comparison of different bonding strategies (green: good, red: bad) [67]..... 17

**Figure 2. 7** The characterized Au-Si eutectic bonding recipe..... 17

**Figure 2. 8** (a) SEM images from Ref. [68], and (b) from earlier Au-Si eutectic bonding trials. Si precipitates are recognized in the Au layer in both cases..... 19

**Figure 2. 9** (Left) A bonded wafer pair after Au-Si eutectic bonding, (middle) aligned microstructures in the cold-plate and the manifold, (right) sealed interfaces by Au-Si eutectic alloy ..... 19

**Figure 3. 1** A depiction of the closed-loop flow system that uses single-phase DI water as the working fluid for the current experiments ..... 22

**Figure 3. 2** The user interface for the flow loop operation programmed by the Labview, (a) the flow loop schematic with a separate panel to control the flow rate, (b) & (c) another options to monitor temperature and pressure at various locations in the loop..... 24

**Figure 3. 3** A captured PI feedback control subfunction programmed by the Labview. . 25

**Figure 3. 4** (a) & (b) A cross-sectional view of an assembled test, and (c) an image of the assembled test section. (1) Power supply lines, (2) 5 mm-by-5 mm heated region in the sample, (3) Au electrode pads that are connected to RTDs, (4) Swagelok fittings for inlet and exit pressure read-outs..... 26

**Figure 3. 5** (a) A new sample holder schematic drawn by Solidworks2018, and the actual holder setup in comparison, (b) the actual test section with other experimental components. .... 27

**Figure 3. 6** A schematic of electric circuitry to measure electric power dissipated by the heater..... 28

**Figure 3. 7** Description of the IR calibration procedure, (a) conceptual image of the IR measurement setup, (b) determination of the emissivity of the black body, emissivity of 0.95 performs best among others, (c) typical IR images showing surface temperature distribution of the heated surface from perspective and top views for 298 W/cm<sup>2</sup>, single-phase R-245fa at flow rate of 0.37 l/min, the maximum and average heat temperatures are 80.5 °C and 69.5 °C, respectively ..... 30

**Figure 4. 1** (a) Conceptual design of the embedded microchannels-3D manifold cooler (EMMC), (b) key geometric parameters of cold-plate and manifold in A-A' and B-B' cut views ..... 33

**Figure 4. 2** Full scale chip and a quarter-cut solid and fluid domains for conjugate CFD simulations..... 35

**Figure 4. 3** The fluid domain used in CFD simulations is divide into four discrete regions. **zone 0**: semicircular open area where the fluid is introduced to the device, **zone 1**: regions right after the inlet plenum where the gradual contraction begins, **zone 2**: regions right before the active cooling area where the gradual contraction is ended, **zone 3**: open-ends of the manifold outlet conduits that are connected to the exit plenum, **zone 4**: square open area where the fluid exits from the device. .... 35

**Figure 4. 4** Comosition of each thermal resistance component in the baseline EMMC design, D4 ..... 38

**Figure 4. 5** A summarized conjugate CFD simulation results to show the design improvement process by plotting data in average surface temperatures and corresponding thermal resistances vs.  $\Delta P_{total}$ . Effect of symmetric distribution of manifold inlet/outlet conduits (1), effect of CP thickness (2), effect of fluid-solid interfacial area in cold-plate microchannels (3 – 5) are studied in the following sections. Also see Appendix D.2, Table D.3 for more details for designs D4 to D9..... 40

**Figure 4. 6** Pressure drop and thermal resistance vs.  $W_{mani,wall}/L_{flow}$  results (D4/D5). .... 41

**Figure 4. 7** Thermal resistance vs.  $H_{cp,sub}$  (D5/D6) ..... 43

**Figure 4. 8** Thermal resistance and pressure drop vs.  $N_{cp}$  (D6/D7, D7/D8/D9) ..... 44

**Figure 5. 1** The experimental data and numerical simulation results for (a)  $T_{heat,max}$  or  $T_{heat,avg}$  vs.  $\Delta P_{total}$ , for the highest flow rate and heat flux of 0.1 l/min and 250 W/cm<sup>2</sup>, respectively; dimensions for the microchannel and 3D-manifold conduits are listed in Table 2.1. The uncertainty in pressure drop from simulations, is mainly associated with variations of the microfabricated channel dimensions. The numerical values of the maximum and average temperatures, flow rate, pressure drop for the 9 test cases are listed in Table A.5, (b) maximum surface temperature vs. heat flux for flow rates 0.03, 0.07 & 0.1 l/min. The “semi-transparent” red region, flow rate 0.03 l/min, represents  $\pm 10$  % uncertainty levels in CFD predictions associated with variations in  $\mu$ -cooler channel and manifold conduits dimensions. .... 50

**Figure 5. 2** The experimental data and numerical simulation results for (a)  $T_{heat,max}$  or  $T_{heat,avg}$  vs.  $\Delta P_{total}$ , for the flow rates from 200 to 400 g/min, at the supplied heat flux of 800 W/cm<sup>2</sup>. Two semi-transparent polygons filled with semi-transparent red and orange colors are estimated temperature and pressure drop results by CFD, (b)  $T_{heat,max}$ ,  $T_{heat,avg}$ ,  $T_{f,ref}$  vs.  $q$ ” for the flow rates from 200 to 400 g/min, dotted lines represent the estimated  $T_{heat,max}$ ,  $T_{heat,avg}$ ,  $T_{f,ref}$  as a function of  $q$ ”. .... 51

**Figure 5. 3** Captured thermal images from the IR camera and the CFD simulations. The thermal images from the CFD simulations are quarter-cut due to the defined CFD simulation domains. In general, temperature uniformity across the hotspot improves with the increased flow rate due to enhanced heat transfer rate. (a) At the heat flux of 300 W/cm<sup>2</sup>, temperature distribution in the IR images and the CFD images is almost identical (confirmed in Figure 5.2b). However, (b) more intensive and wider local hotspots are appearing at the heat flux of 900 W/cm<sup>2</sup> with flow rates of 200 and 300 g/min in the IR images. .... 52

**Figure 5. 4** Experimental data and predictions for (a)  $R_{total}$  &  $R_{adv}$  vs. Flow Rate, and pressure drop for single-phase water at heat flux of 250 W/cm<sup>2</sup>. (b) As expected, there is no significant change in  $R_{total}$  as the supplied heat flux increased from 60 to 250 W/cm<sup>2</sup> for a given flow rate. .... 54

**Figure 5. 5** The change in thermal resistances plotted as a function of  $q''$ , reduction in  $R_{total}$  due to the increased flow rate is 15 - 21 %, despite the flow rate is doubled from 200 to 400 g/min. Dotted lines are thermal resistances from the CFD data. .... 55

**Figure 5. 6** Summarized total thermal resistances as a function of total pressure drop at 100 W/cm<sup>2</sup>. Six different flow rates, from 0.03 to 0.4 l/min, are used. .... 56

**Figure 5. 7** The measured and simulated results for heat transfer coefficients at the cold-plate microchannel walls,  $h_{effect}$ . (a) The  $h_{effect}$  vs. flow rate for various heat fluxes, and (b) the  $h_{effect}$  vs. heat flux for various flow rates..... 57

**Figure 5. 8** Summary of  $h_{effect}$  vs.  $q''$  for the flow rate from 0.03 to 0.4 l/min..... 57

**Figure 5. 9** Results of the CFD simulations for pressure loss in the channel and 3D manifold: (a) relative contributions of pressure drop components:  $\Delta P_{plenum}$  (or  $\Delta P_1$ ),  $\Delta P_{contraction}$  (or  $\Delta P_2$ ),  $\Delta P_{friction}$  (or  $\Delta P_3$ ), and  $\Delta P_{expansion}$  (or  $\Delta P_4$ ) over the total pressure drop at  $Q_{total,in} = 100$  g/min, (b) schematics of the inlet, microchannel and outlet of the  $\mu$ -cooler, (c) experimental and numerical simulation results for  $\Delta P_{total}$  vs. Flow Rate at a nominal heat flux of  $q'' = 250$  W/cm<sup>2</sup>. .... 59

**Figure 5. 10** (a)  $\Delta P_{total}$  vs.  $Q_{total,in}$  at a heat flux of 900 W/cm<sup>2</sup>,  $\Delta P_{total,EXP}$  is compared to  $\Delta P_{total,CFD}$  and agrees well with the estimation within the uncertainty, (b) composition of  $\Delta P_2$  and  $\Delta P_3$  to  $\Delta P_{total}$  is estimated by CFD simulations. Based on the simulation results, about 55 % of pressure drop occurs in the gradual contraction region, and microchannels under the hotspot is responsible for ~ 40 % of  $\Delta P_{total}$ . .... 60

**Figure 5. 11** (a) Visualized pressure gradient in a quarter-cut EMMC CFD domain, showing inlet plenum, two converging sections, and inlet/outlet conduits, (b) visualized internal fluid flow pattern with arrow head vectors; A-A': at the interface between inlet/outlet conduits and a microchannel, the fluid is diverged and flows through the microchannel, and exits through the adjacent outlet conduit, B-B': after the fluid passes Zone 2, the fluid keeps diverging whenever it encounters adjacent CP microchannel, from Ch1 through Ch13. Ch 13 is the channel located at the very center of the EMMC, thus no further fluid flow is allowed after this point. .... 61

**Figure 5. 12** (a) Average velocity and Reynolds number profiles in every defined zone in the CFD domains, (b) normalized velocity profile in each channel in Zone 3. .... 63

**Figure 5. 13** Friction factor vs.  $Re_{CFD}$  in various heat fluxes for the comparison purpose. For the developing flow, hydrodynamic entrance length is considered in the correlations [58, 59]. ..... 64

**Figure 5. 14** Poiseuille number vs. hydrodynamic entrance length plotted in log-log scale. The entrance length,  $x^+ = L_{unit} Re \cdot Dh$ , is calculated in each segmented microchannel,  $f_{CFD}$  and  $Re_{CFD}$  are given from the CFD simulation results. .... 65

**Figure 5. 15** Friction factors predicted by the existing correlations and a newly developed correlation vs.  $f_{CFD}$  for four different heat flux cases. .... 66

**Figure 5. 16** (a) Predicted  $\Delta P_{total}$  by the new correlation plotted as a function of  $Re_{CFD}$  and a function of  $\Delta P_{total,CFD}$  for heat fluxes of  $800 \text{ W/cm}^2$ , (b) comparison between  $\Delta P_{total,EXP}$  and  $\Delta P_{total,CFD}$  at the heat fluxes of  $200/400/800 \text{ W/cm}^2$  ..... 67

**Figure 5. 17** (a) Local Nusselt number vs. dimensionless axial distance for the thermal entrance region,  $x^*$ , (b) predicted average Nusselt numbers against the average Nusselt number from the CFD simulation. Figure only shows one CFD simulation case,  $q'' = 800 \text{ W/cm}^2$ ,  $Q_{total,in} = 200 \text{ g/min}$ . .... 69

**Figure 5. 18** (a) Mean Nu vs.  $Re_{CFD}$ , the predicted mean Nu from the existing correlations are compared with average Nu from the CFD simulations, (b) Mean  $Nu/Pr^{1/3}$  vs.  $Re_{CFD}$  in log-log scale..... 69

**Figure 5. 19** Summary of the predicted Nu and measured Nu vs.  $Nu_{CFD}$  for all test cases with single-phase DI water. .... 70

**Figure 5. 20** Experimental results, (a)  $T_{heat,avg}$  vs.  $\Delta P_{total}$ , the supplied heat and the fluid flow rate are up to  $300 \text{ W/cm}^2$  and  $0.37 \text{ l/min}$ , respectively, (b) measured temperatures vs. supplied heat flux at a given flow rate of  $0.3 \text{ l/min}$ , open marker represents the ONB or two-phase regime (see Appendix B.2 for details)..... 71

**Figure 5. 21** Behavior of total thermal resistance as the flow rate changes and the supplied heat flux changes is presented by  $R_{total}$  vs.  $Q_{total,in}$ . Numbers next to the markers are  $T_{heat,avg}$  ..... 73

**Figure 5. 22** Behavior of total thermal resistance as the flow rate changes and the supplied heat flux changes is presented by  $R_{total}$  vs.  $Q_{total,in}$ . Numbers next to the markers are  $T_{heat,avg}$  ..... 74

<b>Figure 5. 23</b> The measured HTC at the cold-plate microchannel walls vs. flow rate, the overall fin efficiency is from 98.4 to 99.4 % .....	75
<b>Figure 5. 24</b> Pressure drop results from the experiments are compared with the conjugate CFD simulation results. The total pressure drops from the CFD simulations are within the error of the total pressure drops from the experiments. (a) Pressure drops vs. flow rate at a constant heat flux of 100 W/cm <sup>2</sup> . (b) The total pressure drop results are plotted as a function of supplied heat flux. Since the tested fluidic flow is single-phase, change in the total pressure drop is less than 4 % .....	76
<b>Figure 5. 25</b> Total pressure drop vs. supplied heat flux. The void markers indicate that the flow regime is changed to two-phase. Inlet pressure is between 254 – 283 kPa. ....	77
<b>Figure 5. 26</b> A schematic to explain the energy balance model for single-/two-phase heat transfer. ....	78
<b>Figure 5. 27</b> (a) Exit quality vs. heat flux for the flow rates from 0.1 to 0.37 l/min, (b) generated vapor flow rate at the outlet vs. exit quality. ....	80
<b>Figure 5. 28</b> Temperature behavior against the supplied heat fluxes for the flow rate of 0.37 l/min, IR images taken at the ONB and at the highest heat flux, respectively .....	80
<b>Figure 5. 29</b> Summarized $T_{\text{heat,avg}}$ vs. $Q_{\text{total,in}}$ with an ONB estimation line. Colored markers represent single-phase, and empty markers represent two-phase. ....	81
<b>Figure 5. 30</b> Summarized $R_{\text{total,avg}}$ vs. $\Delta P_{\text{total}}$ for various heat fluxes from 50 W/cm <sup>2</sup> to 600 W/cm <sup>2</sup> . ....	82
<b>Figure 5. 31</b> $R_{\text{total,avg}}$ vs. $\Delta P_{\text{total}}$ at a given flow rate from (a) 0.1 to (b) 0.2 to (c) 0.3 to (d) 0.37 l/min. Supplied heat flux and exit vapor quality values are written next to the two-phase markers.....	83
<b>Figure 5. 32</b> (a) The $h_{\text{effect}}$ as a function of heat flux, and (b) the $h_{\text{effect}}$ as a function of $x_{\text{exit}}$ . Four different flow rates are tested in single and two-phase regime. ....	84
<b>Figure 5. 33</b> (a) The $\Delta P_{\text{total}}$ as a function of heat flux, and (b) normalized $\Delta P_{\text{total}}$ as a function of $x_{\text{exit}}$ .....	85
<b>Figure 6. 1</b> Configurations of three different cooling strategies. (a, a') <b>Design A</b> : cross-sectional views and associated thermal resistance components, (b, b') <b>Design B</b> : cross-sectional views and associated thermal resistance components; (c, c', c'') <b>Design C</b> : explains embedded cooling with 3D manifold concept, direction of flow from 3D-	

manifold inlet to channel inlet, traversing channel length, moving out of the channel and entering the outlet of 3D-manifold. Also, thermal resistance components are included. . 87

**Figure 6. 2** Sample designs for manufacturability test, the minimum wall thickness dimension used in each design is 200/300/500  $\mu\text{m}$ , respectively. .... 91

**Figure A. 1** A study of mesh element independence at  $T_{f,in} = 293 \text{ K}$ ,  $Q_{total,in} = 0.001 \text{ kg/s}$ ,  $q'' = 4,494,517 \text{ W/m}^2$  conditions. The number of mesh elements used in the study are from 1.11E6 to 3.19E6 to 5.40E6 to 1.09E7..... 95

**Figure A. 2** A study of mesh element independence at  $T_{f,in} = 293.15 \text{ K}$ ,  $Q_{total,in} = 5.0 - 6.67\text{E-}3 \text{ kg/s}$ ,  $q'' = 14,703,889 - 16,296,666 \text{ W/m}^2$  conditions. The number of mesh elements used in the study are from 3.27E6 to 1.42E7..... 95

**Figure A. 3** Summarized heater temperatures and pressure drop results for the mesh independence study. The results are plotted as a function of the mesh elements. The results with more than 25 millions of mesh elements show good simulation convergence,  $< 0.6 \%$ ..... 96

**Figure B. 1** (a) A simplified heat conduction pathway in the embedded microchannel with 3-D manifold heat exchanger and (b) Temperature vs  $P_{out}$  for single-phase water test case at the maximum heat flux  $250 \text{ W/cm}^2$ . .... 102

**Figure B. 2** Experimental data and CFD modeling results for single-phase water at inlet temperature  $\sim 25^\circ \text{C}$  using a typical embedded microchannel with 3D manifold  $\mu$ -cooler developed at Stanford. The experimental data are for heat flux  $< 250 \text{ W/cm}^2$ . The CFD simulations are conducted to explore the feasibility of single-phase cooling at much higher heat fluxes; the onset of boiling occurs at  $850 \text{ W/cm}^2$  to be verified experimentally. For water at inlet temperature of  $25^\circ \text{C}$ , heat dissipation levels up to  $500 \text{ W/cm}^2$  is feasible for target junction temperature of  $100^\circ \text{C}$ . .... 102

**Figure B. 3** Estimation of onset-of-nucleate boiling points for each test case, ONB estimation vs. supplied heat flux at given flow rates. The dashed line indicates the threshold for ONB by the correlation [ONB\_REF] and the open markers designate the empirically captured ONB moments. .... 103

**Figure C. 1** Comparison between Joule-heating case vs. uniform heating case, natural convection is assumed on top surface, forced convection with  $HTC = 100 \text{ kW/m}^2\text{-K}$  is assumed at the bottom surface of the hotspot. .... 105

**Figure C. 2** Comparison between Joule-heating case vs. uniform heating case, natural convection is assumed on top surface, forced convection with  $HTC = 100 \text{ kW/m}^2\text{-K}$  is assumed at the bottom surface of the hotspot. .... 106

**Figure D. 1** Temperature distributions at the top of the micro-cooler (quarter) designs D4 and D9. .... 109

# Chapter 1

## Introduction

### 1.1 Motivation and overview of current strategies

An increased power density for wide-bandgap (WBG) transistors for power electronics application poses a significant challenge in terms of device performance and reliability. As shown in Figure 1.1, as the lithography technique has been advanced over decades, the computation capability per processor has been improved exponentially. At the same time, the similar changing trend is recognized in power dissipation per processor and it becomes a main hurdle to improve the computation capability of processors.

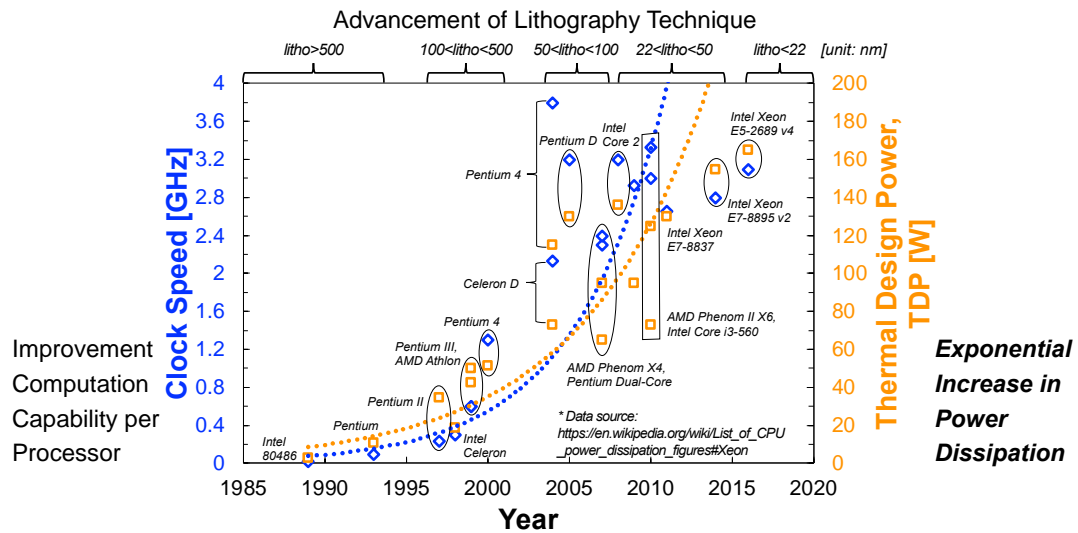


**Figure 1. 1** Chronological changing trend in commercial CPUs’ computation capability and power dissipation rate [1]

Thermal-power bottlenecks and constraints have given rise to serious threats to the historical rate of increase in processor performance [2], meanwhile, the advent of energy-

efficient computing and heterogeneous integration [3,4] offer considerable reduction in computational energy. These two conflicting trends have resulted in a substantial increase in both heat flux and power density ( $\text{W}/\text{cm}^3$ ), that requires highly integrated embedded cooling strategies capable of removing heat fluxes  $\sim 1 \text{ kW}/\text{cm}^2$  at a junction temperature  $\sim 100 \text{ }^\circ\text{C}$ .

Traditionally, single phase cold-plate microchannels dissipate heat fluxes up to  $300 \text{ W}/\text{cm}^2$  [5,6], however at higher heat fluxes, two-phase flow cooling strategies become more relevant. Two-phase flows take the advantage of sensible and latent heat of the fluid to achieve very high heat transfer coefficients up to  $150 \text{ kW}/\text{m}^2\text{-K}$  [7-13]. But, the extremely high heat transfer needs in current semiconductor applications require utilization of micro-channel flows [14-21], which provide very high heat transfer coefficients even higher than traditional two-phase schemes [12,16,22,23].

Efforts to minimize both the thermal resistance and pressure drop in dimensionally-scaled heat exchangers date back for many decades. This challenge was, quite arguably, first articulated into a comprehensive discipline of mechanical engineering practice by Kays & London [24] at Stanford University. While this work was primarily for two-fluid heat exchange, in many cases with a gas as one working fluid, many of the manifolding and hydraulic routing concepts quantified in that text have found their way into heat sink design. At roughly the same time, the scaling of compact heat sinks from the milliscale [25] to the microscale regime was being pursued by Stanford electrical engineers Tuckerman & Pease [26], who cooled  $\sim 800 \text{ W}/\text{cm}^2$  through the use of chip-length microchannels and a relatively large pressure drop up to 215 kPa. The next two decades brought a great quantity of microchannel research, primarily on two-phase convective boiling [27], which illustrated numerous challenges associated with long channels including Ledinegg instabilities, flow regime oscillation, and dryout/hotspots for the case of controlled heat generation distribution [28].

The large body of work on chip-length two-phase micro-channels was neither stabilizing nor reducing the pressure drop associated with high heat flux cooling, in part due to the lack of integration of older fluid manifolding and routing concepts. A series of theoretical papers started to address the fluid routing challenge, either through tree-like or

fractal-based networks [29-31] or through the more practical force-fed staged manifolding approach from U. Maryland [32]. The principle of these improvements was – in contrast to the earlier chip-length microchannels – to limit the axial lengthscale over which fluid must traverse the narrowest regions (with low hydraulic diameter) of the heat exchanger. This minimizes the pressure drop exerted by the small hydraulic diameter while still allowing the associated high heat transfer coefficients. All of the academic papers cited in this paragraph share the common feature of chip normal, or 3D, fluid routing with manifolding from the backside rather than the ends of the heat sink, which is conventional routing implemented in microchannel design.

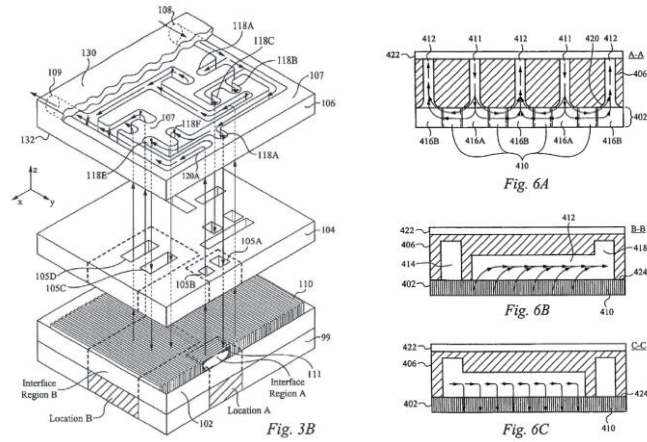


**Figure 1. 2** One of the schematic from US Patent 7,000,684, by Goodson, et al. [33,34], Kenny, et al. [35], illustrating distributed manifolding for a microchannel heat sink. This patent was the basis for commercialized chip-normal fluid routing.

Some papers cited in the previous paragraph may very well have been written using the Apple G5 workstation, which in 2005/2006 featured a microfluidic heat sink with these features. This novel heat sink was developed and commercialized by Cooligy, a Stanford startup company founded by Profs. Kenny, Santiago, and Goodson based on earlier DARPA HERETIC funding of their programs. Stanford and Cooligy submitted a series of patents in the 2003-2004 timeframe featuring distributed, chip-normal fluid routing to a microfluidic heat exchange region, which could take the form of either microchannels, distributed microscale pin fins, or microporous foam (Figure 1.2) [33-36]. This industrial advancement in fluid routing methodology, commercialized in parallel with the academic papers cited above, was essential for Cooligy to achieve a winning product considering both pressure drop and thermal resistance.

Lee, et al. [37] conducted single/two phase CFD modeling of SiC embedded cooling microchannels ( $D_h \sim 20 \mu\text{m}$ ) at extreme heat flux  $30 \text{ kW/cm}^2$  or GaN-based high electron mobile transistors (HEMTs). The developed methods in this paper are useful to approximate the most vulnerable locations for dryout regions, and, therefore, it is possible to optimize the design of the microcoolers for the extreme heat flux application.

A combination of microchannels with 3D manifold routing (vertical liquid delivery and distribution scheme) has been proposed to overcome the large pressure drop in conventional lateral liquid feeding approach [38-43]. This approach is preferred because the smaller hydraulic diameter yields improved thermal performance, however, the out-of-plane liquid delivery to each channel results in shorter paths for liquid, thus reducing the pressure drop compared to the conventional microchannel heat exchangers. Drummond, et al. [38,39] developed and tested a microchannel heat exchanger with multi-layer hierarchical manifolds using R-245fa that removed heat flux up to  $\sim 1 \text{ kW/cm}^2$  with thermal resistance of  $0.07 \text{ cm}^2\text{-K/W}$ , and pressure drop from 50 to 120 kPa [39] for two-phase heat transfer. Cetegen [40] also utilized a similar heat exchanger architecture, called Forced-Fed Microchannel Heat Sink (FFMHS), using R-245fa as the working fluid. The cooling performance of the optimized FFMHS was 72 % and 306 % more effective than Traditional Microchannel Heat Sinks (TMHS), and Jet Impingement Heat Sinks (JIHS), respectively. The maximum heat flux removable from the module was  $\sim 1.2 \text{ kW/cm}^2$  with the thermal resistance of  $0.06 \text{ cm}^2\text{-K/W}$ . The reported pressure drop ranged from a few kPa's to 60 kPa for two-phase cooling. Zhou, et al. [42] from Toyota Research Institute of North America tested two chip-scale cooling devices, a straight microchannel cooler and a unit cell microchannel with jet impingement cooler, in single-phase water. The unit cell microchannel device removed the maximum heat flux of  $1.02 \text{ kW/cm}^2$  with a measured pressure drop of 41.2 kPa, which showed superior thermal-fluidic performance to the straight microchannel device.

Unfortunately, using straight microchannel correlations for design and optimization of the embedded microchannels-3D manifold coolers (or EMMCs) turned out to be very inaccurate [44] due to the complexity of the flow patterns in the cold-plate and the impact of the 3D-manifold conduits geometry and form factor. Therefore, the computational fluid dynamics (CFD) simulations is the preferred approach and have been conducted

both for a unit cell U-shape cold-plate passage and for a full-scale analysis of the entire EMMC. The unit cell analysis is cost-effective but this method is more accurate if the symmetry and periodicity conditions are satisfied in the CFD domains [45-47]. Andhare, et al. [48], performed single-unit cell simulations for a flat-plate, manifold microchannel heat exchanger. Arie, et al. [49], introduced a hybrid computational method, a single manifold-microchannel model, for the same heat exchanger used in [48]. The computational results from both papers showed reasonably good agreement with the experimental data with the reduced computational time and cost [48-49].

Many researchers also reported a porous-medium modeling to understand the performance of various heat sink designs due to its feasibility for entire heat sink analysis [50-53]. According to these papers, the porous-medium approach is more suitable for complex and realistic thermal management applications than a unit-cell model which only takes into account for a single microchannel under assumptions of periodicity, and symmetry [50-53]. Sarangi, et al. [53], reported two computational methods, a simple unit-cell model and a porous-medium model, to determine a manifold microchannel heat sink design to achieve optimal heat transfer performance. Two most interesting outputs, heat transfer coefficient and pressure drop, were validated by these models in various test cases, and the porous medium model showed good cost-effectiveness and desired reliability in system-level geometry optimization [53].

Solovitz and Mainka [54] proposed an optimized power law model for a manifold shape to avoid non-uniform distribution of the fluid flow in their multi-channel cooling system. The proposed analytic model was validated by a series of full-scale CFD simulations with fully-developed, laminar flow conditions [54]. With the varying Reynolds numbers from 5 to 500, the optimal manifold design showed a standard deviation of less than 3% of the overall mean channel speed [54].

The full-scale CFD analysis is less sensitive to periodicity and symmetry conditions, and it is advantageous to analyze local and global thermo-fluidic behavior of complicated structures such as EMMCs. Despite of its expensive computational cost, the full-scale, conjugate CFD simulations for single-phase coolants in EMMCs have been validated by experimental test results [43,55,56] with good reliability. In a separate study, we have

also conducted CFD simulation on uniform heating of small (5 mm x 5 mm) and large (20 mm x 20 mm) footprint micro-coolers, and compared it to unit cell results. It is concluded that the error for small footprint micro-cooler could be as large as 12%, therefore, we will proceed with the full-scale chip CFD simulations for parametric study of different EMMCs designs.

## **1.2 Description of dissertation**

Despite thermofluidic behavior of various EMMCs have been studied by many researchers, a broad understanding of the microfluidic behavior, underlying physics, and limitations to optimize the thermofluidic performance of EMMC are not well understood. Therefore, the goal of my work is to develop a novel EMMC design and perform microfluidic heat transfer experiments to understand thermofluidic behavior of the developed EMMC.

In this dissertation, my journey to achieve this objective is described one by one.

In Chapter 2, I present overall microfabrication efforts for the EMMCs. The entire microfabrication process is explained step-by-step, followed by two major fabrication challenges. The configuration of the target EMMC design is introduced, and the subsequent sections highlight how the non-conventional fabrication processes are dealt with the conventional fabrication technique.

In Chapter 3, I present the overall configuration of the experimental system in three aspects: hardware, software and test section. The functional requirements for the heat transfer experiments are satisfied with the system upgrades, including installation of an electric circuitry to measure supplied electric power, adding an immersion heater to the customized liquid reservoir to remove non-condensable gas components, implementation of a PI feedback control in the operating program for an accurate control over the flow rate, construction of a new sample holder system with metal frames for the IR measurement setup.

In Chapter 4, I present parametric study of various EMMCs to improve thermofluidic performance at high heat flux condition. Full-scale CFD simulation is performed with

quarter-cut EMMC designs. In Section 4.1, the CFD simulation domains and boundary conditions are explained. The governing equations and boundary conditions of the CFD domains are described and the method to characterize thermofluidic performance of the EMMCs is followed. In Section 4.2, three main approaches to improve the cooling performance yet minimize the pressure drop are proposed: modifying inlet/outlet conduits, reducing cold-plate substrate thickness, and increasing the effective cold-plate microchannel area.

In Chapter 5, I present hydraulic and thermal behavior of the proposed EMMC design with single and two-phase DI water/R-245fa. In Section 5.1, I introduce the analytic tools to interpret the experimental data to understand thermofluidic performance of the EMMCs. In Section 5.2, thermo-fluidic performance of the tested EMMCs with DI water and R-245fa is investigated. For single-phase flow, conjugate CFD simulations are used to validate the experimental data. A parametric study of the developed correlations [57-61] is conducted to understand how the thermo-fluidic performance of the EMMCs. Furthermore, I propose new correlations to predict friction factors and Nusselt numbers of the tested heat exchangers by the parametric study of the conjugate CFD simulations. For two-phase flow, forced-convective subcooled boiling is confirmed by checking experimental data. Thus, change in thermo-fluidic behavior of the EMMCs by exit vapor quality is studied with the given flow regime.

The lessons after this work will broaden our understanding of the hydraulic and thermal behavior of the EMMCs. Furthermore, more effective single-phase and two-phase heat exchangers can be developed by changing geometric dimensions or hydraulic or thermal operating conditions.

## **Chapter 2**

# **Fabrication of Si-based Embedded Microchannels-3D Manifold Coolers (EMMCs)**

This chapter describes overall microfabrication efforts for the embedded microchannels-3D manifold coolers (or EMMCs). The microfabrication process is introduced and explained step-by-step, followed by two major fabrication challenges. In Section 2.1, we describe the configuration of the EMMC design with geometric dimensions. In Section 2.2, four major steps of the microfabrication process are explained. In Section 2.3 and 2.4, two major fabrication challenges are discussed: double-sided anisotropic Si etching process and Au-Si eutectic bonding followed by Au-Au thermocompression bonding.

### **2.1 Design of Embedded Microchannels-3D Manifold Cooler**

The EMMC consists of two parts: a cold-plate (CP) and a fluid manifold substrate. Anisotropically etched microchannels are defined on one side of the CP, and a serpentine Au/Ti heater is deposited on the other side of the CP. Likewise, inlet openings, inlet plenums, and inlet/outlet conduits are anisotropically etched into the manifold substrate from both sides.

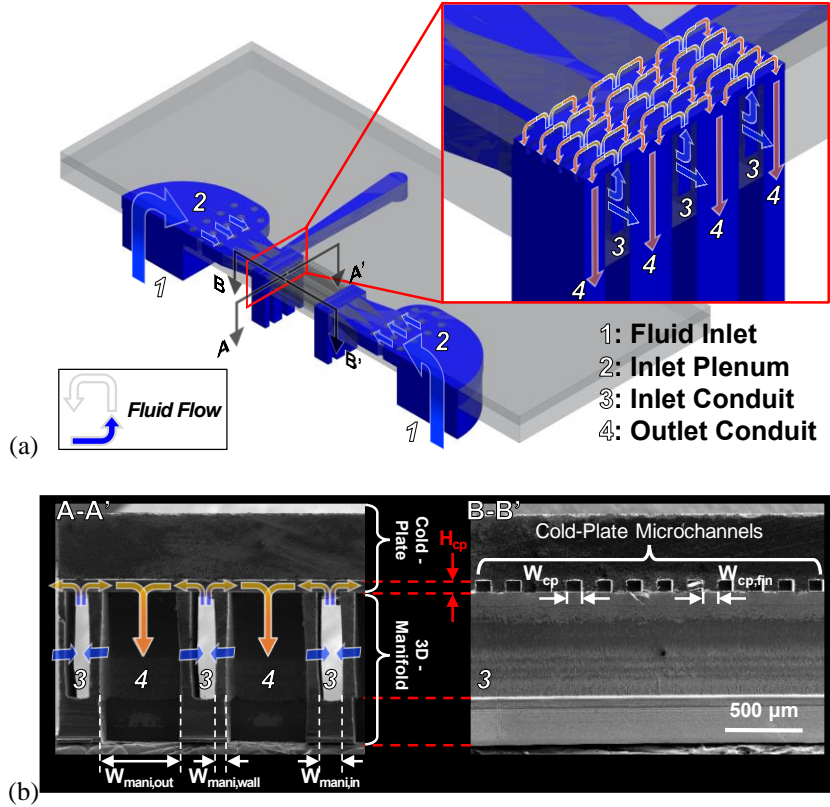


**Figure 2. 1** Conceptual design of an Embedded Microchannel-3D Manifold (EMMC), (a) representation of the fluid flow pattern inside the EMMC, (b) a SEM image of cross-sectional view of the actual EMMC device

Figure 2.1a describes the working principle of the EMMC. The fluid is supplied through the fluid inlet openings (1) from the backside of the manifold substrate and it is uniformly distributed within the inlet plenums (2). The distributed fluid passes the gradual contraction region (between 2 and 3) and keeps flowing through the inlet conduits (3) until it reaches to the intersections between the manifold inlet conduits and the CP microchannels (between 3 and 4). At the intersection, the fluid is diverged and the partial fluid moves toward the CP microchannels' heated section by making a 90° turn. The diverged fluid proceeds along the CP microchannels and heat is transferred from the CP microchannels' surface to the fluid until it exits through the adjacent manifold outlet conduits (4) by making another 90° turn. The non-diverged fluid at the intersection keeps flowing along the manifold inlet conduits until it reaches to the next intersection and the same flow pattern as described earlier is repeated. Figure 2.1b is SEM images of a fabricated test sample that show the placement of CP microchannel, manifold inlet/outlet conduits and depicts how the 90°-turns are made inside of the device with 3-D arrows.

Important geometric parameters are introduced in Figure 2.2. The key dimensions to describe the geometry of a Ti/Au serpentine heater (20 and 500 nm of thickness, respectively), CP microchannels, and microstructures in the manifold, are listed in Table 2.1.

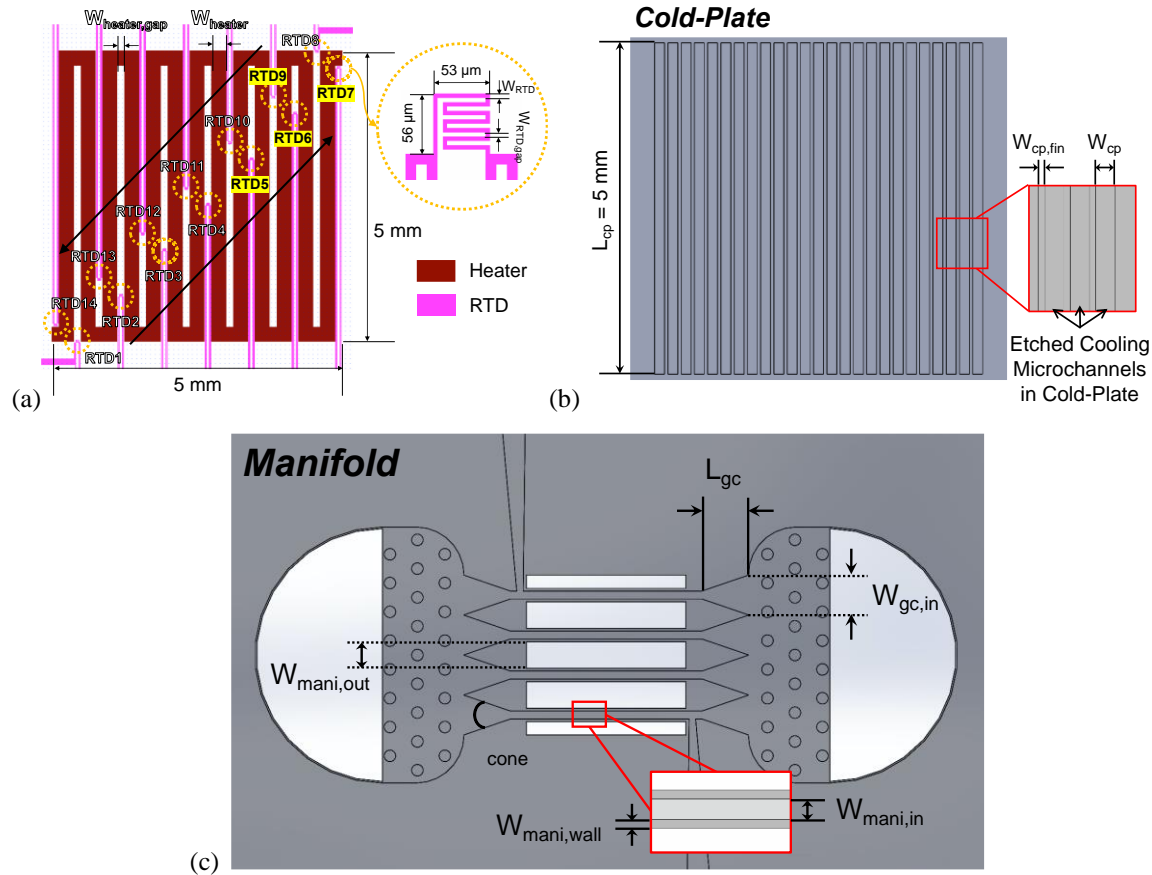


**Figure 2. 2** Geometric parameters of microfeatures, (a) Ti/Au serpentine heater with RTDs are placed on a  $5 \times 5 \text{ mm}^2$  center area of the cold plate. RTDs are diagonally placed in between the heater lines and only RTD5, 6, 7, and 9 (highlighted) were used for actual temperature measurement. Measured temperature coefficient of resistance (TCR) of RTDs was  $3.1 - 3.3 \times 10^{-3} \text{ }^\circ\text{C}^{-1}$  and the thicknesses of the heater and the RTD are 500 nm, and 50 – 55 nm, respectively. A closed-loop flow system is used for RTD calibration by varying the temperature of the liquid and recording corresponding electrical resistance for individual RTDs (b) & (c) Design of various anisotropically etched structures in (b) the cold plate and (c) the manifold, see Table 5.1 for geometry details. A set of pin fin arrays at the entrance and exit plenums are utilized to create uniform flow distribution.

**Table 2. 1** Dimensions of structures in the cold-plate and the manifold

Substrates	Structures	Symbols	Dimensions
Cold Plate	Microchannels	$H_{cp}$	75 $\mu\text{m}$
		$W_{cp}$	150 $\mu\text{m}$
		$W_{cp,fin}$	50 $\mu\text{m}$
	Serpentine heater	$W_{heater}$	250 $\mu\text{m}$
		$W_{heater,gap}$	125 $\mu\text{m}$
	RTD	$W_{RTD}$	4 $\mu\text{m}$
$W_{RTD,gap}$		4 $\mu\text{m}$	
Manifold	Inlet micro-conduits	$H_{mani,in}$	700 $\mu\text{m}$
		$W_{mani,in}$	150 $\mu\text{m}$
		$W_{mani,wall}$	81 $\mu\text{m}$
	Exit micro-conduits	$H_{mani,out}$	1000 $\mu\text{m}$
		$W_{mani,out}$	520 $\mu\text{m}$
	Inlet Plenums	$R_{mani,plen}$	4 mm
		$L_{gc}$	1.45 mm
		$\theta_{cone}$	37.70°
	Fluid Inlet Supply	$R_{inlet}$	3.25 mm

Uniform heat fluxes were applied at the top surface of the cold-plate by means of electrical Joule-heating in a serpentine Ti/Au heater covering a 5 x 5 mm<sup>2</sup> active region of the cold plate. The top surface temperature is monitored by i) several RTDs placed in between the serpentine heater lines, ii) an Infra-red camera, and iii) the serpentine heater itself as another RTD. The RTDs are located diagonally to provide a clear picture of the heating and flow patterns, depicted in Figure 2.2a. The RTDs were calibrated individually before every measurement, the temperature coefficient of resistant (TCR) of the RTDs ranged from 0.0031 to 0.0033 /°C and the change of TCR was maintained within 0.7% after each experiment. We could only utilize 5 out of a total 14 RTDs (RTD5, 6, 7, and 9: highlighted in Figure 2.2a) due to microfabrication defects. The RTD located at the center of the chip was not functional, as a result the heater maximum temperature,  $T_{heater,max}$  is calculated by taking the average temperature of the RTDs 5, 6, 7, and 9, in combination with the scaling factor calculated from the CFD modeling, the process is detailed in Appendix A.4. The associated uncertainty with this procedure is quantified in Appendix B.1 and is estimated to be 1.4 – 3.1 %.

## 2.2 Description of microfabrication process

Two silicon substrates were prepared for the cold plate and manifold layers. Using standard microfabrication techniques, alignment marks were defined and isotropically etched on front and backside of both substrates (Figure 2.3, Step 1).

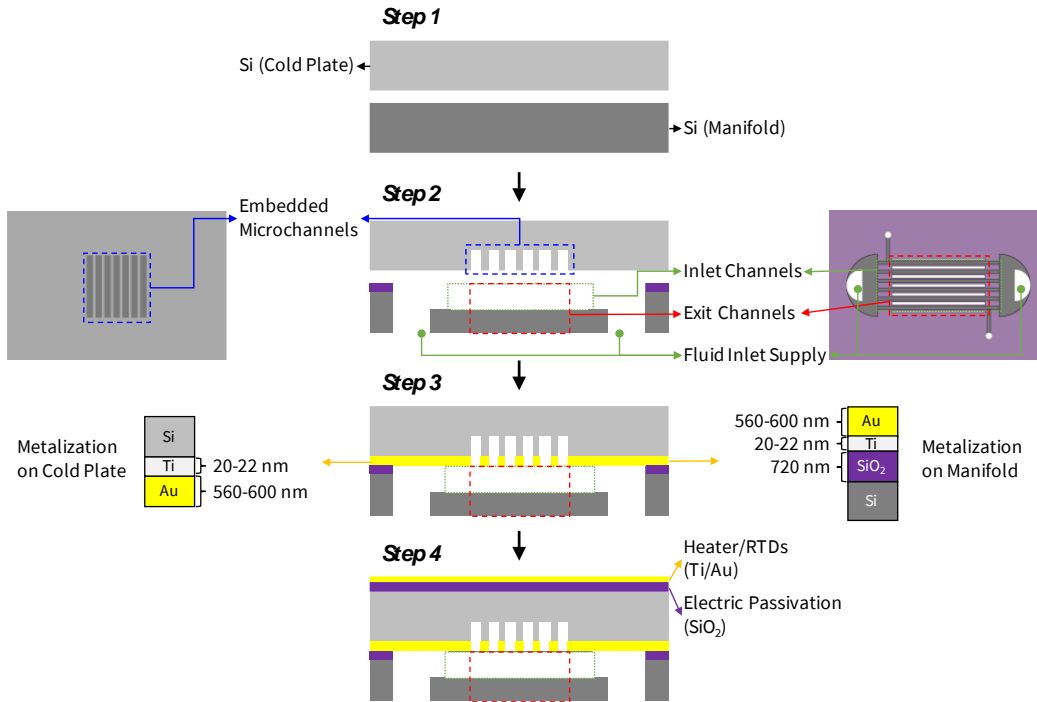


**Figure 2. 3** Overall microfabrication process of the embedded microchannel-3D manifold cooler. *Step 1:* double-polished Si substrates with thickness of 500  $\mu\text{m}$ , and 1000  $\mu\text{m}$  were prepared for the cold plate and the 3D manifold structures, respectively. *Step 2:* Microchannels and other microscale features were anisotropically etched in the cold plate and the 3D manifold substrates. Double-sided anisotropic Si etch technique was used to define the microstructures with different etch depth in the 3D manifold. *Step 3:* Au-Si eutectic bond layers were deposited on the cold plate and the 3D manifold substrates. Ti/Au layer thickness on each substrate is denoted in Figure 2. As the Ti layer on the cold plate functioned as a native oxide getter, Au-Si eutectic reaction was activated from the cold plate surface. 720 nm of SiO<sub>2</sub> layer on the manifold substrate insulated Si from the Au layer and it helps to induce better Au-Si eutectic reaction [68]. *Step 4:* A serpentine heater and RTDs were deposited on top of Si<sub>x</sub>N<sub>y</sub>/SiO<sub>2</sub> electric passivation layer. Since Ti reacts with SiO<sub>2</sub> at high temperatures, it is recommended to deposit a thin Si<sub>x</sub>N<sub>y</sub> layer between Ti and SiO<sub>2</sub> layers to prevent further reaction

In the cold plate, microchannels for convective cooling were anisotropically etched from the backside. In the manifold, there were two anisotropic etch processes to define

the microstructures. The 3D manifold fluid inlet and exit micro-conduits, inlet plenums, pressure taps and flow distributors were etched from the front side. After then, thin Al layer was sputtered to protect the etched features from the front side and holes for fluid inlet supply, and exit micro-conduits were etched from the backside until they were etched through (Figure 2.3, Step 2).

After all of the microstructures in each substrate were defined, the manifold substrate was cleaned in Al etchant to remove residual Al on the surface and it went through organic cleaning in a Piranha bath. Since there had been no metal on the cold plate substrate, the cold plate substrate was cleaned in a Piranha bath only. Ti/Au eutectic bond layers were deposited on bond interfaces, bottom surface of the cold plate and top surface of the manifold, by a metal evaporation process. Another organic clean process was conducted after the metal evaporation process, and both substrates were aligned with the predefined bonding alignment marks from Step 1. Au-Si eutectic bond was formed while high process temperature, 410 – 420 °C, and high compressive pressure, > 425 kPa, conditions were applied to the bond interfaces (Figure 3, Step 3). Lastly, 1 μm thick PECVD SiO<sub>2</sub> and Ti/Au (20/500 nm) layers were deposited on the top surface of the bonded substrate to define an electrical insulation layer, and a metal serpentine heater and RTDs, respectively.

### **2.3 Fabrication achievement 1: Double-sided anisotropic Si etching process**

One of the major challenge in the microfabrication process comes from the inherent design configuration of the manifold substrate: inlet and outlet conduits with two different channel heights, 700 μm, and 1000 μm. In addition, the inlet and outlet manifold conduits are placed side-by-side in a same Si substrate.

Figure 2.4 describes the overall double-sided etch process and the resulting images during the process.

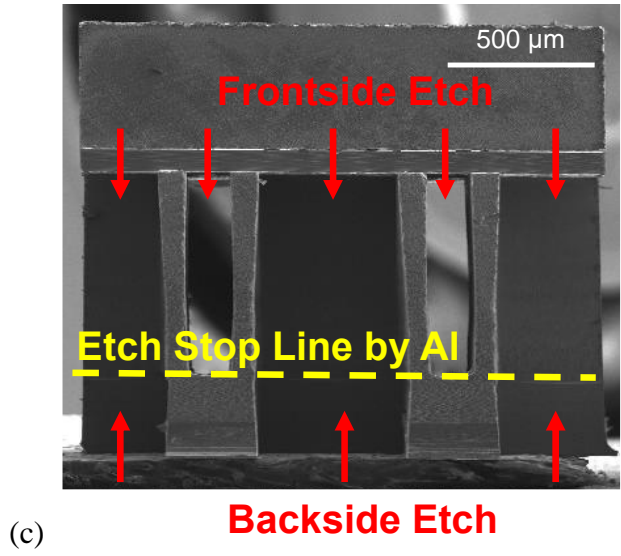
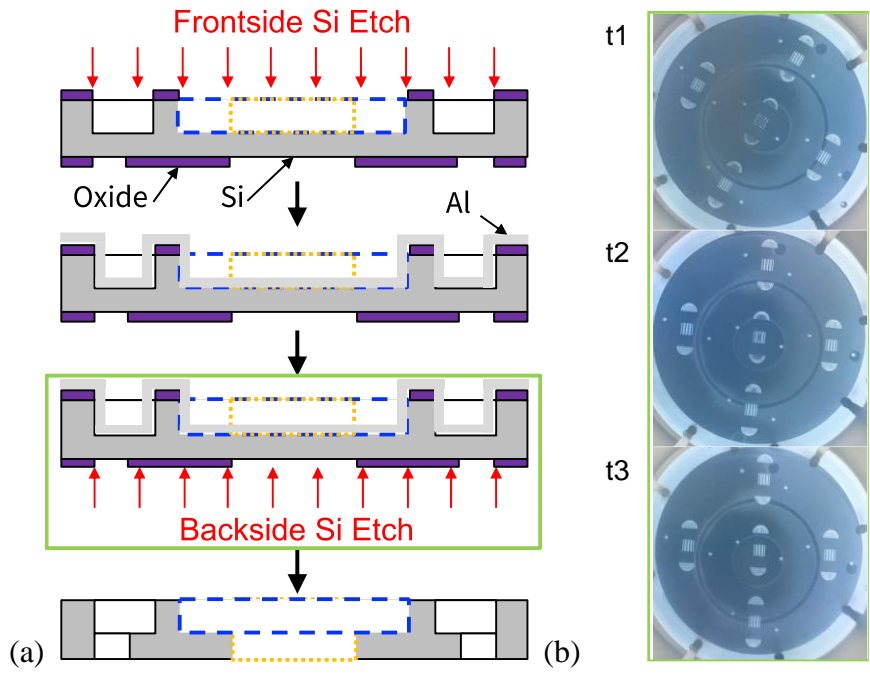


**Figure 2. 4** (a) The overall double-sided anisotropic Si etching process to fabricate manifold structures, masking-frontside etch-masking-backside etch steps are depicted, (b) timelapse images captured during the backside Si etch, (c) a finished microchannels-3D manifold sample in SEM, yellow etch stop line consists of 200-300 nm Al sputtered after the frontside etch.

First the Si substrate is coated with 2 μm thick thermally grown SiO<sub>2</sub> in a furnace by wet oxidation at 1100 °C for 8.5 hrs. Additional 1 μm thick PECVD SiO<sub>2</sub> is deposited right after the thermal oxidation process. After all, the thickness of the oxide layer is 3 μm

to be used for long-term anisotropic Si etch process. A typical anisotropic Si etch rate in a dry etcher, STS reactive ion etcher, is 3 – 4  $\mu\text{m}/\text{min}$  with the Si-to-SiO<sub>2</sub> etch selectivity of 150 – 200. Another 4  $\mu\text{m}$ -thick photoresist layer is deposited on top of the SiO<sub>2</sub> layer and define a device area by the first lithography process. The same process is conducted for both top and bottom surface of the substrate.

Next step is open the defined device areas on top and bottom surface of the substrate in an oxide etcher, PlasmaTherm Oxide etcher. This tool is an inductively coupled plasma etch system configured for dielectric etching. The mixture of CHF<sub>3</sub>, O<sub>2</sub> gases are used to etch the oxide layer until it opens up the bottom Si substrate.

After the oxide etch process, the photoresist masking layer is not removed but used again for following deep Si etching process because the target etch depth of the anisotropic Si etch is up to 700  $\mu\text{m}$ . With the Si-to-photoresist etch selectivity of 100, the required photoresist thickness is 1 – 2.5  $\mu\text{m}$ .

The first anisotropic Si etching process is conducted on the top surface of the substrate. The typical Bosch process is used to pattern inlet plenum, inlet and outlet conduits on the top surface. In Figure 2.4c, the red arrows indicate the etched regions into the top surface, which are the inlet and outlet conduits of the manifold. The repeated etch-passivation steps are conducted for 4 – 5 hrs to etch 700  $\mu\text{m}$  deep micro-conduits in the substrate.

After the first anisotropic Si etching process, an Al metal layer is sputtered on the top surface. Since the inlet conduits are connected to the inlet plenums of the manifold, the sidewall of the inlet conduits can be vulnerable if the Si etch gas, SF<sub>6</sub>, is introduced through the inlet plenum during the backside Si etching process. Therefore, the etched features into the top surface are coated with metallic etch stop layer, Al.

After the metallic etch stop layer is deposited on the top surface, the substrate is flipped upside down, and the second anisotropic Si etching process is conducted. The target etch depth is remaining 300  $\mu\text{m}$ , and the bottom surface is continuously monitored through the viewing window of the Si etcher. In Figure 2.4b, the brighter grey color in the patterns represents the Al, and the darker grey color in the patterns represents the remaining Si. As the anisotropic Si etching process continues, the darker grey regions

reduce but the brighter grey regions are widened in the etched patterns ( $t1 \rightarrow t3$ ). The moment when the etched patterns are full of brighter grey color is the end of the backside Si etching process. After the double-sided anisotropic etching is finished, the remaining mask layers, Al, and SiO<sub>2</sub>, are removed from the substrate by aluminum etchant and buffered HF solution in a wet bench, respectively.

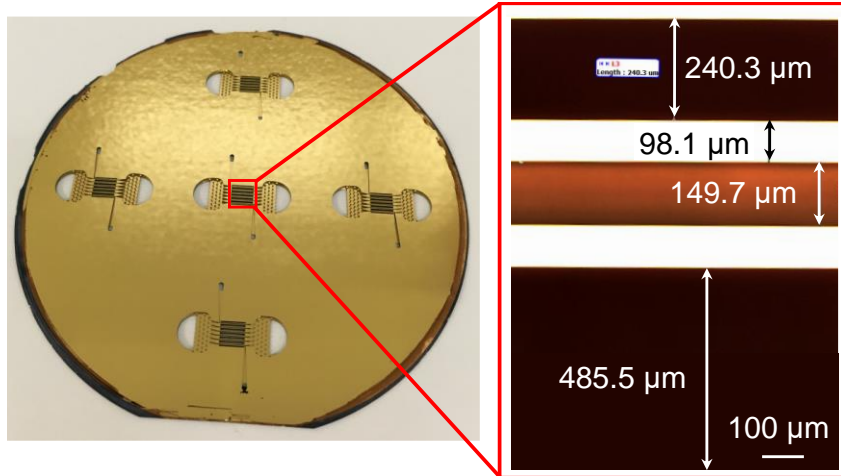


**Figure 2. 5** One of the finished manifold substrates, the dimensions of inlet and outlet conduit are checked under microscope and the measured dimensions are almost identical to the target values, see Table 2.1.

In Figure 2.5, we have confirmed that the dimensions of the manifold inlet and outlet conduits are close to the target values of the original design thanks to the double-sided anisotropic Si etching process.

### 2.3 Fabrication achievement 2: Au-Si eutectic bonding

The second major challenge in the microfabrication process is to create a strong bonding interface between two Si substrates. The bonding interface has to be strong enough not to be broken under pressurized environments. There are many different bonding types shown in Figure 2.6:

Factor	Criteria	Anodic	Glass-frit	Direct	Eutectic
Bond Force	< 10 kN	Green	Green	Green	Green
Bond Temp.	Large Temp. Range	Red	Red	Green	Green
Alignment Capability	< 2 $\mu\text{m}$	Red	Red	Green	Green
Hermetic Seals	Should be hermetic	Green	Green	Green	Green
Heterogeneous Integration	Should be possible	Red	Green	Red	Green
Roughness Requirement	> 10 nm	Green	Green	Red	Green
<b>Potential Issues</b>		Not CMOS/FEOL compatible	Dirty process, large bond line width, high temp.	Requires clean particle-free surfaces	Potential oxidation of metal layers

**Figure 2. 6** Head-to-head comparison of different bonding strategies (green: good, red: bad) [67]

According to the head-to-head comparison table [67], the eutectic bonding is the most promising bonding method for the EMMC. The EMMC should go through some harsh conditions: i) temperature variation across the cold-plate substrate is more than 120 °C, ii) internal pressure change can be up to 100 kPa, iii) low-surface tension fluids flow through the microchannels. In order to satisfy all of these conditions, the eutectic bonding is the best option among others.

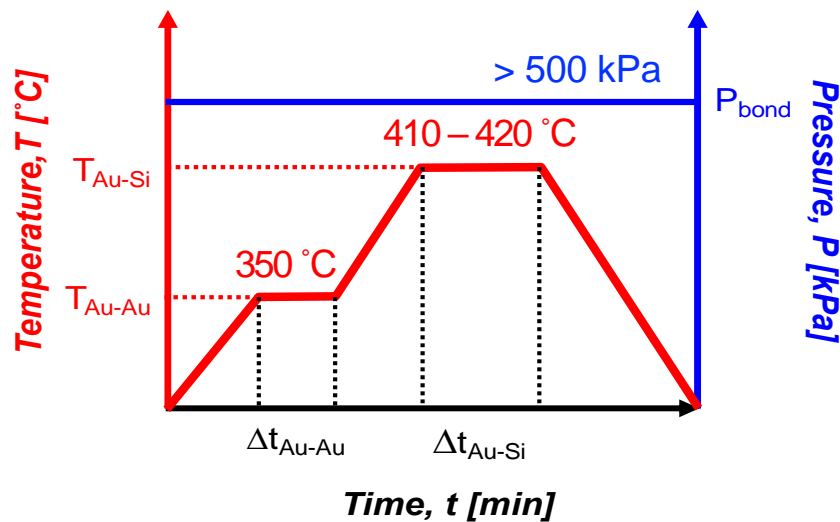
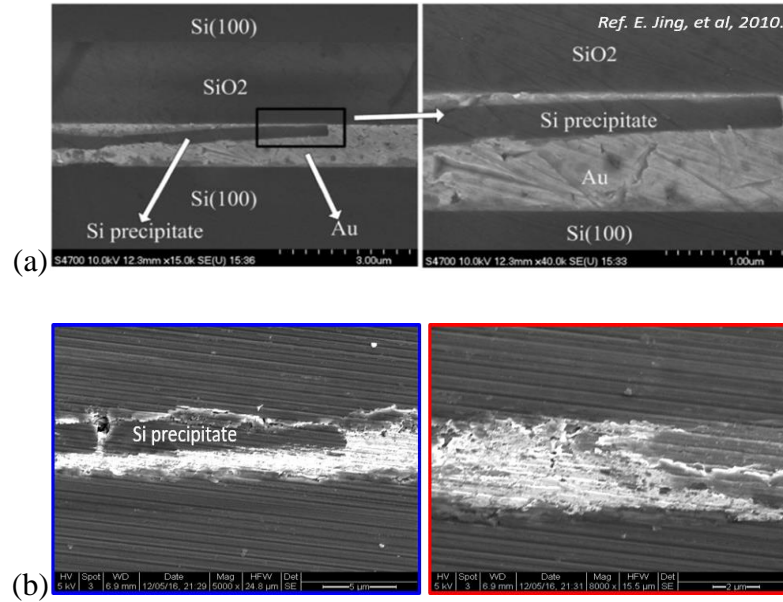


**Figure 2. 7** The characterized Au-Si eutectic bonding recipe.

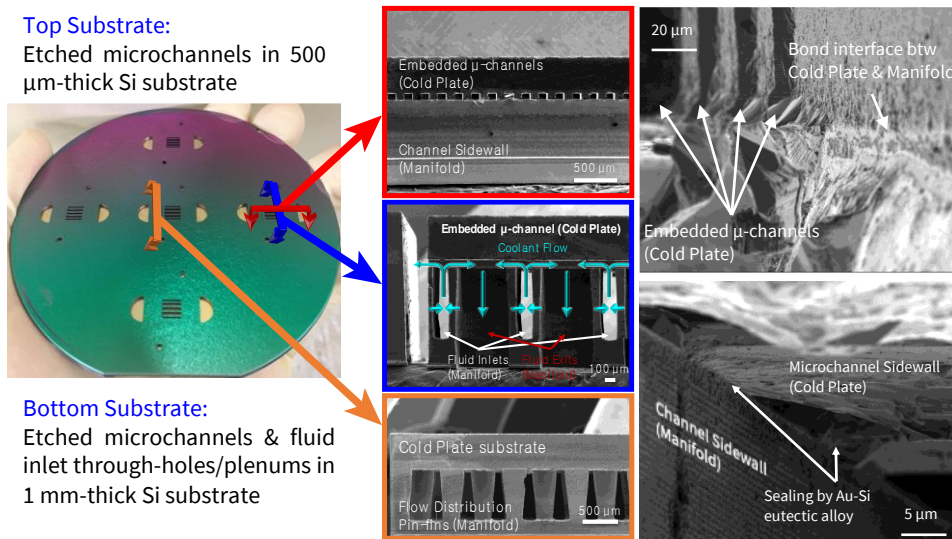
The Au-Si eutectic bonding is chosen for many reasons: i) one of the source material, Si, is coming from one of the Si substrates, no additional metal or dielectric material deposition process is required, ii) the migration of Si atoms from the substrate to the Au layer can create strong bond interface if the bonding is made, iii) the Au-Si eutectic reaction can be self-regulated due to abundant Si material in the Si substrate, iv) the finished bonding is irreversible.

Figure 2.7 shows the characterized Au-Si eutectic bonding recipe with three parameters, temperature, pressure and time. First, two substrates, a cold-plate and a manifold substrate, are joined and placed in a vacuum chamber of the bonding tool, EVbond. Once the chamber is vacuumed, a uniform compressive force up to 3340 N, corresponding compressive pressure of 450 – 500 kPa, is applied to the top and bottom surface of the joined substrates. After then, the bottom chuck of the chamber is heated up to 350 °C for the Au-Au thermocompression bonding. The bonding temperature at this step is maintained for 5 minutes to make a good contact between two separate Au layers. After the Au-Au thermocompression bonding, the bonding temperature is ramping up to 410 – 420 °C to induce Au-Si eutectic reaction. We allow the Au-Si eutectic reaction for 15 – 20 minutes and ramp down the chuck temperature for a couple of hours.

In Figure 2.3, the metal layer configuration for Au-Si eutectic reaction is given: 20 nm of Ti and 500 nm of Au. The layer thickness is determined based on many bonding trials and errors. After all those trials, we found that 20nm of Ti layer works as a native oxide getter rather than a Si diffusion barrier. Jing, et al [68] insisted that thin Ti layer worked as a native oxide getter and the bonding interface became thicker than the original Au layer thickness[68]. Also, they argued that diffused Si precipitates in the bonding interface are proofs of successful Au-Si eutectic bonding [68]. In Figure 2.8a, two SEM images are given from Ref. [68] and they show the Si precipitate in the Au layer. We have also noticed similar structure from one of the Au-Si eutectic trials, which is given in Figure 2.8b. The blue boxed SEM image shows a clear Si precipitate in the Au layer similar to the Si precipitate in Figure 2.8a. The used Ti layer thickness was 20 nm and we could conclude the optimal thickness of Ti for a good quality Au-Si bonding is 20 nm.



**Figure 2. 8** (a) SEM images from Ref. [68], and (b) from earlier Au-Si eutectic bonding trials. Si precipitates are recognized in the Au layer in both cases.



**Figure 2. 9** (Left) A bonded wafer pair after Au-Si eutectic bonding, (middle) aligned microstructures in the cold-plate and the manifold, (right) sealed interfaces by Au-Si eutectic alloy

Figure 2.9 shows the bonded wafer pair after the Au-Si eutectic bonding. The bonded wafer is diced in a wafer-saw system into multiple pieces to check the bonded interfaces at multiple regions. The SEM images in the middle column are representative images showing the fabricated micro-structures: etched microchannels in the cold-plate, inlet and outlet conduits of the manifold, inlet plenum. We could confirm that the microchannels in the cold-plate and the inlet/outlet conduits of the manifold are precisely aligned after the Au-Si bonding. In addition, multiple bonding interfaces between two substrates are viewed by high magnification SEM. The exemplary images are given in Figure 2.9 (right), and the gap between two substrates is perfectly sealed by Au-Si eutectic alloy

# Chapter 3

## Experimental methodology

This chapter describes the overall configuration of the experimental system. A closed-loop flow system is the heart of the convective heat transfer experiments and there are several functional requirements for this study.

i) Various types of coolants can be used in the system. DI water, and low-surface tension dielectric coolants (i.e. R-245fa, HFE-7100, etc) are the candidates for the study.

ii) Thermofluidic properties of the test system should be monitored in real-time with a good accuracy. The detailed uncertainty study is discussed in Appendix B.1.

iii) The experimental setup should be robust for the repeated operations.

In Section 3.1, the closed-loop flow system is described in three aspects: hardware, software, and test section. The components consisting of the flow loop are analyzed by their functionality. In Section 3.2, we discuss the surface temperature measurement procedure by an Infra-red (IR) camera. The calibration process of the IR system is discussed and an exemplary measurement result is following.

### 3.1 Description of a closed-loop flow system

#### 3.1.1 Hardware configuration

A fluid flow loop, depicted in Figure 3.1, is used to achieve the desired test conditions at the inlet of the test module. Water and R-245fa are used as the working fluid for the experiments.

A magnetically coupled gear pump is used to pump the fluid in the loop, which passes through a Coriolis flow meter, and a filter before entering the test module. Upon exiting

the test module, the heated fluid is passed through another filter and a water-cooled heat exchanger, and eventually returns to the geared pump to complete the cycle. The reservoir can be attached by adjusting inlet, drain, and fill valves when the flow loop needs to be refilled with fresh coolant. In order to remove non-condensable gases from DI water in the reservoir, the reservoir is detached from the loop, the DI water inside the reservoir is boiled up by the attached immersion heater, and the captured non-condensable gases above the water are released through a release valve on the reservoir wall.

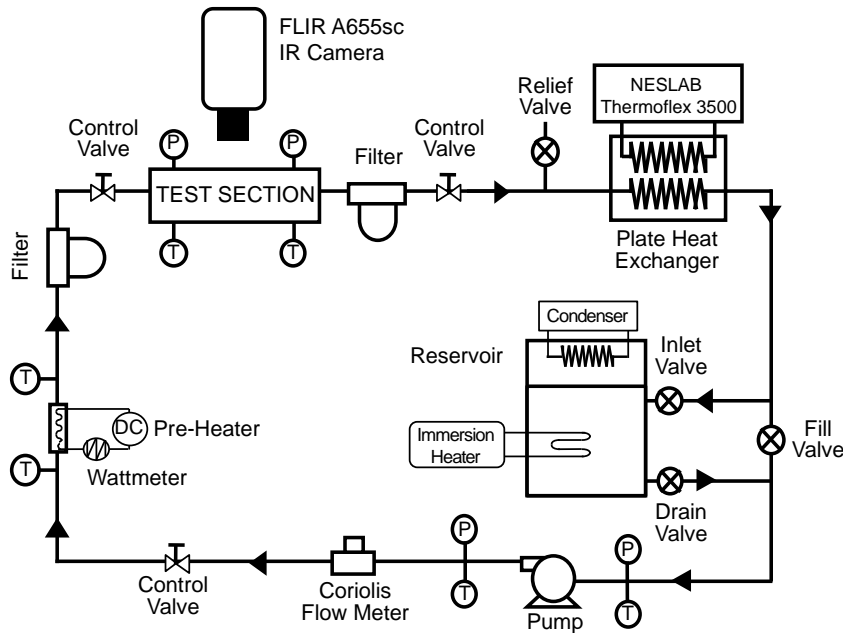


**Figure 3. 1** A depiction of the closed-loop flow system that uses single-phase DI water as the working fluid for the current experiments

Three main functionalities are highlighted. (1) Fluid flow control: a fluidic pump (MICROPUMP GJ-N23) coupled with a Coriolis flow meter (Micro Motion CMFS010) are controlled by a PI feedback control system written in LabVIEW 2016. (2) Temperature/Pressure measurement: multiple K-type thermocouples are placed along the fluid flow path to track down the fluid temperatures at each measurement point. An IR camera (FLIR A655sc) mounted above the test section records the temperature of the exposed surface during the experiments. The heater resistance has been recorded for Electric Resistance Thermometry (or ERT) purpose. Two absolute pressure transducers (OMEGA PX419-500A10V) at the inlet/outlet of the test section, and one additional

differential pressure transducer (OMEGA PX2300-5DI) between the inlet and outlet of the test section, are used to measure pressure change in the test section. (3) Fluid temperature control: the heated fluid after the test section is cooled down at the plate heat exchanger coupled with the recirculation bath (NESLAB Thermoflex 3500). A DC-powered immersion heater is used for fine tuning of the inlet temperature of the fluid before the test section.

The basic operating conditions are listed in Appendix A.1. The inlet pressure is above atmospheric pressure for two reasons: i) supplying coolants from pressurized containers to the flow loop adds extra pressure to the loop, and ii) more pressure head is produced by the pump to circulate the fluid. We intend to increase the loop pressure with the increased heat fluxes and flow rates to keep the boiling condition to subcooled boiling. The subcooled boiling delays the onset-of-nucleate boiling on superheated channel walls and it can remove much higher heat fluxes than saturated boiling scheme. The details will be discussed in Section 5.2.3. The instrument accuracy information of each component is listed in Table 3.1.

**Table 3. 1** Sources of measurement uncertainties for data analysis

<b>Components</b>	<b>Affected Parameters</b>	<b>Accuracy</b>
Thermocouple (K-type)	$T_0, T_{f,in}, T_{f,out}$	$\pm 0.1 \text{ }^\circ\text{C}$
HP34401A Multimeter	$\Delta V_{\text{heater}}, I_{\text{heater}}$	$\pm 0.1 \%$
Temperature Coefficient of Resistance, Au <sup>†</sup>	$\alpha$	$\pm 0.1 \%$
Micro Motion CMFS010 Coriolis mass flow meter	$Q_{\text{total}}$	$\pm 0.10\%$ of rate (Liquid)
Omega PX2300-5DI	$\Delta P_{\text{total}}$	$\pm 0.25\%$ RSS FS (FS: 0 – 5 psi)

<sup>†</sup> Temperature Coefficient of Resistance, or TCR, of Au is the material's property, but it can be differed by deposition conditions. The measured TCR of Au heater is 0.0033 /<sup>o</sup>C which is close to the reported TCR of Au bulk [78].

### 3.1.2 Software configuration

Once the test section was integrated to the closed-loop flow system, LabVIEW code was utilized to control the micro-pump and to record temperature and pressure information related to both the fluid and the test sample. All measurements were taken once the system reached steady-state in the experiments.

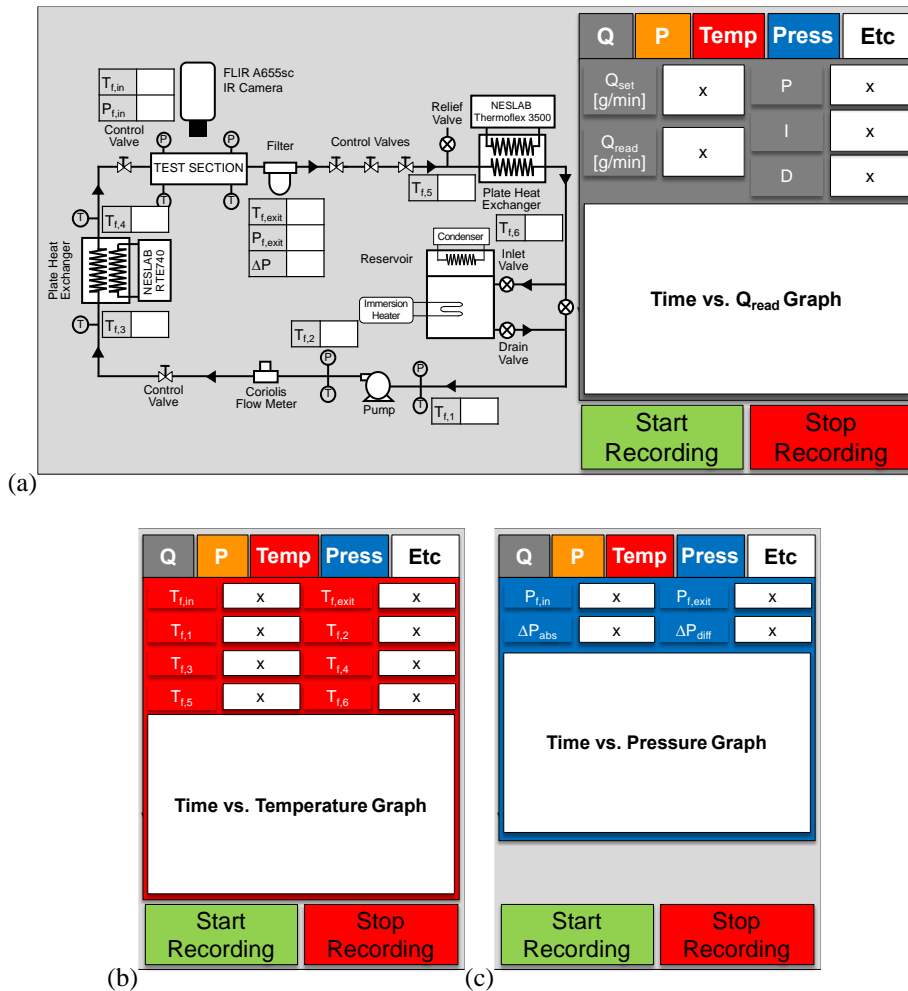


**Figure 3. 2** The user interface for the flow loop operation programmed by the Labview, (a) the flow loop schematic with a separate panel to control the flow rate, (b) & (c) another options to monitor temperature and pressure at various locations in the loop.

The basic user interface design is given in Figure 3.2. The images are simplified drawing from the original user interface programmed by the Labview. The user interface for the flow loop consists of the flow loop schematic and a separate panel. The panel has

five selectable tabs to control or monitor flow rate, pressure, temperature, and electric power supplied to the test sample. For now, the electric power is manually controlled, not by the program, but this functionality will be added in near future.

The first tab in Figure 3.2a shows target and measured flow rates at the same time. The actual flow rate is measured by the Coriolis flow meter and it transmits the electric signal to the system's DAQ and the software converts the raw electric signal to the flow rate. By taking difference between these two values, a PI feedback control adjusts the pump input signal, electric current, to match the actual flow rate to the target value (see Figure 3.3). The actual flow rate is updated and plotted in the subwindow of the panel in real-time. The pressure and temperature measurement tabs (Figure 3.2b and 3.2c) show the measured pressure and temperature values at the various locations along the flow loop and the measurement results are updated in real-time.

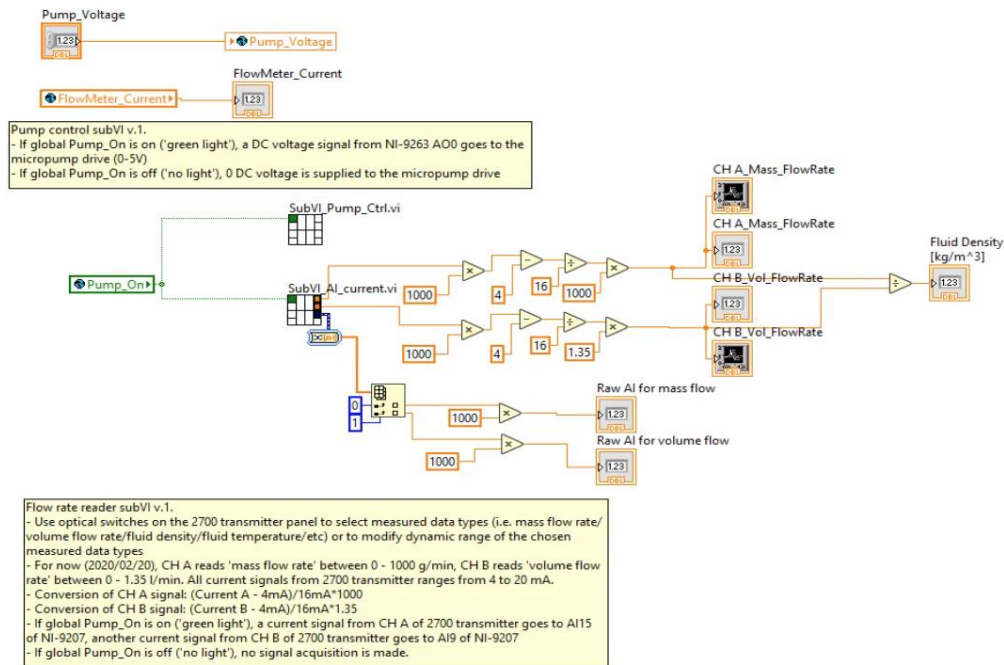


**Figure 3. 3** A captured PI feedback control subfunction programmed by the Labview.

### 3.1.3 Test section configuration

A polycarbonate plastic (Lexan) and PEEK test module is manufactured, see Figure 3.4. The test module contains two inlet ports on the side walls and one outlet port on the

bottom wall. The microfabricated sample is placed on the top side of the test module where the inlet and outlet openings on the sample and the module mate with each other. Fluid pressure is measured at the inlet and outlet of the test module with ports milled into the test module. Fluid temperature measurements are made with type-K thermocouples, having  $\pm 1^\circ\text{C}$  error, inserted into the flow in separate inlet and outlet ports. In the later experiments, the type K thermocouples are calibrated by a reference temperature probe, Fluke 5615-6, which has accuracy of less than  $0.035^\circ\text{C}$  in the normal operation range ( $-20$  to  $420^\circ\text{C}$ ). The adjusted uncertainty of the K-type thermocouple is now reduced to  $\pm 0.1^\circ\text{C}$ .

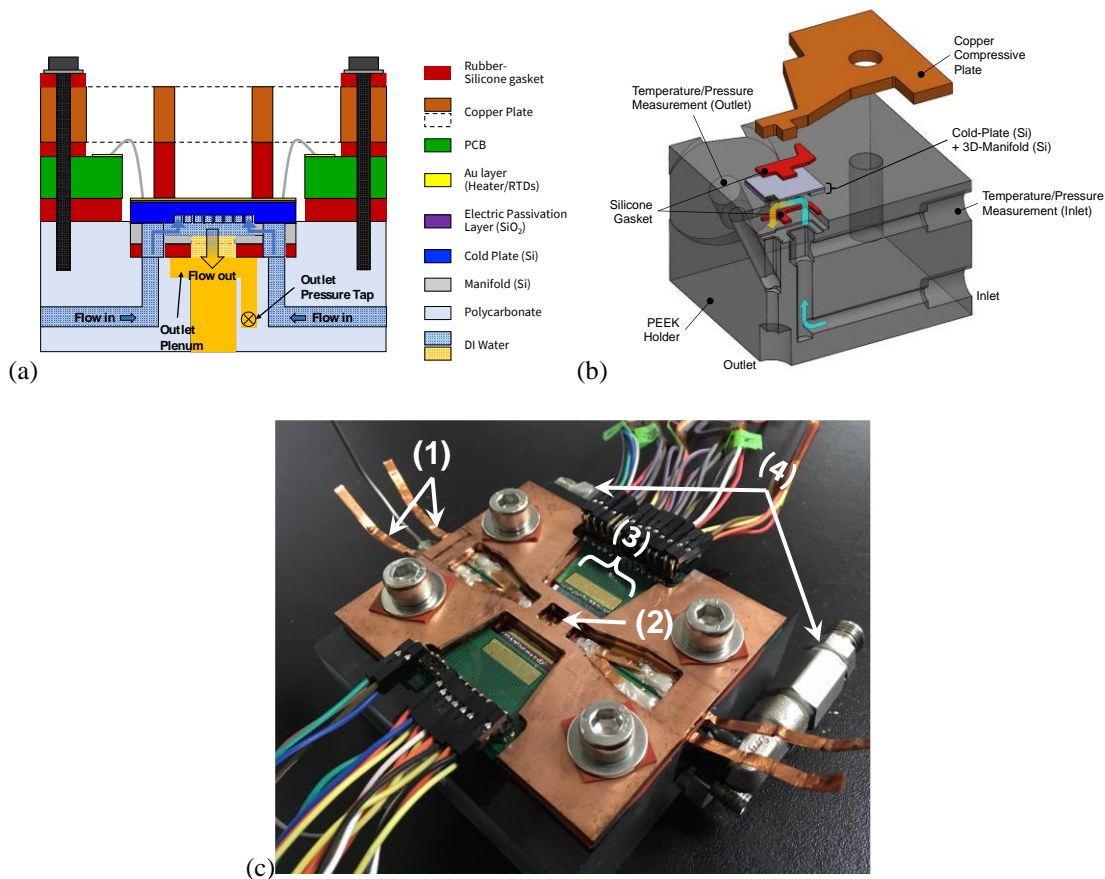


**Figure 3. 4** (a) & (b) A cross-sectional view of an assembled test, and (c) an image of the assembled test section. (1) Power supply lines, (2) 5 mm-by-5 mm heated region in the sample, (3) Au electrode pads that are connected to RTDs, (4) Swagelok fittings for inlet and exit pressure read-outs.

In the early stage of the heat transfer experiments, RTDs were used to measure the surface temperature of the sample. However, this approach only captures partial

temperature information of the heated surface and we have to heavily rely on conjugate CFD simulation modeling to predict temperature gradient across the heated surface. It may be okay for the single-phase heat transfer cases, but there is no accurate simulation modeling for two-phase heat transfer cases. Therefore, we installed another temperature measurement system, an Infra-red (IR) camera, over the test section (Figure 3.5a). The details about the temperature measurement by the IR system will be discussed in Section 3.2.

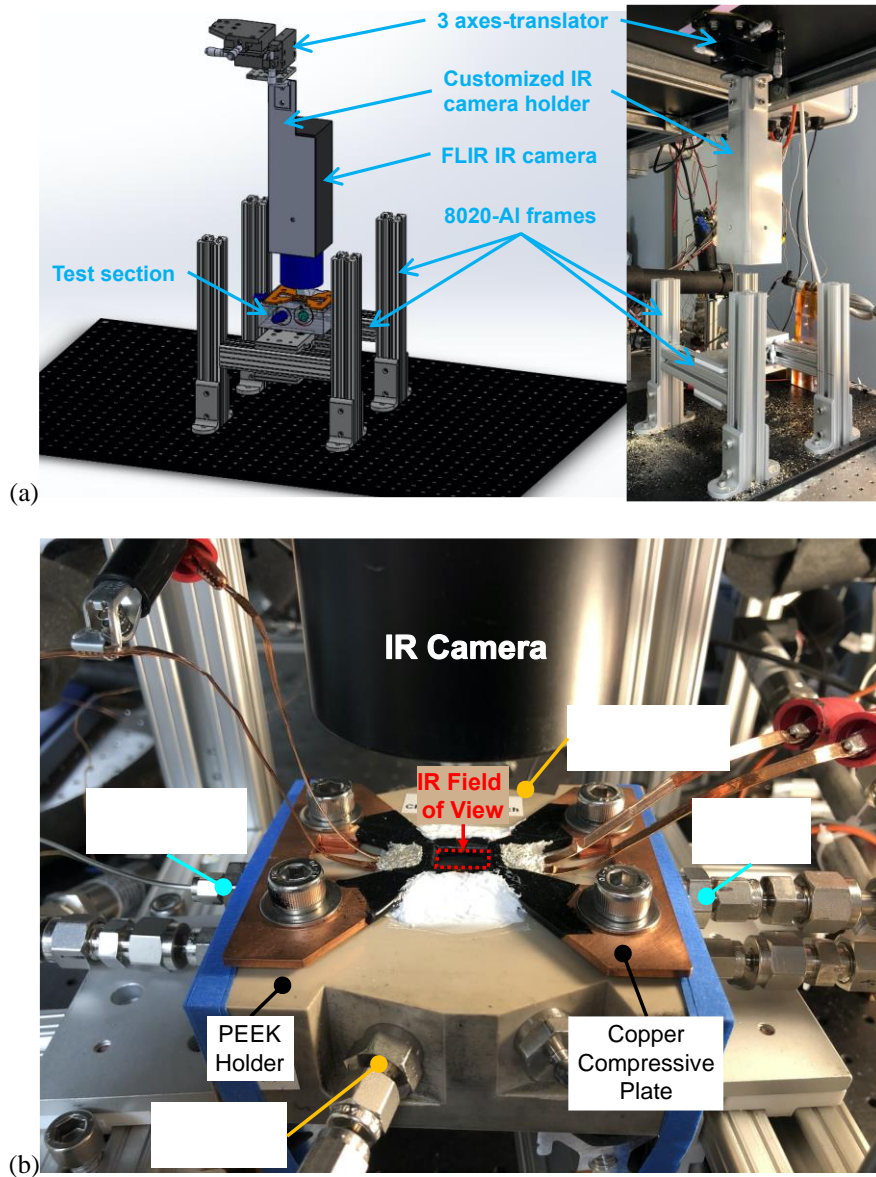


**Figure 3. 5** (a) A new sample holder schematic drawn by Solidworks2018, and the actual holder setup in comparison, (b) the actual test section with other experimental components.

A new sample holder system consists of 8020-Aluminum frames. The holder is placed on top of the air table and the test section is placed in the middle for the measurement. A FLIR IR camera (A-655sc) is placed over the test section held by a customized IR camera holder. A 3 axes-translator is joined to the IR camera holder to change the position of the IR camera during the experiments. Figure 3.5b shows the test section, an IR camera, and other experimental components ready for the heat transfer tests. Again, the fluid is intraduced through two inlet ports placed at the left and right side of the test section, and it exits through the outlet port plated at the bottom side of the test section. The entire test section is compressed by a copper compressive plate for the complete sealing, and electric power is delivered through the copper wires attached to the EMMC sample. The heater area is covered with black spray paint for the IR measurement.

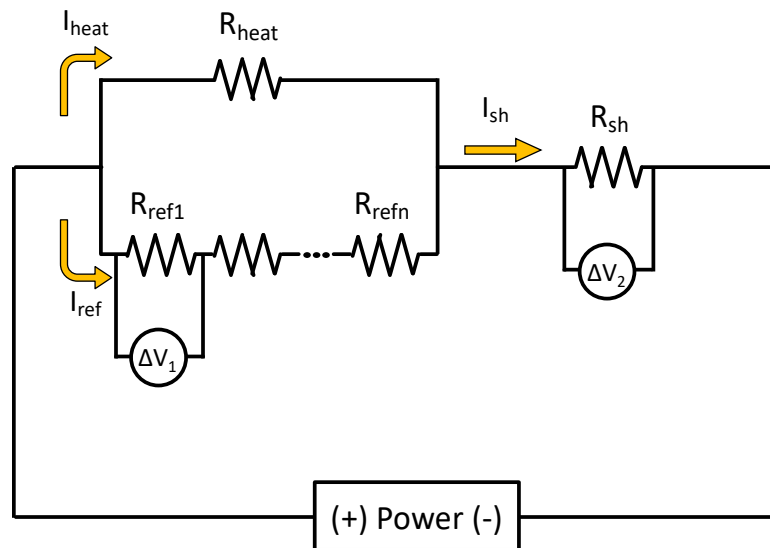


**Figure 3. 6** A schematic of electric circuitry to measure electric power dissipated by the heater.

Lastly, additional electric circuitry is installed next to the test section. Since the readouts of the power supply cannot be recorded through DAQ, the extra circuitry is designed for accurate measurement of the voltage drop,  $\Delta V_{\text{heat}}$ , and the electric current,  $I_{\text{heat}}$ , across or through the heater, respectively.

In the actual experiments, two voltage signals are only read in the circuitry,  $\Delta V_1$  and  $\Delta V_2$ , across the reference resistance 1 and the shunt resistance. The calculation of  $\Delta V_{\text{heat}}$  and  $I_{\text{heat}}$  are given in Eqn. 3.1 and 3.2:

$$I_{\text{heat}} = I_{\text{sh}} - I_{\text{ref1}}, \text{ where } I_{\text{ref1}} = \frac{\Delta V_1}{R_{\text{ref1}}}, I_{\text{sh}} = \frac{\Delta V_2}{R_{\text{sh}}} \quad (3.1)$$

$$\Delta V_{\text{heat}} = \frac{\sum R_{\text{ref}(n)}}{R_{\text{ref1}}} \cdot \Delta V_1 \quad (3.2)$$

### **3.2 Surface temperature measurement by Infra-red (IR) camera**

A FLIR A-655sc IR camera is used to measure the heated surface temperature in real-time. The hotspot area is coated with black spray paint and the emissivity of the painted surface is determined by comparing the surface temperature measured by IR camera to the surface temperature measured by electrical resistance thermometry method.

Figure 3.7a shows the schematic of the IR measurement setup and calibration process. The fluid is heated up by the preheater installed before the test section, where the working fluid is pumped at high flowrates. The inlet and outlet fluid temperatures are measured by two calibrated K-type thermocouples, the average of the inlet and outlet temperatures,  $T_{\text{heater,avg}}$ , were used as reference point for IR thermometry calibration. The electrical resistance of the heater is also calibrated independently in an oven, and along with the average reference temperature (in agreement within 1 °C) are used to estimate the emissivity (~0.95) of the chip surface. See Figure 3.7b. Figure 3.7c shows typical IR images for the maximum removable heat flux, 298 W/cm<sup>2</sup> at the flow rate of 0.37 l/min. In this paper, the average heater surface temperature is measured by both electrical resistance thermometry and compared with the average IR temperature.

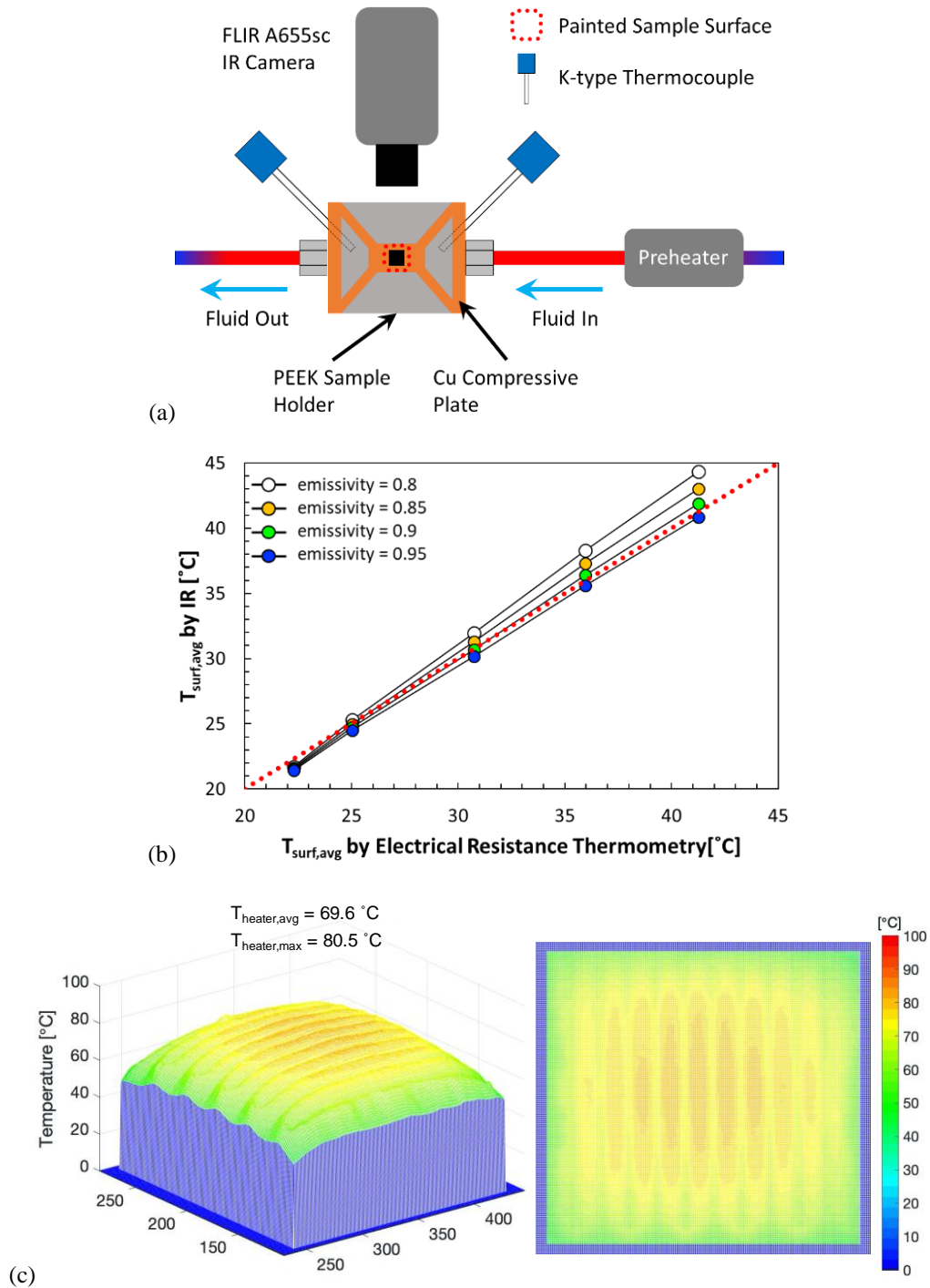


**Figure 3. 7** Description of the IR calibration procedure, (a) conceptual image of the IR measurement setup, (b) determination of the emissivity of the black body, emissivity of 0.95 performs best among others, (c) typical IR images showing surface temperature distribution of the heated surface from perspective and top views for  $298 \text{ W/cm}^2$ , single-phase R-245fa at flow rate of 0.37 l/min, the maximum and average heat temperatures are  $80.5$  °C and  $69.5$  °C, respectively. The size of heated surface is  $5 \times 5 \text{ mm}^2$ .

## Chapter 4

# Conjugate CFD simulations for single-phase study

This chapter describes parametric study of various EMMCs to improve thermofluidic performance at high heat flux condition. Full-scale CFD simulation is performed with quarter-cut EMMC designs. The EMMC designs have a  $5 \text{ mm} \times 5 \text{ mm}$  cold-plate footprint, and they are exposed to the heat flux of  $800 \text{ W/cm}^2$ . Single-phase DI water is used as a working fluid.

In Section 4.1, the CFD simulation domains and boundary conditions are explained. The governing equations and boundary conditions of the CFD domains are described and the method to characterize thermofluidic performance of the EMMCs is followed. Defined thermal resistance and pressure drop components are key parameters to compare the thermofluidic performance of each EMMC design.

In Section 4.2, three main approaches to improve the cooling performance yet minimize the pressure drop are proposed: modifying inlet/outlet conduits, reducing cold-plate substrate thickness, and increasing the effective cold-plate microchannel area. The changed thermofluidic behavior in each EMMC is plotted by thermal resistance and pressure drop as a function of changed geometric dimensions.

## 4.1 CFD simulation domains and boundary conditions

### 4.1.1 Description of Embedded Microchannels-3D Manifold Cooler (EMMC) design

The geometry of an EMMC, shown in Figure 4.1a consists of two Si substrates, one for a cold plate (CP) with embedded microchannels, and a 3D manifold for liquid delivery and extraction conduits. The fluid is introduced through fluid inlets placed at both ends of the manifold and flows through inlet plenums to multiple manifold inlet conduits. Once reached the intersections between the manifold inlet conduits and the CP microchannels, it is diverged, making a 90° turn and flows toward the bottom of the heated section of the CP microchannels. The fluid proceeds along the CP microchannels, exchanging heat with the heated surfaces followed by another 90° turn to exit through the adjacent manifold outlet conduits. A parameter called a unit length of fluid flow path,  $L_{flow}$ , is  $(W_{mani,in} + W_{mani,out})/2 + W_{mani,wall}$  that is defined as the distance that the fluid has to flow from a manifold inlet conduit to an adjacent manifold outlet conduit.

The dimensions of CP microchannels and manifold inlet/outlet conduits are control parameters and these parameters are highlighted in red (Figure 4.1b) and the dimensions of different CP and manifold designs are listed in Table 4.1 and Table 4.2.

**Table 4. 1** Geometry of different cold-plate designs

CP Design	$H_{cp}$ [ $\mu\text{m}$ ]	$W_{cp}$ [ $\mu\text{m}$ ]	$W_{cp,fin}$ [ $\mu\text{m}$ ]	$H_{cp,sub}$ [ $\mu\text{m}$ ]	$N_{cp}$
CP0	75	150	50	500	25
CP1	75	150	50	200	25
CP2	75	50	50	200	50
CP3	75	10	40	200	100
CP4	75	10	15	200	200

**Table 4. 2** Geometry of different manifold designs

Manifold Design	$W_{mani,in}$ [ $\mu\text{m}$ ]	$W_{mani,out}$ [ $\mu\text{m}$ ]	$W_{mani,wall}$ [ $\mu\text{m}$ ]	$L_{flow}$ [ $\mu\text{m}$ ]	$W_{mani,wall}/L_{flow}$ [%]	$N_{mani,in}$
M0'	150	482	100	416	24.04	6
M3	217	215	200	416	48.08	6

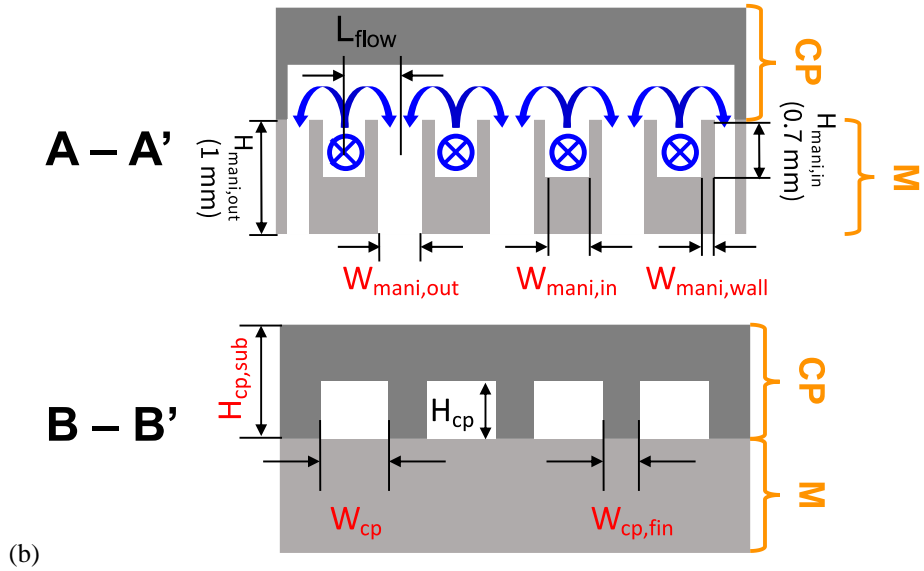
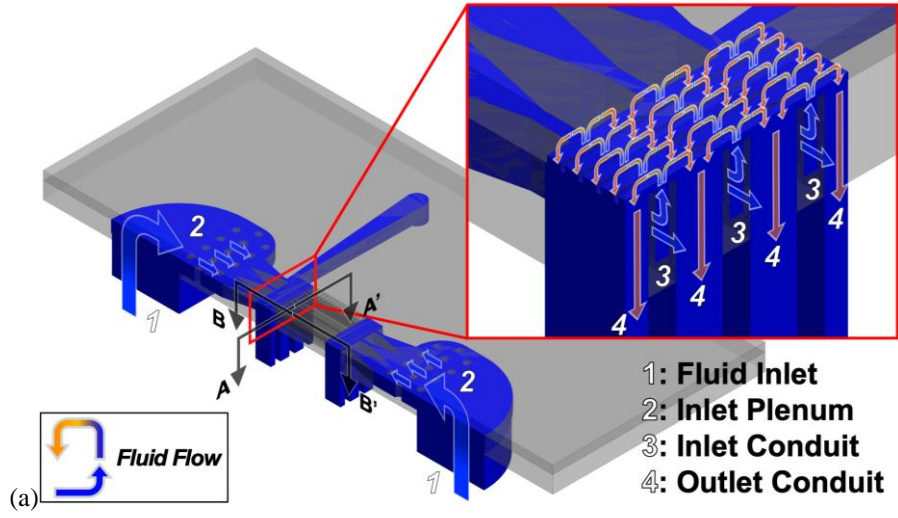


**Figure 4. 1** (a) Conceptual design of the embedded microchannels-3D manifold cooler (EMMC), (b) key geometric parameters of cold-plate and manifold in A-A' and B-B' cut views

### 4.1.2 Governing equations of CFD simulations

In this paper, the single-phase CFD simulations with conjugate heat transfer are performed to investigate thermofluidic behavior of the different EMMC designs. Steady-state, laminar, and incompressible flow conditions in three-dimensional fluid domain are assumed, and the governing equations for the conjugate CFD simulations are given as follows [CFD1]:

Continuity: 
$$\frac{\partial}{\partial x_i} (\rho \cdot u_i) = 0 \quad (4.1)$$

Momentum: 
$$\frac{\partial}{\partial x_i} (\rho u_i u_j) = -\frac{\partial P}{\partial x_j} + \frac{\partial}{\partial x_i} \left( \mu_f \frac{\partial u_j}{\partial x_i} \right) \quad (4.2)$$

Energy equation for fluid domain: 
$$\frac{\partial}{\partial x_i} (\rho u_i C_p T_f) = \frac{\partial}{\partial x_i} \left( k_f \frac{\partial T_f}{\partial x_i} \right) \quad (4.3)$$

Energy equation for solid domain: 
$$\frac{\partial}{\partial x_i} \left( k_s \frac{\partial T_s}{\partial x_i} \right) = 0 \quad (4.4)$$

### 4.1.3 Computational domains and boundary conditions

Since the device is symmetric in two directions, the solid and fluid domains are dissected along the symmetry lines in Figure 4.2. The solid domain consists of two joined Si bodies and four disconnected Au metal bodies. The fluid domain consists of continuous bodies, that fill the empty space inside the Si bodies, and two extended bodies attached to the fluid inlet and outlet. The fluid is divided into four discrete but continuous regions to investigate the contribution of each region's pressure drop to the total (Figure 4.3).

A constant heat flux, 11,985,378 W/m<sup>2</sup>, is applied at the top surface of the Au bodies to supply 800 W/cm<sup>2</sup> on the 5 x 5 mm<sup>2</sup> hot spot. All other solid outer walls are set to be adiabatic. No-slip and coupled wall boundary conditions are held at the interfaces between the solid domain and the fluid domain. Since the steady-state conjugate heat transfer problems are solved in the solid and fluid domains, a monolithic coupling method in the ANSYS Fluent v16.0 software is used to confirm the continuity of temperatures and heat fluxes at the solid-fluid interfaces:

Temperature continuity: 
$$T_{s,int} = T_{f,int} \quad (4.5)$$

Heat flux: 
$$k_s \left( \frac{\partial T_{s,int}}{\partial n} \right) = k_f \left( \frac{\partial T_{f,int}}{\partial n} \right) \quad (4.6)$$

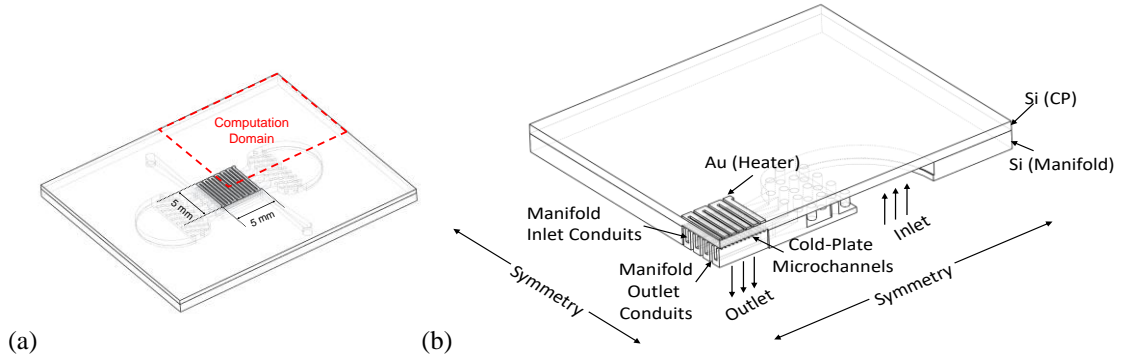


**Figure 4. 2** Full scale chip and a quarter-cut solid and fluid domains for conjugate CFD simulations.

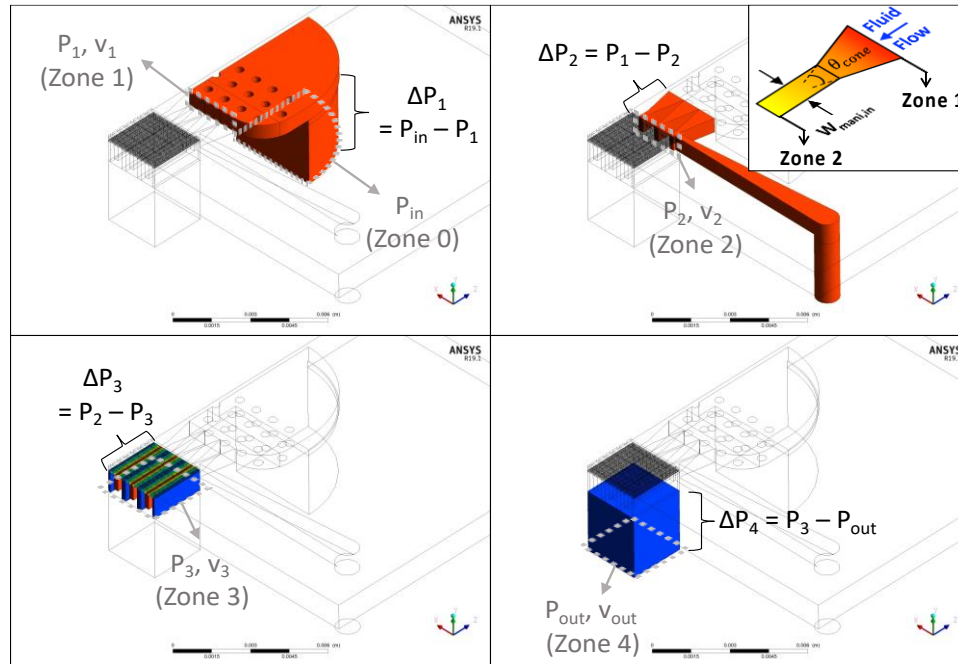


**Figure 4. 3** The fluid domain used in CFD simulations is divide into four discrete regions. **zone 0**: semicircular open area where the fluid is introduced to the device, **zone 1**: regions right after the inlet plenum where the gradual contraction begins, **zone 2**: regions right before the active cooling area where the gradual contraction is ended, **zone 3**: opens of the manifold outlet conduits that are connected to the exit plenum, **zone 4**: square open area where the fluid exits from the device.

The cut surfaces along the symmetry lines in the solid and fluid domains are set to be symmetric (Figure 4.2). Zero gauge-pressure condition is applied on the bottom surface of the fluid outlet, and a constant mass flow rate of  $8.3E-3$  kg/s and a constant temperature of 298.15 K are applied at the fluid inlet (Table 4.3).

**Table 4. 3** Simulation conditions

Conditions	Value
Mass flow rate at zone 0	8.3E-3 kg/s or 0.2 l/min @ 25 °C
Heat fluxes at the heated surfaces	800 W/cm <sup>2</sup>
Energy/Viscous Model	On/Laminar
Fluid inlet temperature	298.15 K
Au thermal conductivity	298 W/m-K
Si thermal conductivity	130 W/m-K
Water thermal conductivity	Piecewise-linear, Temperature dependent

#### 4.1.4 Characterization of thermo-fluidic behavior of EMMCs

In order to estimate the heat transfer and fluidic behavior of different EMMC designs, we investigated thermal resistances and pressure drops of each EMMC design.

Constant heat fluxes are supplied to the serpentine heater,  $q''_{\text{supply}}$ , and the supplied heat is transferred to the solid Au heater, to the solid Si body, and to the single-phase water. The transmitted heat to the working fluid,  $q_{\text{trans}}$ , can be estimated by measuring the change in sensible heat of the working fluid:

$$q_{\text{trans}} = \dot{m} \cdot \int_{T_{f,\text{in}}}^{T_{f,\text{out}}} C_{p,f}(T) dT \quad (4.7)$$

$C_{p,f}$  is the saturated specific heat of single-phase water that is temperature-dependent. Since the outer walls of the solid domain are adiabatic, an overall energy balance requires,  $q_{\text{supply}} - q_{\text{trans}}$ , must approach zero as the CFD simulation solution converges. In practice, we observed that while  $q_{\text{trans}}$  and  $\Delta P_{\text{total}}$  changes are less than 1%, even with excessively large number of mesh generated in the computational domain (see Appendix I), there is a residual 3% difference between  $q_{\text{supply}}$  and  $q_{\text{trans}}$ . Therefore, going forward we will use  $q_{\text{trans}}$  that translates to less than 3% error in calculations of the  $R_{\text{total}}$ .

The overall cooling performance of the EMMC can be described approximately by defining thermal resistances,  $R_{\text{total}}$ ,  $R_{\text{cond}}$ ,  $R_{\text{conv}}$ , and  $R_{\text{adv}}$ :

$$R_{\text{total}} = R_{\text{cond}} + R_{\text{conv}} + R_{\text{adv}} = \frac{T_{\text{heater,avg}} - T_{\text{f,in}}}{q''_{\text{trans}}} \quad (4.8a)$$

$$R_{\text{comp}} = R_{\text{cond}} + R_{\text{conv}} = \frac{T_{\text{heater,avg}} - T_{\text{cp,base,avg}}}{q''_{\text{trans}}} + \frac{T_{\text{cp,base,avg}} - T_{\text{f,out}}}{q''_{\text{trans}}} \quad (4.8b)$$

$$R_{\text{adv}} = \frac{T_{\text{f,out}} - T_{\text{f,in}}}{q''_{\text{trans}}} \quad (4.8c)$$

where  $R_{\text{cond}}$ ,  $R_{\text{conv}}$ ,  $R_{\text{adv}}$  are the conduction, convection, advection thermal resistances, respectively,  $R_{\text{comp}}$  is the composite thermal resistance consists of  $R_{\text{cond}}$  and  $R_{\text{conv}}$ ,  $q''_{\text{trans}}$  is the transferred heat to the single-phase water divided by the hotspot area, and  $T_{\text{heater,avg}}$ ,  $T_{\text{cp,base,avg}}$ ,  $T_{\text{f,in}}$ ,  $T_{\text{f,out}}$  are average temperatures of heater surface, CP microchannel base, inlet and outlet fluid, respectively. Here, we use the average temperature of the chip for calculation of the  $R_{\text{total}}$ , alternatively maximum temperature of the chip can be used to define the appropriate thermal resistance, which is more reasonable for device level reliability considerations or there are a large number of small hot spots distributed in addition to the uniform background power dissipation. The difference between average and maximum temperatures for the cases studied here are less than 10%, see Table D.3 in Appendix D.2.

The total pressure drop,  $\Delta P_{\text{total}}$ , in the EMMC is expressed as:

$$\Delta P_{\text{total}} = \Delta P_1 + \Delta P_2 + \Delta P_3 + \Delta P_4 \quad (4.9a)$$

where  $\Delta P_1$  is the pressure drop from the semicircular inlet opening (zone 0) and the end of the inlet plenum (zone 1),  $\Delta P_2$  is the gradual contraction pressure loss from the end of inlet plenum (zone 1) to the beginning of the manifold inlet conduits (zone 2),  $\Delta P_3$  is the pressure drop from the beginning of inlet conduits (zone 2) to the open ends of the manifold outlet conduits (zone 3), and  $\Delta P_4$  is the expansion pressure loss from the open ends of the manifold outlet conduits (zone 3) to the square outlet opening (zone 4). In general,  $\Delta P_1$  and  $\Delta P_4$  are almost constant despite the geometric changes of the control parameters significantly impact  $\Delta P_2$  and  $\Delta P_3$ . Therefore, the change of  $\Delta P_{\text{total}}$  between different EMMC designs,  $\Delta(\Delta P_{\text{total}})_{D_x \rightarrow D_y}$ , is highly dependent to the change of  $\Delta P_2$  and  $\Delta P_3$ ,  $\Delta(\Delta P_2)_{D_x \rightarrow D_y}$  and  $\Delta(\Delta P_3)_{D_x \rightarrow D_y}$ :

$$\Delta(\Delta P_{\text{total}})_{Dx \rightarrow Dy} \cong \Delta(\Delta P_2)_{Dx \rightarrow Dy} + \Delta(\Delta P_3)_{Dx \rightarrow Dy} \quad (4.9b)$$

## 4.2 Results and discussion of parametric study in EMMCs

### 4.2.1 General guidelines for the EMMC design improvement

The goal of the design improvement is to find EMMC designs that achieve the lowest thermal resistance with a moderate system pressure drop, i.e. less than 10's of kPa, for the single-phase cooling applications.

In the baseline EMMC design, the  $R_{\text{total}} \sim 0.097 \text{ cm}^2\text{-K/W}$  consists of advection ( $R_{\text{adv}}$ ), conduction ( $R_{\text{cond}}$ ) and convection ( $R_{\text{conv}}$ ) thermal resistances. For a given heat flux, the advection thermal resistance is fixed, and represents  $\sim 18 \%$  of the total thermal resistance. However, there is room to reduce conduction and convection thermal resistances that represent about 82 % of the total thermal resistance, see Figure 4.4. Therefore, reducing total thermal resistance by changing EMMC's geometries is the main focus in this paper. At the same time, the expected system pressure drop after each improvement step is also analyzed where we attempted to manage it by optimizing the 3D-manifold geometry and form factor.

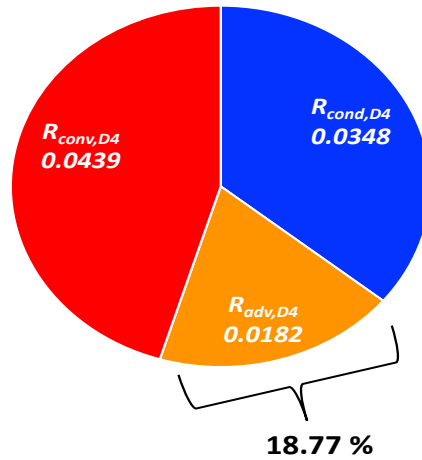


**Figure 4. 4** Composition of each thermal resistance component in the baseline EMMC design, D4

## 4.2.2 A summary of the parametric study in EMMCs

Figure 5 represent a summary of the parametric study of EMMCs performance, thermal resistance vs. total pressure drop, using CFD simulations for single-phase water. The chosen starting point or the baseline is design D4 since we have already fabricated, conducted tests and conducted extensive CFD simulations. The CFD results agree well with the experimental data. Before getting into the detailed analysis of the CFD results that will be presented in the next section, we would like to take the opportunity and summarize the overall trend in thermal resistances and associated pressure drops for successive design improvement attempts. We iterate that this is not a systematic approach rather examining the impact of various geometry dimensions, while seeking successive design improvements from D4 to D9.

The baseline designs D4,  $R_{\text{total}} = 0.10 \text{ cm}^2\text{-K/W}$  and  $\Delta P_{\text{total}} = 8 \text{ kPa}$ , was originally optimized for two-phase application with inlet to outlet channel dimension ratio of 1 to 3. It is well established that for a single-phase cooling, a symmetric inlet to outlet widths reduce the flow bypass, represented by design D5, will both improve the thermal resistance,  $R_{\text{total}} = 0.095 \text{ cm}^2\text{-K/W}$ , and pressure drop  $\sim 5\text{kPa}$ . In design D6, the silicon chip thickness was reduced from 500 to 200  $\mu\text{m}$  that resulted in a reduction in thermal resistance to  $0.075 \text{ cm}^2\text{-K/W}$ , pressure drop is slightly increased but that could be due to temperature-dependent thermophysical properties of the working fluid. In order to achieve even lower thermal resistances, we further reduced the  $\mu$ -channel width from 150  $\mu\text{m}$  (D6) to 50  $\mu\text{m}$  (D7) and 10 $\mu\text{m}$  (D8), at the expense of larger pressure drops up to 80 kPa. In the next step, we attempted to reduce the large pressure drop in design while maintaining the same thermal performance by modifying the 3D manifold channel geometries to arrive at design D9. Clearly, we achieved nearly a factor of 2 improvement in pressure drop, from 80 kPa (D8) to 35 kPa (D9), and about 7 % reduction in thermal resistance from  $R_{\text{total}} = 0.044 \text{ cm}^2\text{-K/W}$  (D8) to  $R_{\text{total}} = 0.041 \text{ cm}^2\text{-K/W}$  (D9).

Additional information regarding the temperature uniformity and distribution as well as inlet and outlet fluid temperatures, hydraulic diameter and Re numbers for designs D4 to D9, are outlined in Appendix D.2.

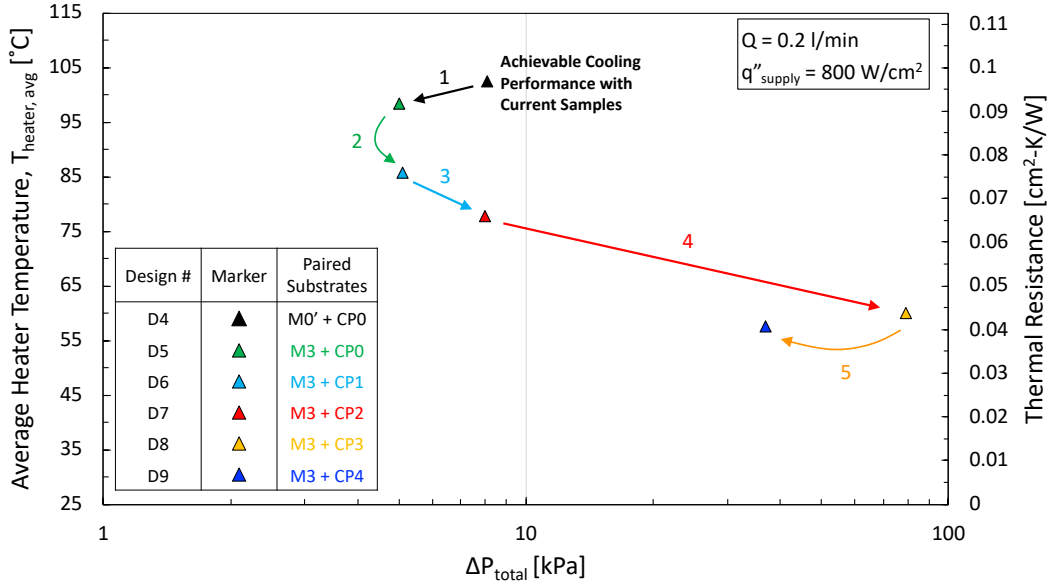
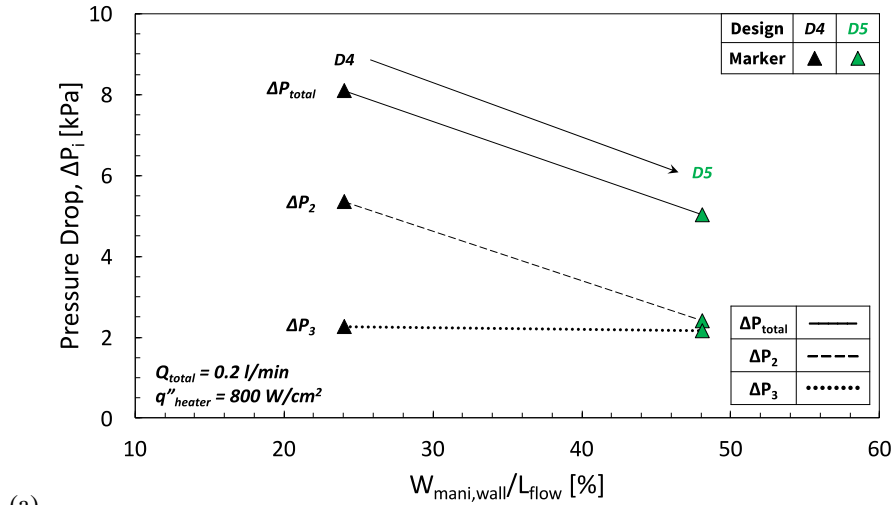


**Figure 4.5** A summarized conjugate CFD simulation results to show the design improvement process by plotting data in average surface temperatures and corresponding thermal resistances vs.  $\Delta P_{total}$ . Effect of symmetric distribution of manifold inlet/outlet conduits (1), effect of CP thickness (2), effect of fluid-solid interfacial area in cold-plate microchannels (3 – 5) are studied in the following sections. Also see Appendix D.2, Table D.3 for more details for designs D4 to D9.

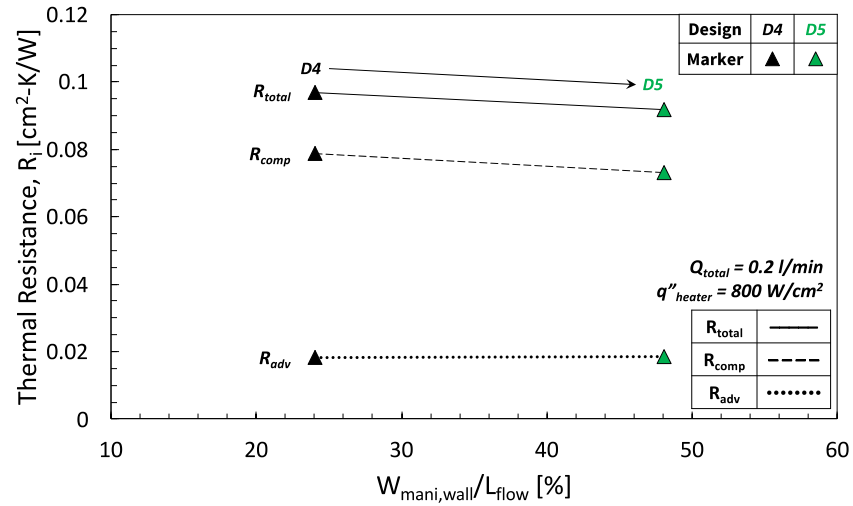
## 4.2.3 More detailed analyses of the parametric study of the EMMCs

### 4.2.3.1 Improvement from Design D4 to D5: Modifying the inlet/outlet conduits

The baseline EMMC design D4, Jung, et al. [44], was originally intended for two-phase heat transfer. As such the outlet conduits are 3 times wider than inlet conduits to accommodate the sudden expansion of vapor volume. When the inlet/outlet conduits are symmetrically placed in the EMMC, the  $\Delta P_{total}$  for D5 design, is reduced by 38.0 % from baseline design D4 (Figure 4.6a). The reduction in  $\Delta P_{total}$  is mainly attributed to the reduction in  $\Delta P_2$  rather than  $\Delta P_3$ , where  $\Delta P_2$  contributes to 96% of reduction in  $\Delta P_{total}$ . This is because  $\Delta P_2$  is greatly impacted by the size of  $W_{mani,in}$  while  $\Delta P_3$  is linked to the average fluid velocity in zone 2,  $v_2$ . For even more extensive analysis and details, please see Appendix D.3.



(a)



(b)

**Figure 4. 6** Pressure drop and thermal resistance vs.  $W_{\text{mani,wall}}/L_{\text{flow}}$  results (D4/D5).

The total thermal resistance,  $R_{\text{total,D5}}$  decreases from  $R_{\text{total,D4}}$  by 5.5 %, see Figure 4.6b. The changed  $R_{\text{total}}$  is almost identical to the changed  $R_{\text{comp}}$ .  $L_{\text{flow}}$  is defined by  $N_{\text{mani,in}}$  and remains constant, so  $W_{\text{mani,wall}}$  is the parameter that determines the amount of bypassed fluid between the manifold inlet/outlet conduits. As  $W_{\text{mani,wall}}/L_{\text{flow}}$  in D5 is doubled from D4, the amount of bypassed fluid is reduced. Therefore, improvement in  $R_{\text{total}}$  in D5 is expected due to reduced  $R_{\text{comp}}$ . As expected, the advection thermal resistance remains the same from design D4 to D5.

**Table 4. 4** Key geometries and CFD results (D4/D5)**a. Key geometries (D4/D5)**

Geometry	D4	D5
$N_{\text{mani}}$	6	6
$\theta_{\text{cone}} [^\circ]$	25.8	23.3
$W_{\text{mani,in}} [\mu\text{m}]$	150	217
$W_{\text{mani,wall}}/L_{\text{Flow}} [\%]$	24.04	48.08

**b. Key CFD results (D4/D5)**

Design Resulting Parameters		D4	D5
$\Delta P_{\text{total}}$	[kPa]	8.1	5.0
$\Delta P_2$		5.4	2.4
$R_{\text{total}}$	[cm <sup>2</sup> -K/W]	.0970	.0917
$R_{\text{comp}} (= R_{\text{cond}} + R_{\text{conv}})$		.0788	.0732

**4.2.3.2 Improvement from Design D5 to D6: Effect of cold plate thickness**

The most practical way to improve the cooling performance of EMMC is to minimize the conduction thermal resistance by reducing conduction heat transfer pathway. In this section, the effect of CP substrate thickness on the thermo-fluidic performance of the EMMC is analyzed by comparing D5 and D6. The substrate thickness of CP,  $H_{\text{cp,sub}}$ , is reduced by 300  $\mu\text{m}$  from D5 to D6 but other geometric dimensions are maintained. The absolute value of changed in  $\Delta P_{\text{total}}$  between D5 and D6 is 0.09 kPa, that is only 1.83 % of  $\Delta P_{\text{total,D5}}$ , 5.11 kPa. We estimate the error in CFD simulation of the pressure drop to be  $\sim 0.5\%$ , the remaining percentage difference is attributed to temperature-dependent thermophysical properties of water between 70 °C to 74 °C .

**Table 4. 5** Key CFD results (D5/D6)

Design Resulting Values	D5	D6
$\Delta P_{\text{total}}$ [kPa]	5.0	5.1
$R_{\text{total}}$ [cm <sup>2</sup> -K/W]	.0917	.0758
$R_{\text{comp}} (= R_{\text{cond}} + R_{\text{conv}})$ [cm <sup>2</sup> -K/W]	.0732	.0576

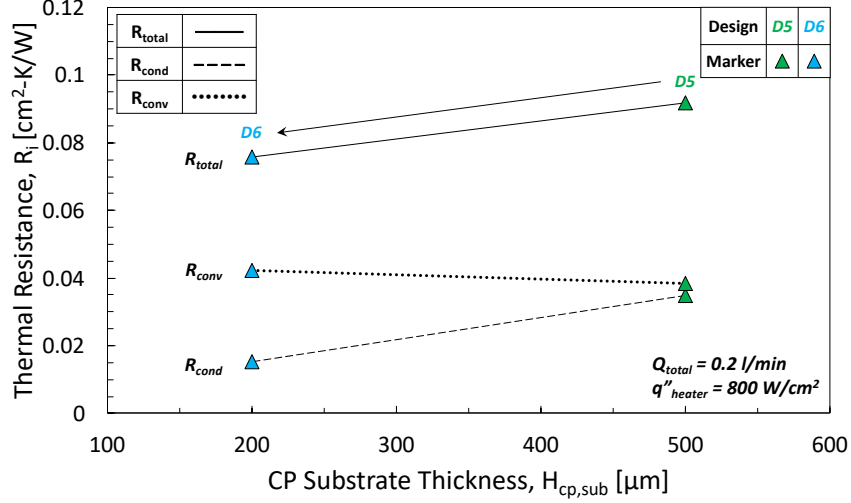


**Figure 4. 7** Thermal resistance vs.  $H_{cp,sub}$  (D5/D6)

The thermal resistance,  $R_{total,D6}$ , is reduced by ~17% from  $R_{total,D5}$  (Figure 7), mainly due to the reduction in  $R_{cond}$ :

$$\Delta(R_{cond})_{est} = \frac{\Delta(H_{cp,sub})_{D5 \rightarrow D6}}{k_{Si}} \cong 0.0231 \left[ \frac{\text{cm}^2 - \text{K}}{\text{W}} \right]$$

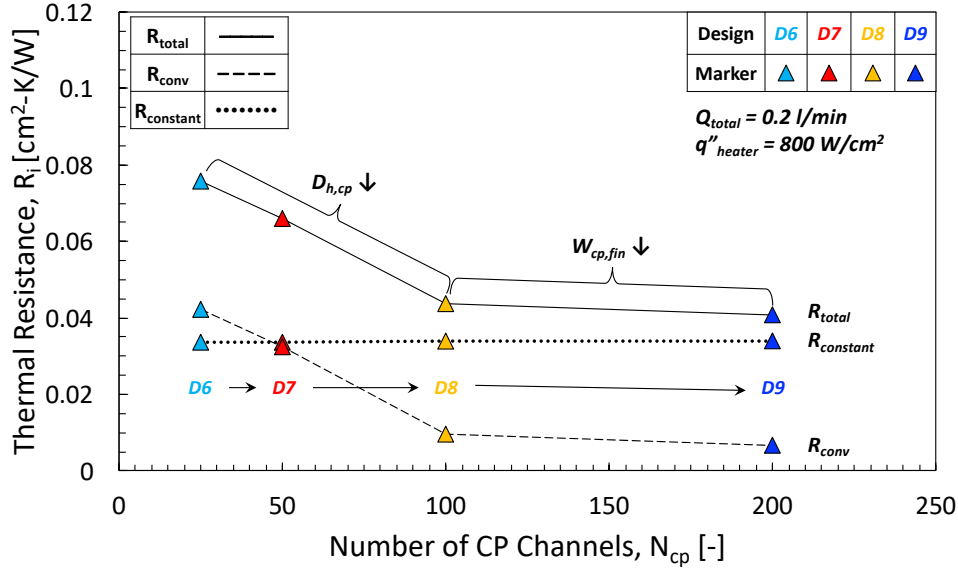
$$\Delta(R_{cond})_{CFD} = R_{cond,D5} - R_{cond,D6} \cong 0.0195 \left[ \frac{\text{cm}^2 - \text{K}}{\text{W}} \right]$$

where  $\Delta(R_{cond})_{est}$  is the an estimate of reduced  $R_{cond}$  when  $H_{cp,sub}$  decreases by 300 $\mu\text{m}$ .  $\Delta(R_{cond})_{CFD}$  accounts for 2D heat spreading. There is a slight increase in estimation of  $R_{conv}$  from D5 design to D6, very likely due to 2D heat spreading vs. 1D conduction.

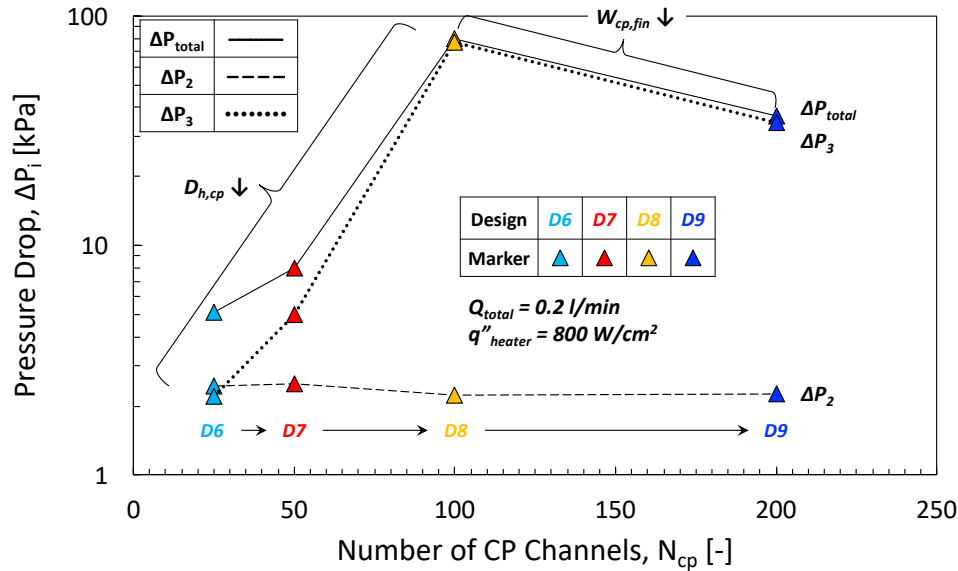
#### 4.2.3.3 Improvement from Design D6 to D7, D8, and D9: Increasing the effective CP microchannel area

There are two ways to increase the effective area for heat exchange between the fluid and the CP microchannels, namely by reducing  $W_{cp}$ , and  $W_{cp,fin}$ , see Figure 1b and Table 4.6a.

We first start with reducing  $W_{cp}$ , from 150  $\mu\text{m}$  to 50  $\mu\text{m}$  to 10  $\mu\text{m}$ , for D6, D7 and D8 designs, respectively. In Figure 8-a, the  $R_{total}$  is plotted as a function of the number of CP microchannels,  $N_{cp}$ . As the  $N_{cp}$  is doubled from D6 to D7, and from D7 to D8, the  $R_{total}$  linearly decreases by 13.0 % and 33.8 %, respectively.



(a)



(b)

**Figure 4. 8** Thermal resistance and pressure drop vs.  $N_{cp}$  (D6/D7, D7/D8/D9)

In the second step, in order to manage the excessive pressure drop ( $\sim 80 \text{ kPa}$ ) for design D8, we further reduce  $W_{cp,fin}$  from 40 to 15  $\mu\text{m}$ . This results in further reduction in  $R_{total}$  by 6.8 % from D8 to D9 with doubling  $N_{cp}$ . This happens because the contribution of the  $R_{conv}$  to the  $R_{total}$  diminishes.

Table 4.6b shows thermal resistance components for the EMMCs designs D6 to D9 as the effective CP microchannels area is successively increases. Clearly, the  $R_{conv}$  is the only parameter that decreases with increasing number of  $N_{cp}$ , while  $R_{cond}$  and  $R_{adv}$  remain constant (lower limit of  $0.034 \text{ cm}^2\text{-K/W}$ ). As shown in Figure 4.8b, the pressure drop is

increased with reducing  $W_{cp}$ , from 150  $\mu\text{m}$  to 50  $\mu\text{m}$  to 10  $\mu\text{m}$ , for D6, D7 and D8 designs, respectively. Reducing  $W_{cp,fin}$  from 40 to 15  $\mu\text{m}$ , accommodates more microchannels in the cold-plate such that the average mass flow rate/cooling channel, and therefore pressure is reduced from design D8 and D9. For a more detailed analysis of the pressure drop components to the total pressure drop, please consult with Appendix D.4.

**Table 4. 6** Key CFD geometries and results (D6-D9)

**a** Key CFD geometries (D6-D9)

Geometry	D6	D7	D8	D9
$N_{cp}$	25	50	100	200
$D_{h,cp}$ [ $\mu\text{m}$ ]	100	60	17.6	17.6
$W_{cp,fin}$ [ $\mu\text{m}$ ]	50	50	40	15
$A_{wet}$ [ $10^{-5}\text{m}^2$ ]	5.625	6.25	8.5	17

**Table 4.6b** Key CFD results (D6-D9)

Resulting Values \ Design	D6	D7	D8	D9
$\Delta P_{total}$ [kPa]	5.1	8.0	79.3	36.9
$\Delta P_3$ [kPa]	2.2	5.0	76.6	34.2
$R_{total}$ [ $\text{cm}^2\text{-K/W}$ ]	.0758	.0660	.0437	.0408
$R_{constant}$ (= $R_{cond} + R_{adv}$ ) [ $\text{cm}^2\text{-K/W}$ ]	.0336	.0336	.0340	.0340
$R_{conv}$ [ $\text{cm}^2\text{-K/W}$ ]	.0423	.0324	.0098	.0068

# Chapter 5

## Results and discussion

This chapter describes hydraulic and thermal behavior of the proposed EMMC design with single and two-phase DI water/R-245fa. A parametric study of the developed correlations [57-61] is conducted to understand the thermo-fluidic performance of the given EMMC design. Furthermore, we propose new correlations to predict friction factors and Nusselt numbers of the tested heat exchangers by the parametric study of the conjugate CFD simulations. In Section 5.1 we introduce analytic tools to interpret experimentally measured data to understand thermo-fluidic behavior of the EMMC. The same method for data reduction is also applied to the CFD simulation results. In Section 5.2 the thermo-fluidic performance of the tested EMMCs with DI water and R-245fa is investigated. The single-phase test results are validated by the conjugate CFD simulation results over the wide range of heat fluxes and flow conditions (Section 5.2.1, Section 5.2.2). The two-phase test results with R-245fa are following in Section 5.2.3. Forced-convective subcooled boiling is the dominant cooling scheme for the two-phase heat transfer and we will discuss how the thermo-fluidic behavior changes with respect to the exit vapor quality.

### 5.1 Theoretical analysis for data reduction

The metal serpentine heater is powered by Joule heating,  $q_{\text{heater}}$ , and it is calculated by multiplying the voltage drop across the heater,  $\Delta V_{\text{heater}}$ , and the current flowing through the heater,  $I_{\text{heater}}$ .

$$q_{\text{supply}} = \Delta V_{\text{heater}} \cdot I_{\text{heater}} \quad (5.1)$$

The supplied heat is transferred from the metal layer to the bulk Si, to the working fluids, DI water or R-245fa. The net heat transferred to the fluid,  $q_{\text{trans}}$ , is estimated by observing the sensible heat change of the fluid:

$$q_{\text{trans}} = q_{\text{supply}} - q_{\text{loss}} = \dot{m} \cdot \int_{T_{f,\text{in}}}^{T_{f,\text{out}}} C_p(T) dT = \sum_{i=1}^n dq_{\text{trans},i} \quad (5.2a)$$

$$dq_{\text{trans},i} = \dot{m} \cdot \frac{C_{p,i} + C_{p,i+1}}{2} \cdot \frac{T_{f,\text{out}} - T_{f,\text{in}}}{n}, n = \frac{T_{f,\text{out}} - T_{f,\text{in}}}{\delta_T} \quad (5.2b)$$

where  $C_p$  is the saturated specific heat of single-phase R-245fa and it is temperature-dependent. If we define the finite interval of temperature,  $\delta_T$ , as 0.1 °C, the number of intervals between  $T_{f,\text{out}}$  and  $T_{f,\text{in}}$ ,  $n$ , is determined and the finite  $q_{\text{trans}}$  at  $i^{\text{th}}$  interval,  $dq_{\text{trans},i}$ , can be calculated. The numerical integration of  $dq_{\text{trans},i}$  is the overall transmitted heat to the working fluid. Since the heater is made of pure metal layers, Ti and Au, the resistance of the heater,  $Z_{\text{heater}}$ , is linearly changed as the heater temperature is changed:

$$T_{\text{heat,avg}} = T_0 + \frac{Z_{\text{heat}} - Z_0}{\alpha \cdot Z_0}, Z_{\text{heat}} = \frac{\Delta V_{\text{heat}}}{I_{\text{heat}}} \quad (5.3)$$

where  $T_0$  is the room temperature,  $Z_0$  is the heater resistance at the room temperature,  $\alpha$  is the temperature coefficient of resistance (TCR) of the heater.

The cooling performance of the EMMC can be described by the total thermal resistance,  $R_{\text{total}}$ , and it consists of multiple terms:

$$R_{\text{total}} = R_{\text{cond}} + R_{\text{conv}} + R_{\text{adv}} = \frac{T_{\text{heat,avg}} - T_{f,\text{in}}}{q''_{\text{trans}}} \quad (5.4a)$$

$$R_{\text{cond}} = \frac{T_{\text{heat,avg}} - T_{\text{cp-base,avg}}}{q''_{\text{trans}}} \quad (5.4b)$$

$$R_{\text{conv}} = \frac{T_{\text{cp-base,avg}} - T_{f,\text{ref}}}{q''_{\text{trans}}} \quad (5.4c)$$

$$R_{\text{adv}} = \frac{T_{f,\text{ref}} - T_{f,\text{in}}}{q''_{\text{trans}}} \quad (5.4d)$$

where  $R_{\text{cond}}$  is the conduction thermal resistance in solid substrates,  $R_{\text{conv}}$  is the convection thermal resistance between the CP microchannel wall and the working fluid,  $R_{\text{adv}}$  is the advection thermal resistance that indicates the increase in the average temperature of the fluid.

The effective heat transfer coefficient,  $h_{\text{effect}}$ , is defined as a convective heat transfer rate at the CP microchannel walls and it is expressed as:

$$h_{\text{effect}} = \frac{q_{\text{trans}}}{\eta_o \cdot (T_{\text{cp-base,avg}} - T_{\text{f,ref}}) \cdot A_{\text{wet}}} \quad (5.5)$$

where  $\eta_o$  is overall fin efficiency,  $T_{\text{cp-base,avg}}$  is the average temperature of the CP microchannel base that is calculated by conduction resistance across the metal/SiO<sub>2</sub>/Si layers.

$$\eta_o = 1 - \frac{N_{\text{cp}} \cdot A_{\text{fin}}}{A_{\text{wet}}} \cdot (1 - \eta_{\text{fin}}) \quad (5.6a)$$

$$\eta_{\text{fin}} = \frac{\tanh(m \cdot H_{\text{cp}})}{m \cdot H_{\text{cp}}}, m = \sqrt{\frac{2 \cdot h_{\text{effect}}}{k_{\text{Si}} \cdot w_{\text{cp,fin}}}} \quad (5.6b)$$

$$T_{\text{cp-base,avg}} = T_{\text{heat,avg}} - q''_{\text{trans}} \cdot \sum_i \frac{\delta_i}{k_i} \quad (5.6c)$$

where  $N_{\text{cp}}$  is the number of CP microchannels and  $\eta_{\text{fin}}$  is the individual fin efficiency. The reference fluid temperature,  $T_{\text{f,ref}}$ , is the average fluid temperature between inlet and outlet if  $x_{\text{out}} \leq 0$ . For the heat fluxes where  $x_{\text{out}} > 0$ , estimation of  $T_{\text{f,ref}}$  becomes more complicated. Since the dominant two-phase heat transfer is forced-convective subcooled boiling along the microchannels, the fluid temperature is assumed to linearly increase up to the local Onset-of-Nucleate Boiling (or ONB) point,  $z_{\text{ONB}}$ , in the microchannels and linearly increase again along the remaining channels. Therefore,  $T_{\text{f,ref}}$  is estimated by length-weighted averaging fluid temperature along the CP microchannel:

$$T_{\text{f,ref}} = \begin{cases} \frac{T_{\text{f,in}} + T_{\text{f,out}}}{2}, & \text{if } x_{\text{out}} \leq 0 \\ \frac{T_{\text{f,in}} + T_{\text{f,ONB}}}{2} \cdot \frac{z_{\text{ONB}}}{L_{\text{cp}}} + \frac{T_{\text{f,ONB}} + T_{\text{f,out}}}{2} \cdot \left(1 - \frac{z_{\text{ONB}}}{L_{\text{cp}}}\right), & \text{if } x_{\text{out}} > 0 \end{cases} \quad (5.7)$$

The effective heat transfer coefficient is first calculated by assuming the fin efficiency of unity in Eqn. (5.5). After then, the fin efficiency is iterated until the  $h_{\text{effect}}$  is converged. In this paper, the calculated  $\eta_o$  for all test cases is  $\sim 0.99$ .

The total pressure drop in the EMMC,  $\Delta P_{\text{total}}$ , is described as follows:

$$\Delta P_{\text{total}} = \Delta P_1 + \Delta P_2 + \Delta P_3 + \Delta P_4 \cong \Delta P_2 + \Delta P_3 \quad (5.8)$$

where  $\Delta P_1$  is the pressure drop from the inlet openings to the inlet plenums,  $\Delta P_2$  is the pressure drop within the gradual contraction regions, from the end of the inlet plenums to the beginning of the active cooling region,  $\Delta P_3$  is the pressure drop where the convective heat transfer occurs,  $\Delta P_4$  is the expansion pressure drop after the fluid exits through the manifold outlet conduits. According to the CFD simulations by Jung, et al. [43,55], the fluid across the manifold inlet conduits is uniformly distributed. In addition, it was concluded that the sum of  $\Delta P_1$  and  $\Delta P_4$  contributes to less than 5 – 6 % of  $\Delta P_{\text{total}}$  based on the conjugate CFD simulation results. A rough estimation of the  $\Delta P_2$  and  $\Delta P_3$  values are outlined in Section 5.2.1.3.

## 5.2 Test results with EMMCs

DI water and R-245fa are the working fluids for all test cases. With DI water, we carefully established that single-phase flow and heat transfer prevails even for the highest power dissipation in the experiments,  $1100 \text{ W/cm}^2$ , and the lowest flow rates, 33 g/min. The detailed test conditions are summarized in Appendix A.1. We organized the results in the form of temperature vs. pressure drop, thermal resistance/heat transfer coefficient vs. flow rate/pressure, and total pressure drop vs. flow rate, etc. For all single-phase test cases, we compare the experimental data with the results of the conjugate thermal fluid flow numerical simulations, detailed in Appendix A.2 and A.3.

## 5.2.1 Single-phase DI water

### 5.2.1.1 Temperature Behavior

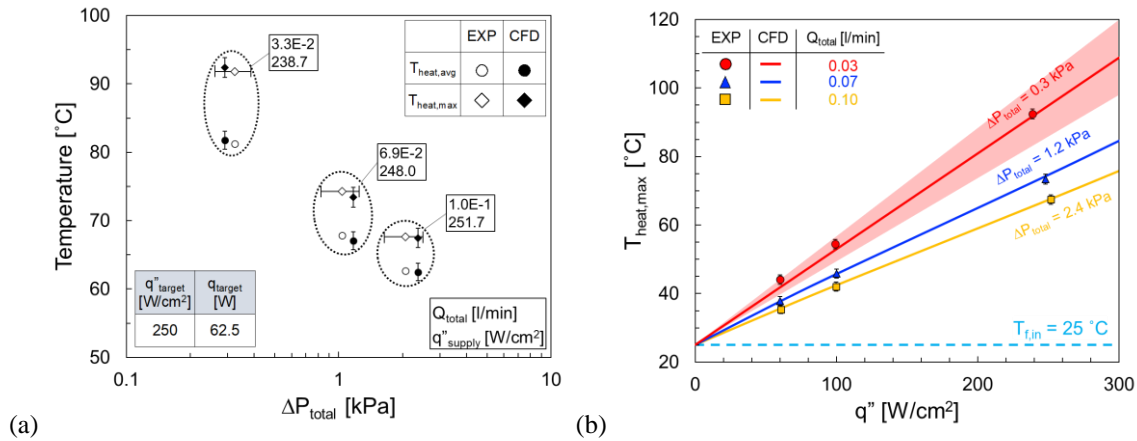


**Figure 5. 1** The experimental data and numerical simulation results for (a)  $T_{heat,max}$  or  $T_{heat,avg}$  vs.  $\Delta P_{total}$ , for the highest flow rate and heat flux of 0.1 l/min and 250 W/cm<sup>2</sup>, respectively; dimensions for the microchannel and 3D-manifold conduits are listed in Table 2.1. The uncertainty in pressure drop from simulations, is mainly associated with variations of the microfabricated channel dimensions. The numerical values of the maximum and average temperatures, flow rate, pressure drop for the 9 test cases are listed in Table A.5, (b) maximum surface temperature vs. heat flux for flow rates 0.03, 0.07 & 0.1 l/min. The “semi-transparent” red region, flow rate 0.03 l/min, represents  $\pm 10\%$  uncertainty levels in CFD predictions associated with variations in  $\mu$ -cooler channel and manifold conduits dimensions.

Figure 5.1(a) shows the maximum and average temperature of the heater vs. pressure drop for given flow rates (0.03, 0.07 and 0.1 l/min) and heat fluxes (60, 100 and 250 W/cm<sup>2</sup>) along with the numerical simulation results. The pressure drop across the  $\mu$ -cooler is  $< 3$  kPa for all flow rates. The maximum and average temperatures of the heated surface for any given heat flux are reduced as the flow rate increases. As the heat flux increases at a constant flow rate, both maximum and average temperatures of the chip also increase. The CFD results for temperature and pressure agree well with the experimental data (Figure 5.1a, 5.1b). The slight discrepancy between the measured and simulated pressures are due to potential variation in the dimensions of the microfabricated channels from the target nominal values. The associated uncertainty of heater temperature is quantified in Appendix B.1 and is estimated to be 1.4 – 3.1 %. The EMMC device is capable of removing 250 W/cm<sup>2</sup> (experimental data:  $T_{heat,max} = 90^\circ C$ )

and potentially up to  $850 \text{ W/cm}^2$  (numerical simulations:  $T_{\text{heat,max}} = 158^\circ\text{C}$ ) with only 2.4 kPa pressure drop for flow rate of 0.1 l/min, see Figure B.4. We have not tested the potential maximum heat flux during the experiments because the initial goal is not to check the critical heat flux of the sample, but to show minimal system pressure drop while moderate to high level heat fluxes are applied. The system pressure drop should be kept as low as possible to increase the system's coefficient of performance (COP), and the detailed information about the system pressure drop will be discussed in Section 5.2.1.3.

After the initial goal of the current work is achieved, we continue testing higher flow rates, 200 – 400 g/min, to remove up to or higher than  $1 \text{ kW/cm}^2$  of the supplied heat fluxes with single-phase DI water.

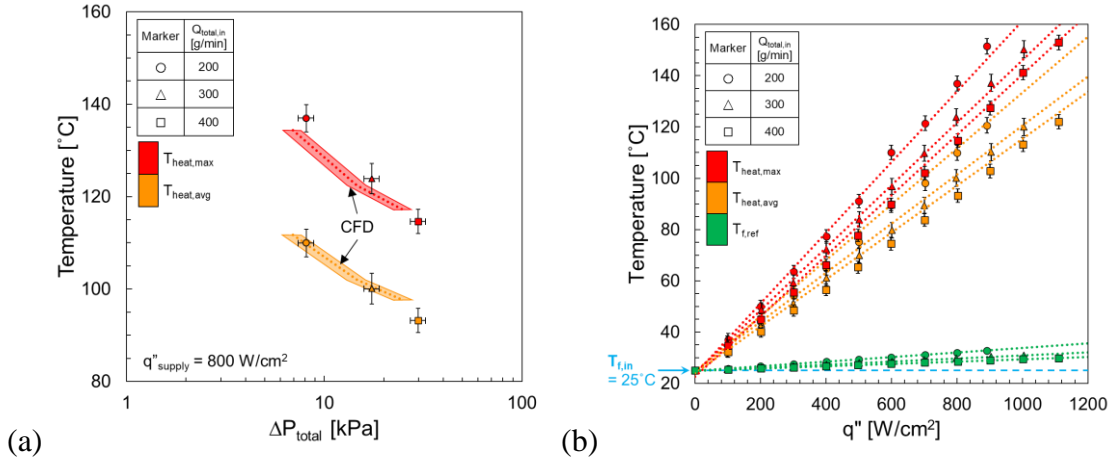


**Figure 5. 2** The experimental data and numerical simulation results for (a)  $T_{\text{heat,max}}$  or  $T_{\text{heat,avg}}$  vs.  $\Delta P_{\text{total}}$ , for the flow rates from 200 to 400 g/min, at the supplied heat flux of  $800 \text{ W/cm}^2$ . Two semi-transparent polygons filled with semi-transparent red and orange colors are estimated temperature and pressure drop results by CFD, (b)  $T_{\text{heat,max}}$ ,  $T_{\text{heat,avg}}$ ,  $T_{f,\text{ref}}$  vs.  $q''$  for the flow rates from 200 to 400 g/min, dotted lines represent the estimated  $T_{\text{heat,max}}$ ,  $T_{\text{heat,avg}}$ ,  $T_{f,\text{ref}}$  as a function of  $q''$ .

In general, the experimentally measured temperature and pressure drop results agree well with the CFD simulation results. The heat fluxes up to or higher than  $1 \text{ kW/cm}^2$  can be removed with increased flow rates, 300 or 400 g/min, while keeping the heated surface temperature below  $150^\circ\text{C}$ . In return, the significant pressure drop is inevitable (Figure 5.2a), that will be discussed further in Section 5.2.1.3 and 5.2.1.4. The temperatures and pressures at the inlet and outlet of the manifold are monitored to check energy balance

and observe incipient boiling event at the extreme heat fluxes. Based on this basic procedure, we confirm that the heat inputs for all test cases in Figure 5.2 are less than the value required to reach the saturation temperature at the given pressure level. Further discussion regarding onset-of-nucleate boiling, or ONB, is in Section B.2 that requires additional microchannel wall temperature information.

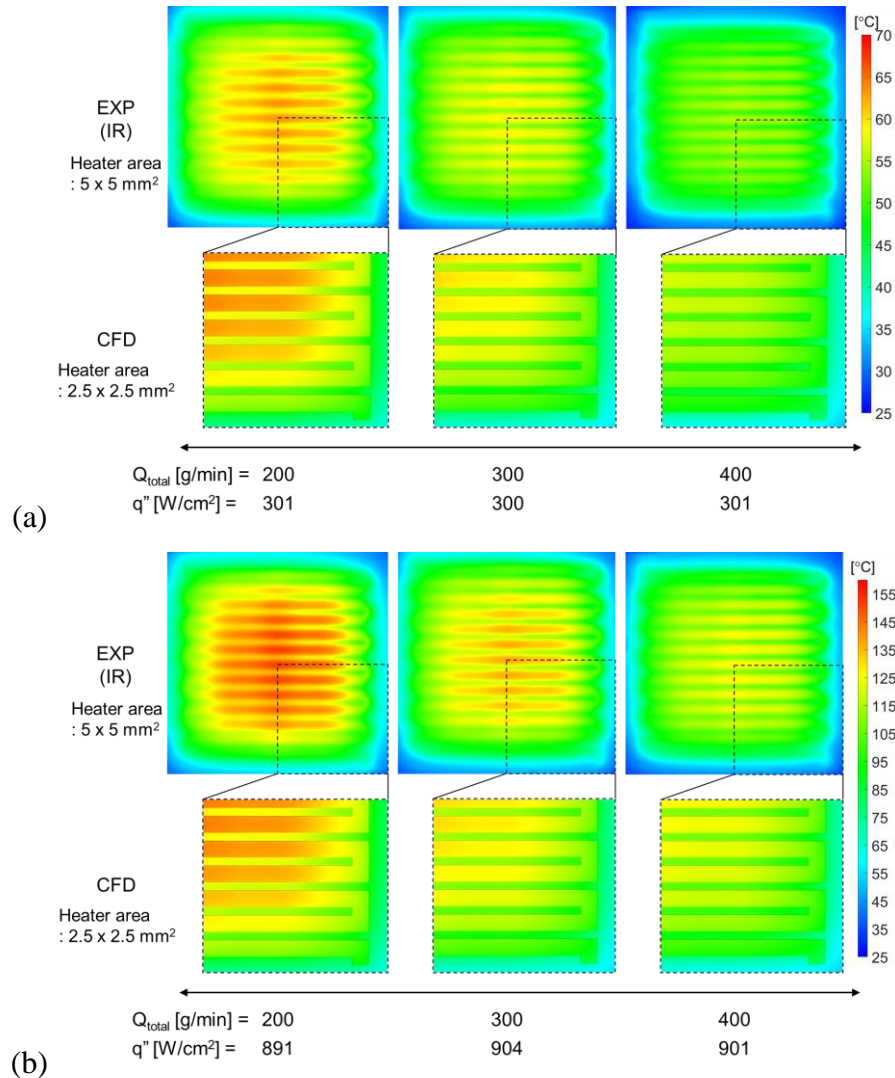


**Figure 5. 3** Captured thermal images from the IR camera and the CFD simulations. The thermal images from the CFD simulations are quarter-cut due to the defined CFD simulation domains. In general, temperature uniformity across the hotspot improves with the increased flow rate due to enhanced heat transfer rate. (a) At the heat flux of 300 W/cm<sup>2</sup>, temperature distribution in the IR images and the CFD images is almost identical (confirmed in Figure 5.2b). However, (b) more intensive and wider local hotspots are appearing at the heat flux of 900 W/cm<sup>2</sup> with flow rates of 200 and 300 g/min in the IR images.

As the flow rate increases, the allowable heat dissipation from the metal serpentine heater to the solid substrates to the working fluid also improves. In Figure 5.2b, both  $T_{\text{heat,max}}$  and  $T_{\text{heat,avg}}$  are reduced with the increased flow rate at a given heat flux. However, the localized hotspots starts appearing as the heat flux increases and these localized hotspots creates nonlinear behavior in  $T_{\text{heat,max}}$  and  $T_{\text{heat,avg}}$ .

In Figure 5.3, thermal images captured by the IR camera show temperature gradient across the heated surface, and they are compared with the captured thermal images from the CFD results. At the heat flux of  $300 \text{ W/cm}^2$  with the given flow rates (Figure 5.3a), the temperature distribution in the IR and CFD images shows similarity and it is quantified and plotted in Figure 5.2b. However, at the heat flux of  $900 \text{ W/cm}^2$  (Figure 5.3b), wider local hotspots show up in the IR images, compared to the CFD thermal images. In addition, the temperatures at these local hotspots are higher than the temperatures at the same locations in the CFD images, thus the  $T_{\text{heat,max}}$  data points are higher than the estimated  $T_{\text{heat,max}}$  lines in Figure 5.2b.

The nonlinearity issue in  $T_{\text{heat,max}}$  is mostly due to nonlinear heating effect in the metal serpentine heater. The detailed discussion on this topic is described in Appendix C.2. In principle, the resistance of the metal heater changes its local resistance if there is temperature gradient, and this phenomenon leads to nonuniform heat fluxes which are local hotspots. According to the study in Appendix C.2, the  $T_{\text{heat,max}}$  at the heat flux of  $1000 \text{ W/cm}^2$  with a heat transfer coefficient of  $100 \text{ kW/m}^2\text{-K}$  goes up by 3 – 3.5 %. If this effect is taken into account for estimating  $T_{\text{heat,max}}$  in the CFD simulations, the  $T_{\text{heat,max}}$  for  $1000 \text{ W/cm}^2$  heat flux with 300 and 400 g/min flow rates changes from 142.3 to 146.5 °C, and from 138.2 to 142.4 °C, respectively.

### **5.2.1.2 Thermal resistance and heat transfer coefficient**

The  $q_{\text{heat}}$  (or  $q$ ) and  $q_{\text{trans}}$  are calculated using measured applied electrical current and voltage to the serpentine heater, and the measured change in the sensible heat of the liquid. Although we confirmed that numerical simulation indicated only 2 – 3 % heat loss due to conduction at the periphery of the heated chip, the experimental heat loss,  $q_{\text{loss}}$ , ranged up to 19.7 % of  $q$  as the flow rate decreased. In addition,  $R_{\text{total,exp}}$  became larger

than  $R_{total,CFD}$  as  $(q_{loss}/q)$  increased,  $R_{total,CFD}$  values were out of the error bars of  $R_{total,exp}$  at the flow rate of 0.03 l/min (Figure 5.4a, 5.4b).

The inlet temperature of the fluid,  $T_{f,in}$ , is measured using a thermocouple, see Table 3.1. Figure 5-4a depicts the measured and simulation results for  $R_{total-max}$  (or  $R_{total-max,exp}$ ) vs. flow rate for the nominal heat flux value of  $250 \text{ W/cm}^2$ , which agree well for given uncertainty levels estimated in Appendix B.1. As expected, both  $R_{total-max}$  and  $R_{advection}$  decrease as the flow rate increases at a given heat flux. The sum of conduction and convection thermal resistances,  $R_{comp}$  ( $= R_{cond} + R_{conv}$ ), can be estimated by  $R_{comp} = R_{total-max} - R_{adv}$  and it also follows same changing trend as both  $R_{total-max}$  and  $R_{adv}$ .

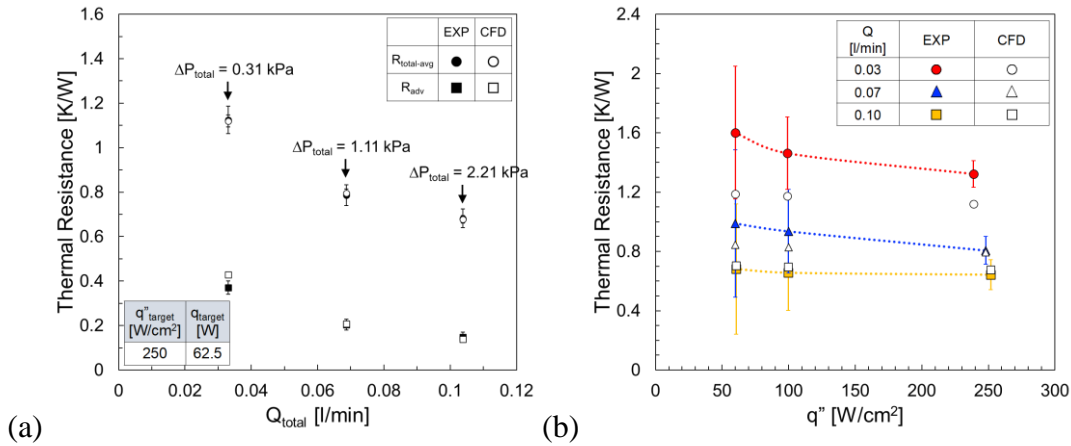


**Figure 5. 4** Experimental data and predictions for (a)  $R_{total}$  &  $R_{adv}$  vs. Flow Rate, and pressure drop for single-phase water at heat flux of  $250 \text{ W/cm}^2$ . (b) As expected, there is no significant change in  $R_{total}$  as the supplied heat flux increased from  $60$  to  $250 \text{ W/cm}^2$  for a given flow rate.

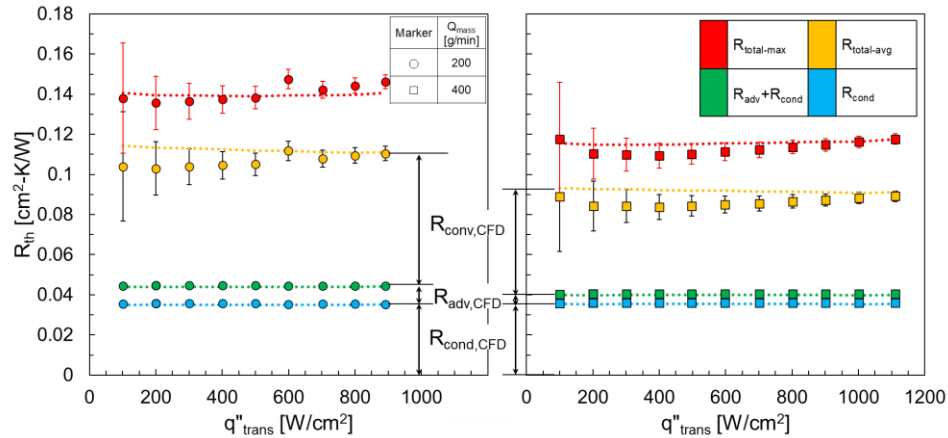
Figure 5.4b shows that there is no significant change in  $R_{total-max}$  as the supplied heat flux increased from  $60$  to  $250 \text{ W/cm}^2$  for a given flow rate. The error bar for  $R_{total-max}$  and  $R_{adv}$  decreases as the flow rate increases, despite of increase in the uncertainty ratio of  $R_{total-max}$  and  $R_{adv}$ , which is due to reduction in both  $R_{total-max}$  and  $R_{adv}$  along with the increase in flow rate, for details see Appendix B.1.

Figure 5.5 shows how each thermal resistance component is changing as the flow rate changes from  $200 \text{ g/min}$  to  $400 \text{ g/min}$ . In addition, we try to show the contribution of these thermal resistance components to the total thermal resistance. As expected,  $R_{adv}$  and  $R_{conv}$  decrease as the flow rate increases, but  $R_{cond}$  remains almost constant. Therefore,

reduction in  $R_{total-max}$ , and  $R_{total-avg}$  are attributed to the reduced  $R_{adv}$  and  $R_{conv}$ , mostly from  $R_{conv}$  (52 - 60 % of  $\Delta R_{total-avg}$ ), as the flow rate increases.

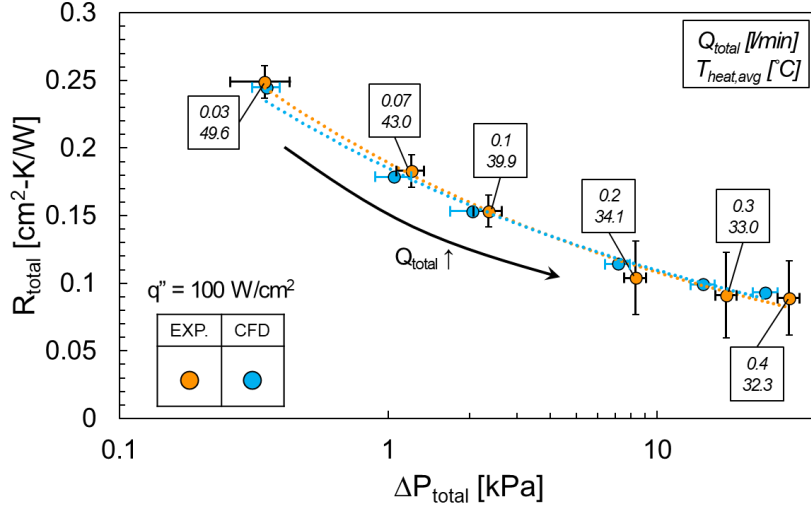
As the flow rate is doubled from 200 to 400 g/min,  $R_{total-max}$  and  $R_{total-avg}$  only reduces by 15 – 21 %. The reduction in  $R_{total}$  is mostly attributed to the reduction in  $R_{conv}$  with the increased flow rate. According to a newly developed correlation to predict average Nusselt number discussed in Section 5.2.1.5, the average Nusselt number of the microchannels in the EMMC is proportional to  $Re^{0.3623}$  and it is expected that the rate of growth in  $h_{effect}$  decreases with the higher flow rate. As a result, the rate of reduction in  $R_{conv}$  also decreases as well.

The uncertainty of  $R_{total-avg}$  (or  $R_{total-max}$ ) is attributed to uncertainties of  $q''_{trans}$ ,  $T_{heat,avg}$  (or  $T_{heat,max}$ ) and  $T_{f,in}$ , and it reduces with the increase heat flux which is discussed in Appendix B.1. The uncertainties of the both  $R_{total}$  start from 20 – 35 % at the heat flux of 100 W/cm<sup>2</sup> and decrease to 2 – 4 % at the heat fluxes of 900 – 1100 W/cm<sup>2</sup>.



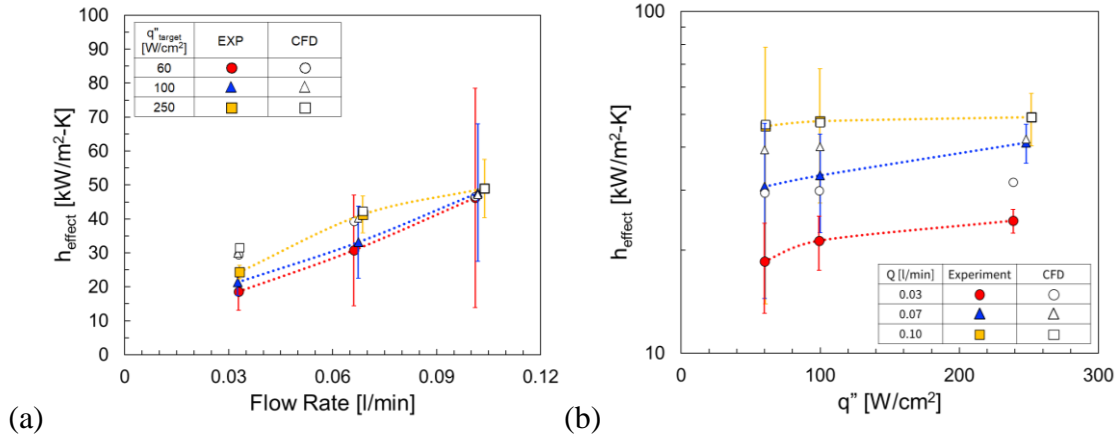
**Figure 5. 5** The change in thermal resistances plotted as a function of  $q''$ , reduction in  $R_{total}$  due to the increased flow rate is 15 - 21 %, despite the flow rate is doubled from 200 to 400 g/min. Dotted lines are thermal resistances from the CFD data.

In Figure 5.6,  $R_{total-avg}$  for six different flow rates are plotted as a function of  $\Delta P_{total}$  at a given heat flux of 100 W/cm<sup>2</sup>. As the flow rate increases from 0.03 to 0.4 l/min, the overall cooling performance of the EMMC is improved by 64 % but the EMMC sacrifices the overall system pressure drop by 8800 %. Lastly, we have proven that the experimental data and the CFD simulation results show good agreement over wide range of flow rates.

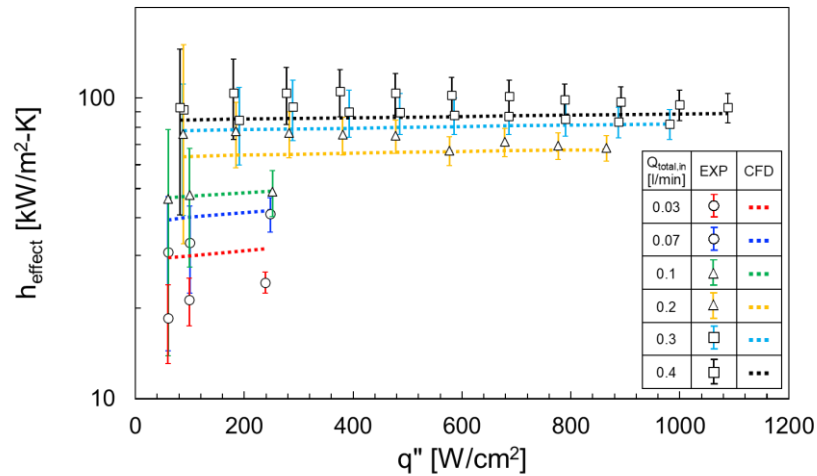


**Figure 5. 6** Summarized total thermal resistances as a function of total pressure drop at  $100 \text{ W/cm}^2$ . Six different flow rates, from 0.03 to 0.4 l/min, are used.

Figure 5.7a indicates that the heat transfer coefficient,  $h_{effect}$ , increases with flow rate. In single-phase regime,  $Re$  increases as the flow rate increases, and the thickness of thermal boundary layer is proportional to  $Re^{-\frac{1}{2}}$  [61]. Therefore,  $h_{effect}$  increases as the flow rate increases due to reduction in thickness of the thermal boundary layer. The heat transfer coefficient increases weakly with the applied heat flux due to slight increase in thermal conductivity of water, see Figure 5.7b. The discrepancy between the measured  $h_{effect}$  (or  $h_{effect,EXP}$ ) and CFD predictions ( $h_{effect,CFD}$ ), is within the range of estimated uncertainty except the flow rate was 0.03 l/min. According to Eqn. 5.5,  $h_{effect}$  is linearly proportional to  $q_{trans}$  and we have confirmed that  $q_{trans,EXP}$  became closer to  $q_{heat,EXP}$  as the flow rate increased. At the flow rate of 0.03 l/min,  $(q_{loss,EXP}/q_{heat,EXP})$  ranges from 14.9 to 19.7 %, however,  $(q_{loss,CFD}/q_{heat,CFD})$  is only 2 – 3 %. As a result,  $h_{effect,EXP}$  became smaller than  $h_{effect,CFD}$  at  $Q_{total,in} = 0.03 \text{ l/min}$  with a given  $q_{supply}$ . Especially, the discrepancy between  $h_{effect,EXP}$  and  $h_{effect,CFD}$  is maximized at the lowest flow rate and the heat flux,  $Q_{total,in} = 0.03 \text{ l/min}$ ,  $q_{supply} = 60 \text{ W/cm}^2$ , respectively, that is detailed in Appendix B.1.



**Figure 5. 7** The measured and simulated results for heat transfer coefficients at the cold-plate microchannel walls,  $h_{\text{effect}}$ . (a) The  $h_{\text{effect}}$  vs. flow rate for various heat fluxes, and (b) the  $h_{\text{effect}}$  vs. heat flux for various flow rates.



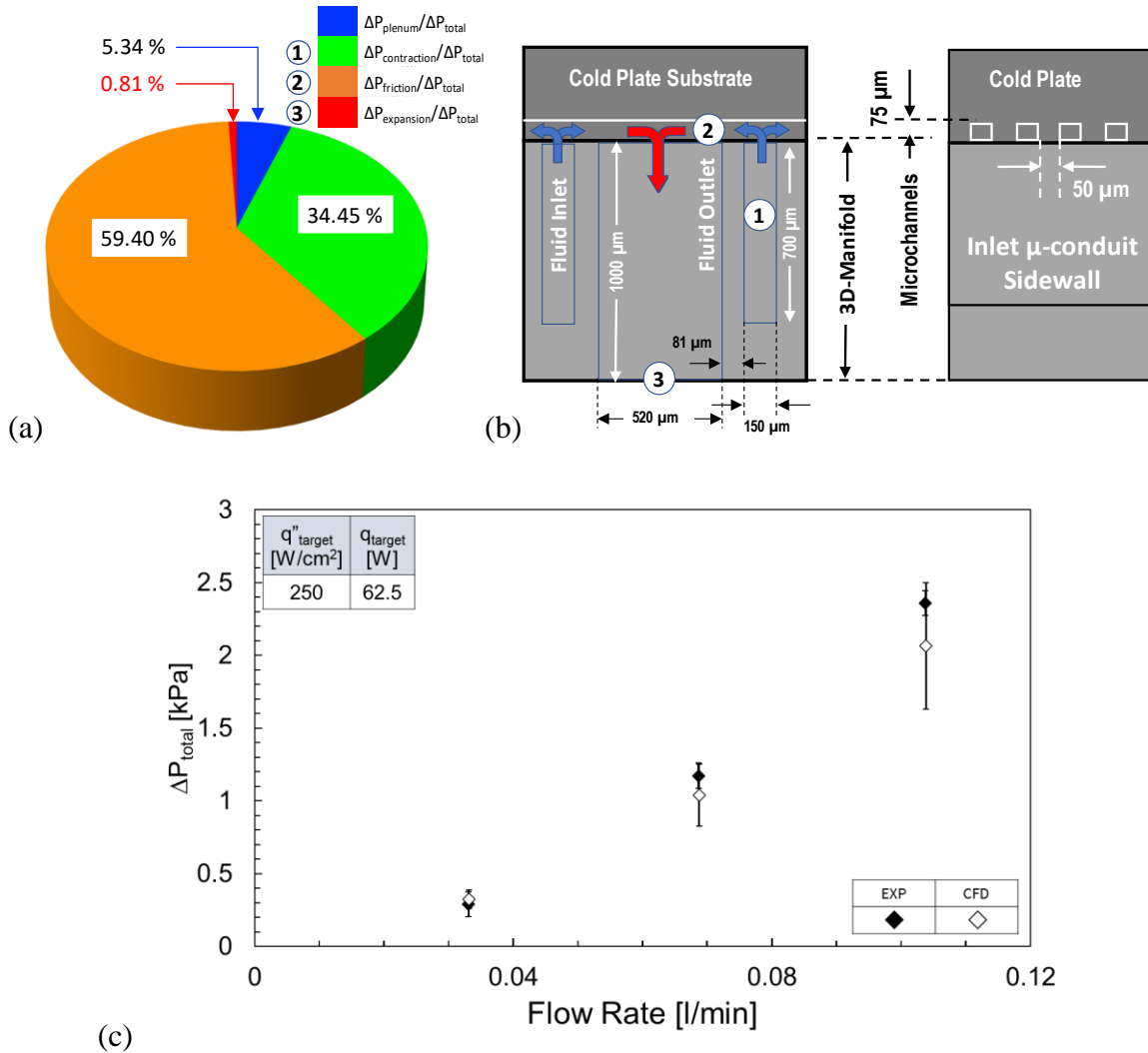
**Figure 5. 8** Summary of  $h_{\text{effect}}$  vs.  $q''$  for the flow rate from 0.03 to 0.4 l/min

Figure 5.8 summarizes all of the  $h_{\text{effect}}$  data with single-phase DI water as a function of the heat flux. Again, the  $h_{\text{effect}}$  increases with the higher flow rate, but the rate of growth in  $h_{\text{effect}}$  is reduced which follows the newly developed correlation in Section 5.2.1.5. In addition, the  $h_{\text{effect}}$  at a given flow rate minimally changes over the wide range of  $q''$  which will also be explained in Section 5.2.1.5. Therefore, based on the findings in Section 5.2.1.2, it is difficult to further improve the heat transfer coefficient by increasing flow rate of single-phase DI water higher than 400 g/min in the given EMMC geometry. The conclusion motivates our parametric study in different geometries of EMMCs in Section 4.2.

### 5.2.1.3 Hydraulic performance: pressure drop

The total pressure drop,  $\Delta P_{\text{total,EXP}}$ , across the  $\mu$ -cooler device is the only directly measured quantity. The contributions of various components are evaluated using CFD simulations, Figure 5.9a, and 5.9b. For the highest flow rate of  $Q_{\text{total,in}} = 100 \text{ g/min}$ , 34% and 5% of the total pressure drops occurs at the entrance (contraction) and exit (expansion) of microchannel to the 3D manifold conduits, respectively. Figure 5.9c compares the experimental data and simulation results for pressure drop vs. flow rate, which is proportional to square of mass flux,  $G^2$ . The difference between  $\Delta P_{\text{total,CFD}}$  and  $\Delta P_{\text{total,EXP}}$ , is significantly larger than the uncertainty of the differential pressure transducer ( $\pm 0.086 \text{ kPa}$ , see Table 3.1) for flow rates higher than  $0.066 \text{ l/min}$  (Figure 5.9c). This is due to difference between microchannel “target” design dimensions (used in numerical simulation) and that of “actual” microfabricated structure, details are discussed in Section 2.1. Lastly, there had been large variation in the inlet pressure as the flow rate changed. However, thermophysical property changes due to the pressure difference can be negligible compared to those by temperature changes since it is subcooled region.

For the higher flow rates from  $200 \text{ g/min}$  to  $400 \text{ g/min}$ ,  $\Delta P_{\text{total}}$  is also proportional to square of mass flux in Figure 5.10a. Discrepancy between  $\Delta P_{\text{total,EXP}}$  and  $\Delta P_{\text{total,CFD}}$  is covered by the uncertainty of  $\Delta P_{\text{total}}$  originated from the dimensional error during the fabrication. In Figure 5.10b,  $\Delta P_{\text{minor,CFD}}$ , the sum of  $\Delta P_{1,\text{CFD}}$  and  $\Delta P_{4,\text{CFD}}$ , also contributes 5 – 6 % of the  $\Delta P_{\text{total,CFD}}$ . However, the contribution of  $\Delta P_{2,\text{CFD}}$  and that of  $\Delta P_{3,\text{CFD}}$  to  $\Delta P_{\text{total,CFD}}$  are reversed (Figure 5.10b), 55 % and 39 %, respectively. In Section 5.2.1.4, we report that the Reynolds number and the fluid velocity at the Zone 2 (Figure 4.3, Figure 5.11a) are proportional to the flow rate.  $\Delta P_2$  in the converging section of the EMMC is proportional to square of the fluid velocity (Appendix B.3, Eqn. B.12), therefore, the contribution of  $\Delta P_2$  to  $\Delta P_{\text{total}}$  increases with the higher flow rates.



**Figure 5. 9** Results of the CFD simulations for pressure loss in the channel and 3D manifold: (a) relative contributions of pressure drop components:  $\Delta P_{\text{plenum}}$  (or  $\Delta P_1$ ),  $\Delta P_{\text{contraction}}$  (or  $\Delta P_2$ ),  $\Delta P_{\text{friction}}$  (or  $\Delta P_3$ ), and  $\Delta P_{\text{expansion}}$  (or  $\Delta P_4$ ) over the total pressure drop at  $Q_{\text{total,in}} = 100 \text{ g/min}$ , (b) schematics of the inlet, microchannel and outlet of the  $\mu$ -cooler, (c) experimental and numerical simulation results for  $\Delta P_{\text{total}}$  vs. Flow Rate at a nominal heat flux of  $q'' = 250 \text{ W/cm}^2$ .

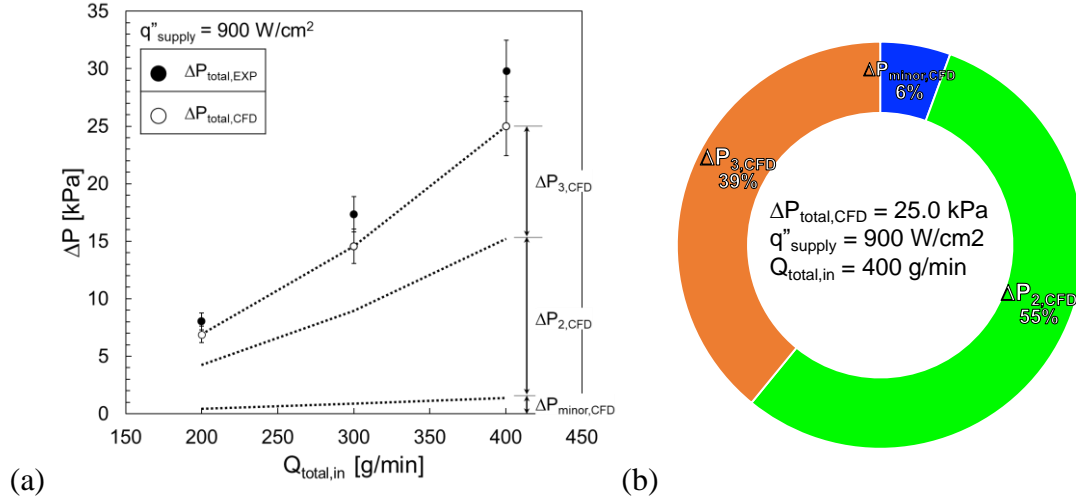


**Figure 5.10** (a)  $\Delta P_{total}$  vs.  $Q_{total,in}$  at a heat flux of  $900 \text{ W/cm}^2$ ,  $\Delta P_{total,EXP}$  is compared to  $\Delta P_{total,CFD}$  and agrees well with the estimation within the uncertainty, (b) composition of  $\Delta P_2$  and  $\Delta P_3$  to  $\Delta P_{total}$  is estimated by CFD simulations. Based on the simulation results, about 55 % of pressure drop occurs in the gradual contraction region, and microchannels under the hotspot is responsible for  $\sim 40 \%$  of  $\Delta P_{total}$ .

#### 5.2.1.4 Prediction of friction factor

Since the internal fluid flow with single-phase DI water cannot be empirically inspected due to limited visual access in the tested EMMCs, the conjugate CFD simulation results are used to develop a correlation to estimate Darcy friction factor based on the microchannels' Reynolds number.

Since the 5 mm-long microchannels are segmented by 4 manifold inlet conduits, there are 8 shortened flow paths per a microchannel, refer Figure 5.10. In other words, the distance between the middle line of Inlet 1 and that of Outlet 2 is the shortened flow path thanks to the manifold conduits. Therefore, the unit length of the fluid flow path in a microchannel,  $L_{unit}$ , is assumed to be  $625 \mu\text{m}$  for the further analysis. The hydraulic diameter of the microchannel,  $D_h$ , is  $100 \mu\text{m}$ .

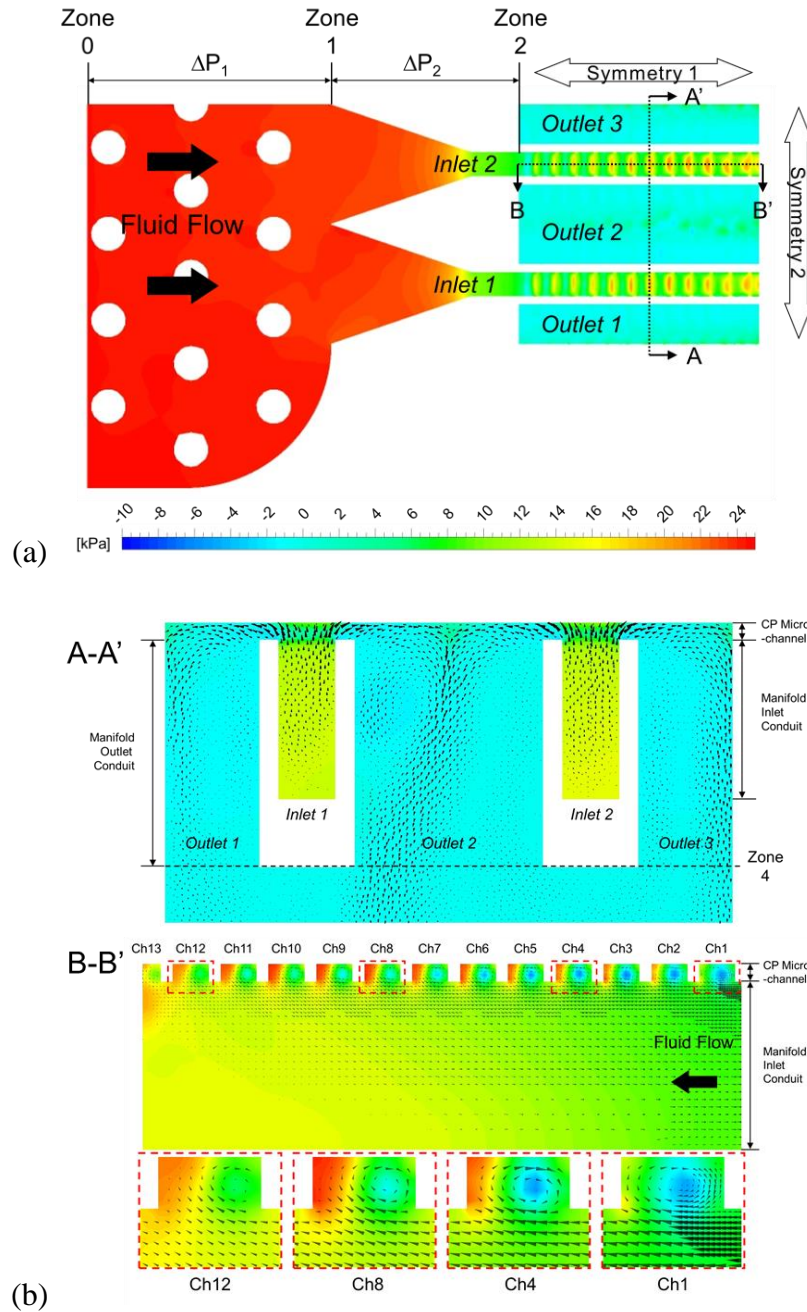


**Figure 5. 11** (a) Visualized pressure gradient in a quarter-cut EMMC CFD domain, showing inlet plenum, two converging sections, and inlet/outlet conduits, (b) visualized internal fluid flow pattern with arrow head vectors; A-A': at the interface between inlet/outlet conduits and a microchannel, the fluid is diverged and flows through the microchannel, and exits through the adjacent outlet conduit, B-B': after the fluid passes Zone 2, the fluid keeps diverging whenever it encounters adjacent CP microchannel, from Ch1 through Ch13. Ch 13 is the channel located at the very center of the EMMC, thus no further fluid flow is allowed after this point.

First, we have investigated individual microchannel's Reynolds number,  $Re$ , and other relevant thermo-fluidic properties such as fluid velocity, density, and pressure drop across the shortened microchannels. After then, manually calculate Darcy friction factor,  $f_{CFD}$ , in each microchannel by Eqn. 5.9 and 5.10:

$$f_{CFD} = \frac{\left(\frac{\Delta P_{unit}}{L_{unit}}\right) \cdot D_h}{\frac{1}{2} \cdot \rho \cdot \bar{v}^2} \quad (5.9)$$

$$Re_{CFD} = \frac{\rho \cdot D_h \cdot \bar{v}}{\mu} \quad (5.10)$$

where  $\Delta P_{unit}$  is the pressure difference across the unit flow path,  $L_{unit}$ , and  $\bar{v}$ ,  $\rho$ ,  $\mu$  are average fluid velocity, density and dynamic viscosity in the microchannels, respectively.

**Table 5. 1** Previous friction factor correlations for rectangular ducts

Authors	Equation	Remarks
Shah, London (1978) [57]	$f \cdot Re = 96 \left[ 1 - \frac{1.3553}{\alpha} + \frac{1.9467}{\alpha^2} - \frac{1.7012}{\alpha^3} + \frac{0.9564}{\alpha^4} - \frac{0.2537}{\alpha^5} \right]$	Fully developed laminar flow
	$f_{app} \cdot Re = \left[ \left\{ \frac{3.2}{(x^+)^{0.57}} \right\}^2 + (f \cdot Re)_{fd}^2 \right]^{\frac{1}{2}}$ , $x^+ = L/(D_h \cdot Re)$	Apparent friction factor for both the developing and fully developed laminar flow
Nakamura, et al. (1979) [59], Harms, et al. (1999) [58]	$f_{app} Re = \left(\frac{\mu_w}{\mu_m}\right)^{0.58} \cdot \frac{16}{G} + \frac{K_\infty}{4x^+}$ , $f_{app} Re = 4 \cdot (11.3(x^+)^{-0.202} \alpha^{-0.094})$ , $f_{app} Re = 4 \cdot (5.26(x^+)^{-0.434} \alpha^{-0.010})$ ,	$x^+ \geq 0.1$ $0.02 \leq x^+ < 0.1$ $0.001 < x^+ \leq 0.02$
Jung (2020)	$f_{app} Re = 22.35(x^+)^{-0.380} \alpha^{-0.094}$ , $f_{app} Re = 1.33(x^+)^{-1.112} \alpha^{-0.010}$ ,	$0.02 \leq x^+ < 0.1$ $0.001 < x^+ \leq 0.02$
		A correction for temperature-dependent viscosity in rectangular ducts of various aspect ratios  A newly developed correlation for the given EMMC structure

In Figure 5.11a, we present the average fluid velocity and  $Re$  profiles for three different flow rates, 200 – 400 g/min, at a given heat flux of 800 W/cm<sup>2</sup>. All the data points are configured from the CFD simulation results for single-phase DI water with the flow rates of 200 – 400 g/min. Note that the maximum velocity and  $Re$  values are recognized at the Zone 2, where the fluid is about to enter the heated region. The normalized average fluid velocity in each microchannel is also plotted in Figure 5.11b

and it gradually increases as the flow proceeds toward the Symmetry Surface 2 (Figure 5.10a). Thus, the mass flux in each microchannel is not same due to nonuniform distribution of the fluid.

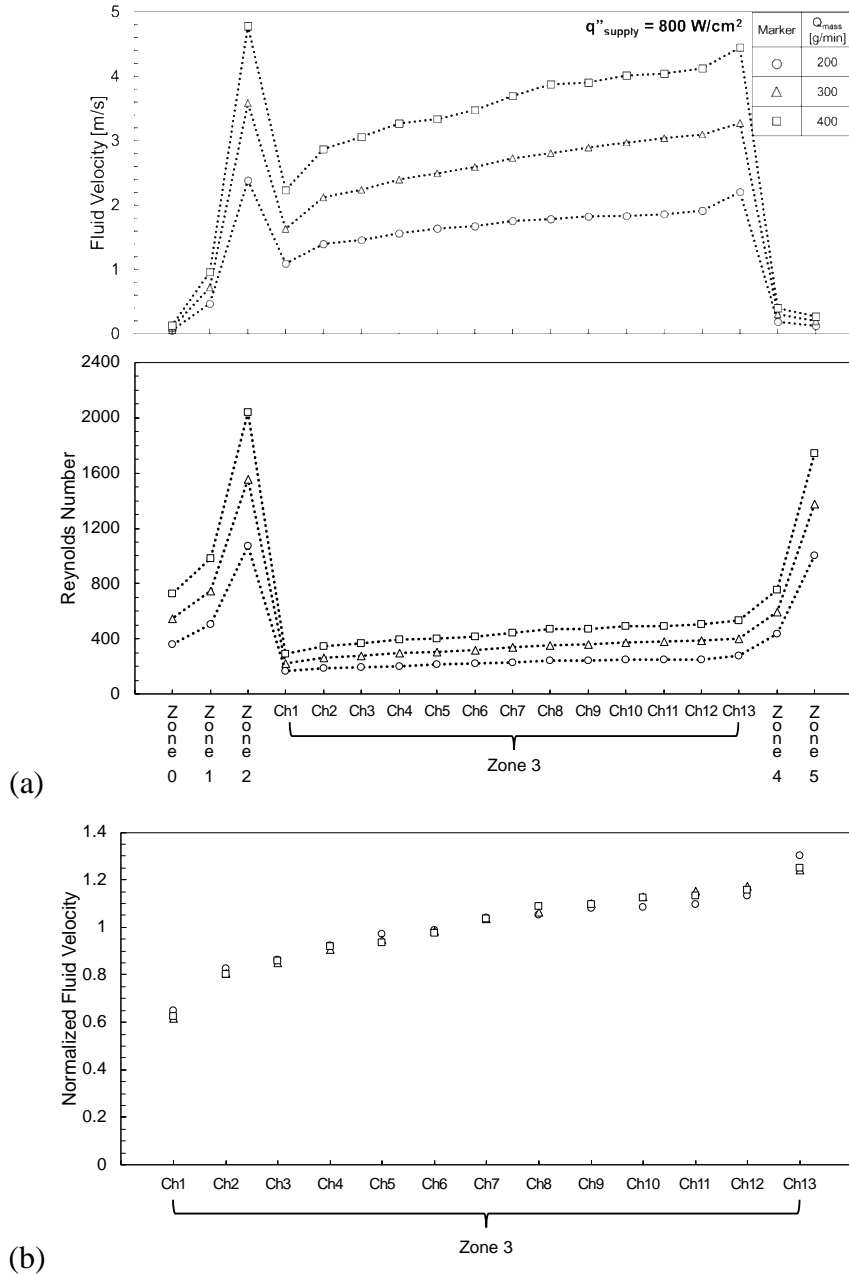


**Figure 5. 12** (a) Average velocity and Reynolds number profiles in every defined zone in the CFD domains, (b) normalized velocity profile in each channel in Zone 3.

The configured friction factors,  $f_{\text{CFD}}$ , and  $Re$  are compared to the conventional predictions given in Table 5.1 [57-59]. Figure 5.12 shows four plots showing friction factors as a function of  $Re$  for the heat fluxes from 100 to 1000  $\text{W}/\text{cm}^2$ .

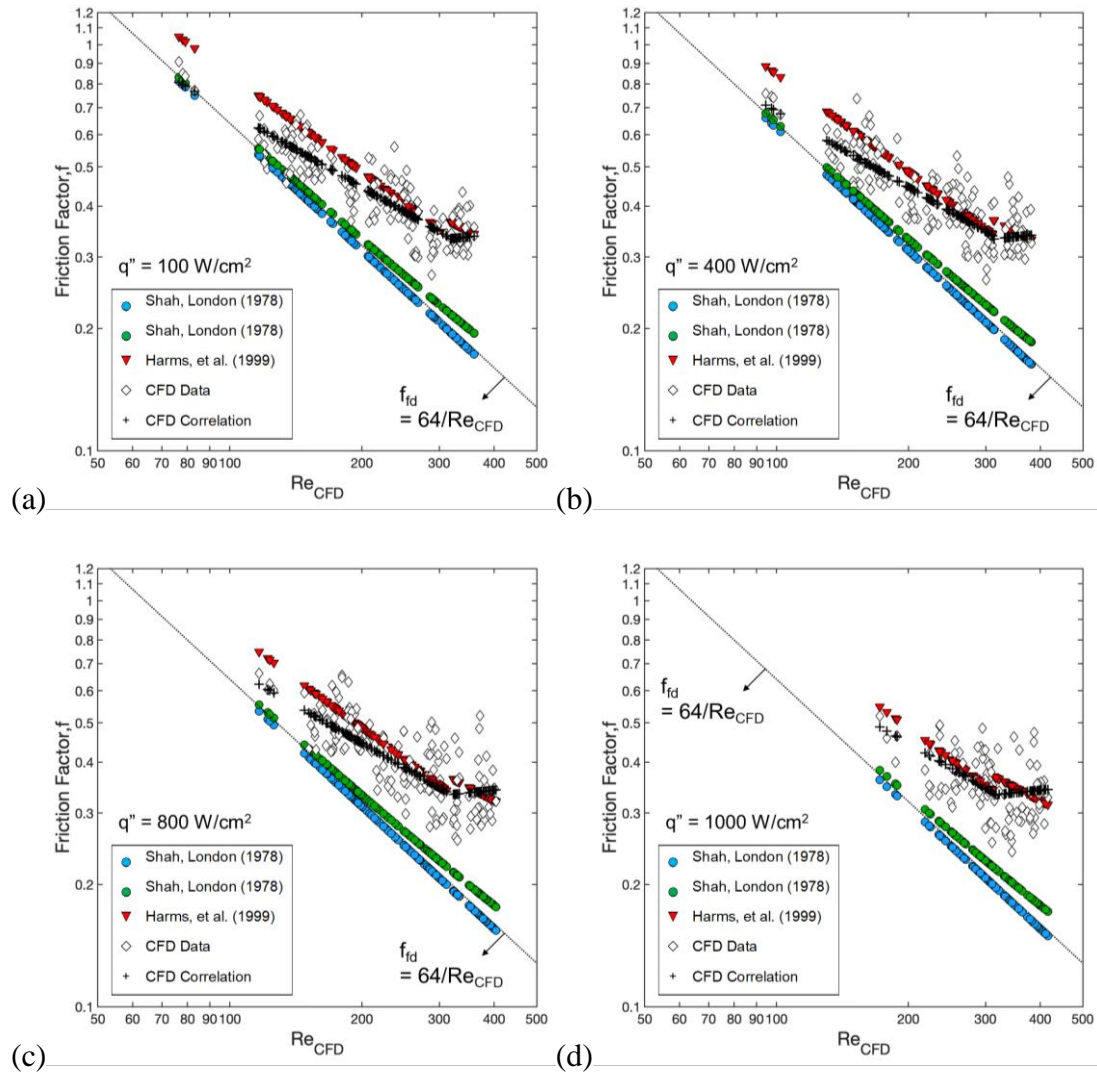


**Figure 5.13** Friction factor vs.  $Re_{CFD}$  in various heat fluxes for the comparison purpose. For the developing flow, hydrodynamic entrance length is considered in the correlations [58, 59].

The  $f_{CFD}$  values are always higher than the predicted  $f$  values for fully developed laminar flow, as expected. The apparent friction factor from Shah and London [57] also cannot capture the changing trend of the  $f_{CFD}$  as a function of  $Re$ . Unlike the correlations from Shah and London [57], however, the correlation from Nakamura, et al [59] captures the changing trend of the  $f_{CFD}$  with a good fidelity in Figure 5.12. Subsequently, we checked hydrodynamic entrance length from the current CFD simulation results and plotted Poiseuille number as a function of the entrance length. The resulting graph is given in Figure 5.13.

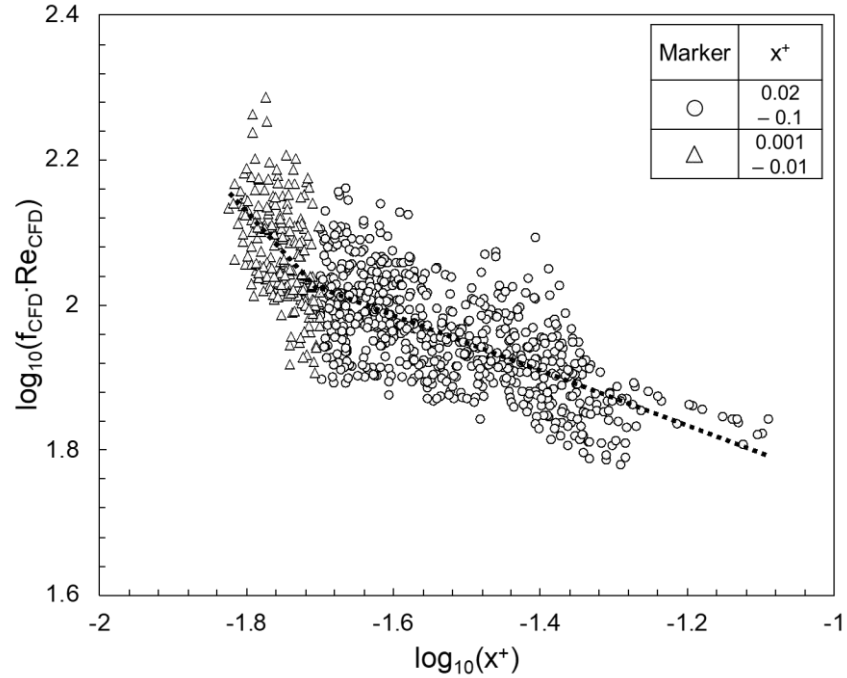


**Figure 5. 14** Poiseuille number vs. hydrodynamic entrance length plotted in log-log scale. The entrance length,  $x^+ = \frac{L_{unit}}{Re \cdot D_h}$ , is calculated in each segmented microchannel,  $f_{CFD}$  and  $Re_{CFD}$  are given from the CFD simulation results.

The change in the slope of the Poiseuille number is recognized before and after  $x^+ = 0.02$ . If we use the same correlation format from Nakamura, et al [59], a new correlation is added to Table 5.1 (the last row). In order to check the fidelity of the newly developed correlation, the friction factors predicted by the correlations in Table 5.1 are compared to the  $f_{CFD}$  for four different heat flux cases (Figure 5.14). The most of the predicted friction factors by Shah and London [57] are falling within  $\pm (30 - 50) \%$  error bands, but the predicted friction factors by Nakamura, et al. [59] and the new correlation are falling within  $\pm (10 - 30) \%$  error bands. Moreover, the newly developed correlation predicts most of the friction factors within  $\pm 10 \%$  error bands for the tested EMMC.

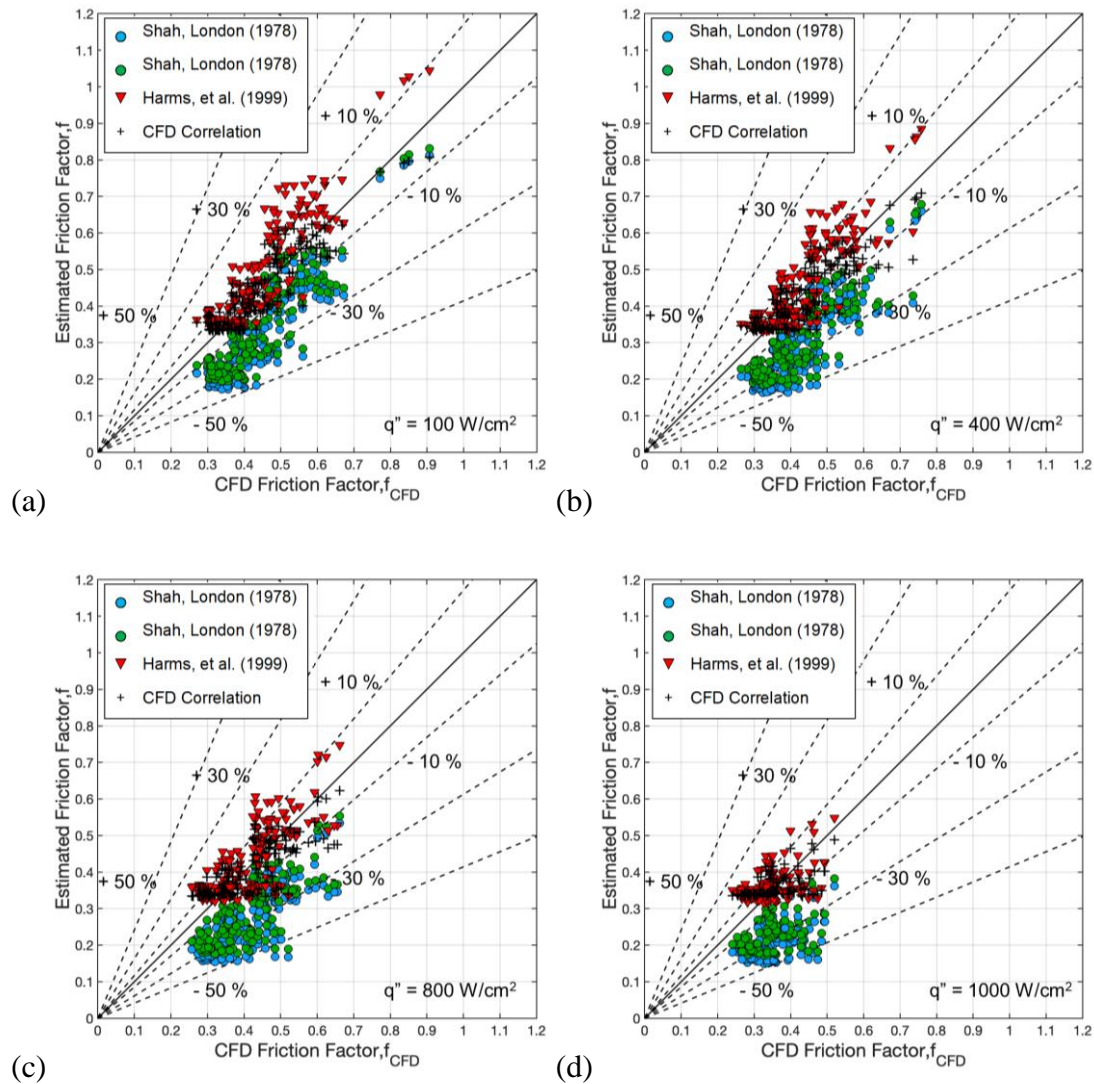


**Figure 5.15** Friction factors predicted by the existing correlations and a newly developed correlation vs.  $f_{CFD}$  for four different heat flux cases.

Again, the predicted  $\Delta P_{3,new}$  is a strong function of  $Re$  for wide range of the heat fluxes (from 100 to 1000  $W/cm^2$ ) and flow rates (from 200 to 400  $g/min$ ), the predicted  $\Delta P_{3,new}$  values are falling within  $\pm (10 - 30) \%$  error bands (Figure 5.15a).

Since the correlation only predicts the  $\Delta P_3$  in the microchannels of the given EMMC, the direct comparison between  $\Delta P_{3,EXP}$  and  $\Delta P_{3,new}$  cannot be done in this work. Instead,  $\Delta P_{total,EXP}$  is compared to  $\Delta P_{total,CFD}$  at heat fluxes of 200/400/800  $W/cm^2$  in Figure 5.15b. If the uncertainty bars are considered, the  $\Delta P_{total,EXP}$  falls within  $\pm 10 \%$  error bands of

the  $\Delta P_{\text{total,CFD}}$ , therefore, there is a great potential for us to apply the developed correlation to predict empirical friction factors in the given EMMC.

To complete the discussion of the friction factor correlation, we should admit the fact that the current correlation may be valid only for the current EMMC geometry. Therefore, more test cases with different geometries are required to complete the prediction model for the friction factors.

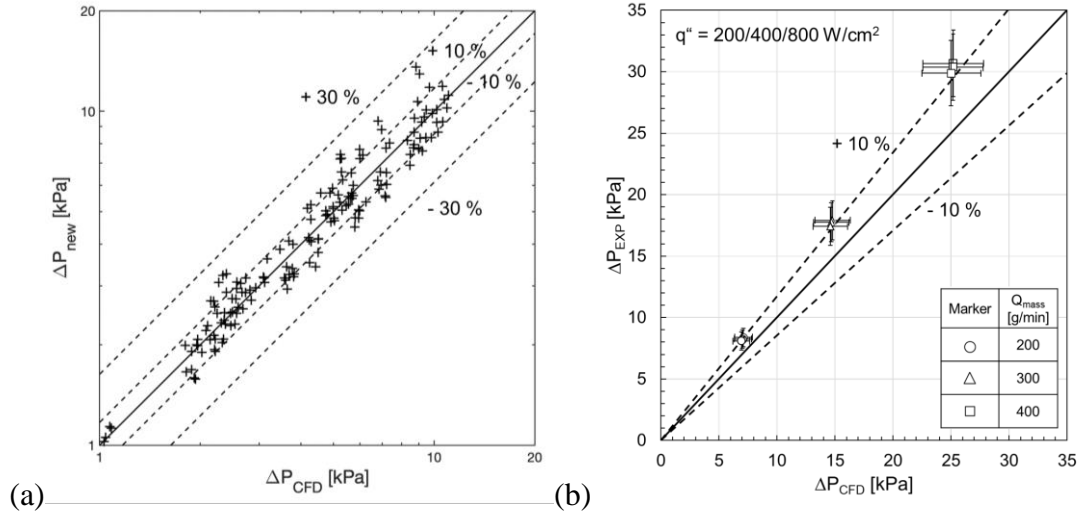


**Figure 5. 16** (a) Predicted  $\Delta P_{\text{total}}$  by the new correlation plotted as a function of  $\text{Re}_{\text{CFD}}$  and a function of  $\Delta P_{\text{total,CFD}}$  for heat fluxes of  $800 \text{ W/cm}^2$ , (b) comparison between  $\Delta P_{\text{total,EXP}}$  and  $\Delta P_{\text{total,CFD}}$  at the heat fluxes of  $200/400/800 \text{ W/cm}^2$

### 5.2.1.5 Prediction of Nusselt number in CP microchannels

The CFD simulation results with single-phase DI water are used again to develop a correlation to predict average Nusselt number in the microchannels. The average Nusselt number from the CFD simulation,  $\text{Nu}_{\text{avg,CFD}}$ , is expressed as:

$$\text{Nu}_{\text{avg,CFD}} = \frac{h_{\text{effect}} \cdot D_h}{k_f} \quad (5.10)$$

where  $h_{\text{effect}}$  is the effective heat transfer coefficient calculated by Eqn. 5.5 and 5.6,  $k_f$  is the fluid thermal conductivity at the reference fluid temperature,  $T_{f,\text{ref}}$ . The next step is to estimate average Nusselt numbers by the conventional correlations for the rectangular ducts (or channels), listed in Table 5.2. The correlations from Ref. [57], [60] predict local

Nusselt numbers as a function of dimensionless axial distance for the thermal entrance region,  $x^*$  (Figure 5.17a). The correlation from Ref. [Nusselt2] is the expression for average Nusselt numbers.

**Table 5. 2** Previous Nusselt number correlations for rectangular ducts

Authors	Equation	Remarks
Shah, London (1978) [57]	$\begin{aligned} \text{Nu}_{x^*} &= 5.39 \text{ for } x^* \geq 0.1 \\ \text{Nu}_{x^*} &= 5.16 + 0.02(x^*)^{-1.035} \\ &\quad \text{for } 0.01 \leq x^* < 0.1 \\ \text{Nu}_{x^*} &= 1.17(x^*)^{-0.401} \text{Pr}^{-0.044} \\ &\quad \text{for } 0.001 < x^* < 0.01 \\ &\quad x^* = x/(D_h \cdot \text{Re} \cdot \text{Pr}) \end{aligned}$	Single rectangular channel, laminar flow, local Nusselt number
	$\begin{aligned} \text{Nu}_{x^*} &= \left[ \begin{array}{l} 8.24 - 16.8 \cdot \alpha + 25.4 \cdot \alpha^2 \\ -20.4 \cdot \alpha^3 + 8.70 \cdot \alpha^4 \end{array} \right] \\ &\quad \text{for } x^* \geq 0.1 \\ \text{Nu}_{x^*} &= 3.35(x^*)^{-0.130} \alpha^{-0.120} \text{Pr}^{-0.038} \\ &\quad \text{for } 0.013 \leq x^* < 0.1 \\ \text{Nu}_{x^*} &= 1.87(x^*)^{-0.300} \alpha^{-0.056} \text{Pr}^{-0.036} \\ &\quad \text{for } 0.005 < x^* < 0.013 \end{aligned}$	Multiple rectangular channels, laminar flow, local Nusselt number
Grigull & Tratz (1965) [60]	$\text{Nu}_{x^*} = 4.36 + \frac{0.00668 \cdot \frac{D_h}{x} \cdot \text{Re} \cdot \text{Pr}}{1 + 0.04 \left[ \frac{D_h}{x} \cdot \text{Re} \cdot \text{Pr} \right]^{\frac{2}{3}}}$	Numerically investigated correlation for the thermal entrance problem, laminar flow with constant heat flux cases
Kraus, Bejan (2003) [61]	$\begin{aligned} \bar{\text{Nu}} &= 1.86 \left( \frac{D_h}{L} \cdot \text{Re} \cdot \text{Pr} \right)^{1/3} \cdot \left( \frac{\mu_b}{\mu_w} \right)^{0.14} \\ &\quad \text{for } \frac{D_h}{L} \cdot \text{Re} \cdot \text{Pr} > 10, 0.0044 \leq \left( \frac{\mu_b}{\mu_w} \right) < -9.75, \\ &\quad 0.48 \leq \text{Pr} \leq 16700 \end{aligned}$	Thermally and hydrodynamically developing flow, average Nusselt number for constant surface temperature condition. $\mu_b$ : the viscosity at the mean bulk temperature, $\mu_w$ : the viscosity at the wall temperature
Jung (2020)	$\bar{\text{Nu}} = 0.9961 \cdot \text{Re}^{0.3623} \cdot \text{Pr}^{\frac{1}{3}}$	A newly developed correlation for the given EMMC structure, average Nusselt number

With the expressions in Ref. [57], [60], local heat transfer coefficients are estimated from the local Nusselt numbers. The average heat transfer coefficients are deduced from the local heat transfer coefficients by length-weighted averaging method afterward. Figure 5.17b shows one exemplary plot showing mean Nusselt numbers predicted by the correlations in Table 5.2 against the average Nusselt number from one of the CFD simulation cases. The tasks done in Figure 5.17 are repeated for all CFD simulation cases with single-phase DI water and the results are presented in Figure 5.18.

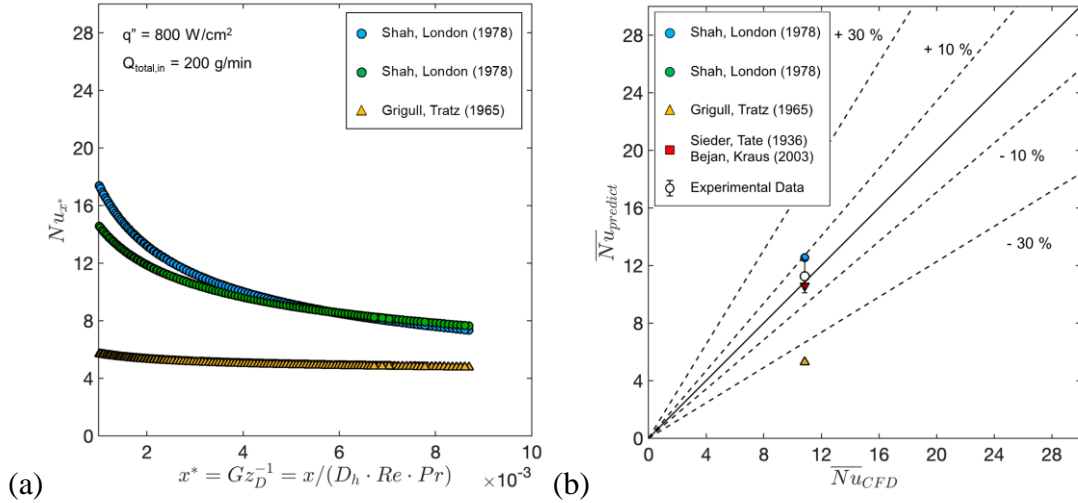


**Figure 5.17** (a) Local Nusselt number vs. dimensionless axial distance for the thermal entrance region,  $x^*$ , (b) predicted average Nusselt numbers against the average Nusselt number from the CFD simulation. Figure only shows one CFD simulation case,  $q'' = 800 \text{ W/cm}^2$ ,  $Q_{\text{total,in}} = 200 \text{ g/min}$ .

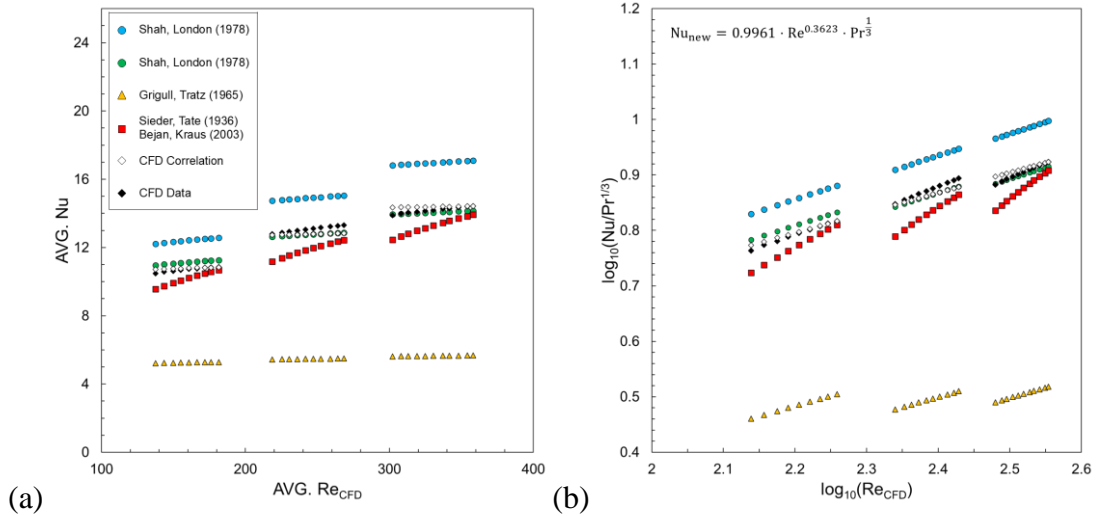


**Figure 5.18** (a) Mean Nu vs.  $Re_{\text{CFD}}$ , the predicted mean Nu from the existing correlations are compared with average Nu from the CFD simulations, (b) Mean  $\text{Nu}/\text{Pr}^{1/3}$  vs.  $Re_{\text{CFD}}$  in log-log scale

In Figure 5.18, the predicted mean Nu from Ref. [57], [61] shows a good agreement with the average Nu from the CFD simulations. However, the correlation from Ref. [57] and [60] over and underpredicts the mean Nu possibly because the correlations are not designed for multi-channel configuration. A microchannel with a hydraulic diameter of

600  $\mu\text{m}$  was tested by Shilder, et al. [63] and they reported that the measurements agreed well with the correlation from Ref. [60]. We also propose a new correlation to predict average Nu for the test structure, and the resulting values are plotted in Figure 5.18 and Figure 5.19.

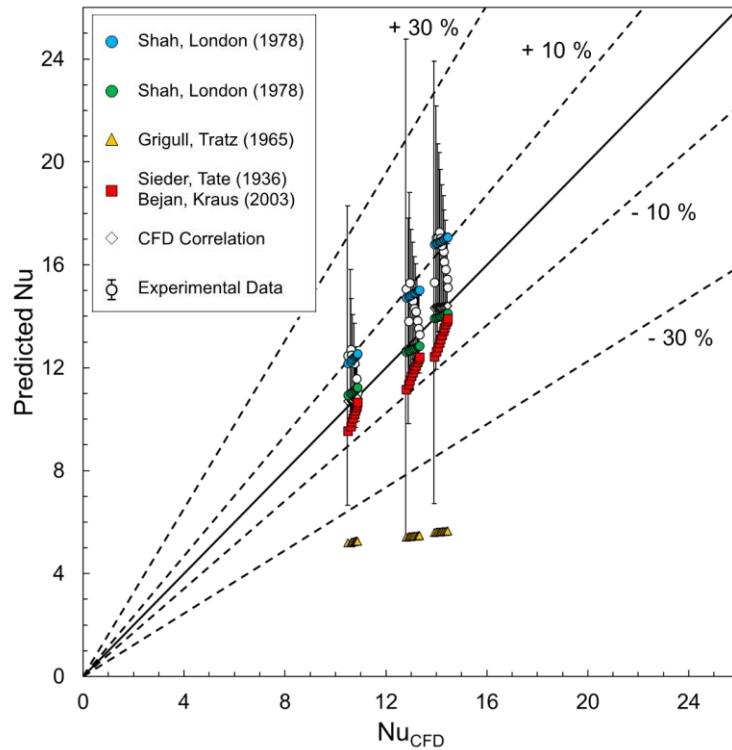


**Figure 5. 19** Summary of the predicted Nu and measured Nu vs.  $Nu_{CFD}$  for all test cases with single-phase DI water.

In Figure 5.19, the predicted Nu from Ref. [57], [58] and the experimentally measured Nu fall within  $\pm 10 - 30\%$  error bands. The new correlation shows highest fidelity in predicting average Nu in Figure 5.19, but we have to be careful to utilize the proposed correlation for different geometries and thermofluidic conditions. The correlation proposed in this section is designed for thermally and hydrodynamically developing laminar flow and more test cases with different geometries are needed to complete the prediction model for EMMCs.

## 5.2.2 Single-phase R-245fa

### 5.2.2.1 Temperature Behavior

Figure 5.20 describes the behavior of average heated surface temperature as the flow rate and the supplied heat are changed. The average surface temperatures,  $T_{\text{heat,avg}}$ , vs. total pressure drops,  $\Delta P_{\text{total}}$ , for supplied heat fluxes,  $q_{\text{heat}}$ , from 25 to 300 W/cm<sup>2</sup> are depicted in Figure 5.20a. As expected, the average temperature increases with the increased  $q_{\text{heat}}$ , and decreases with the increased flow rates. In addition, the onset of nucleate boiling (ONB) is delayed as the flow rate increases.

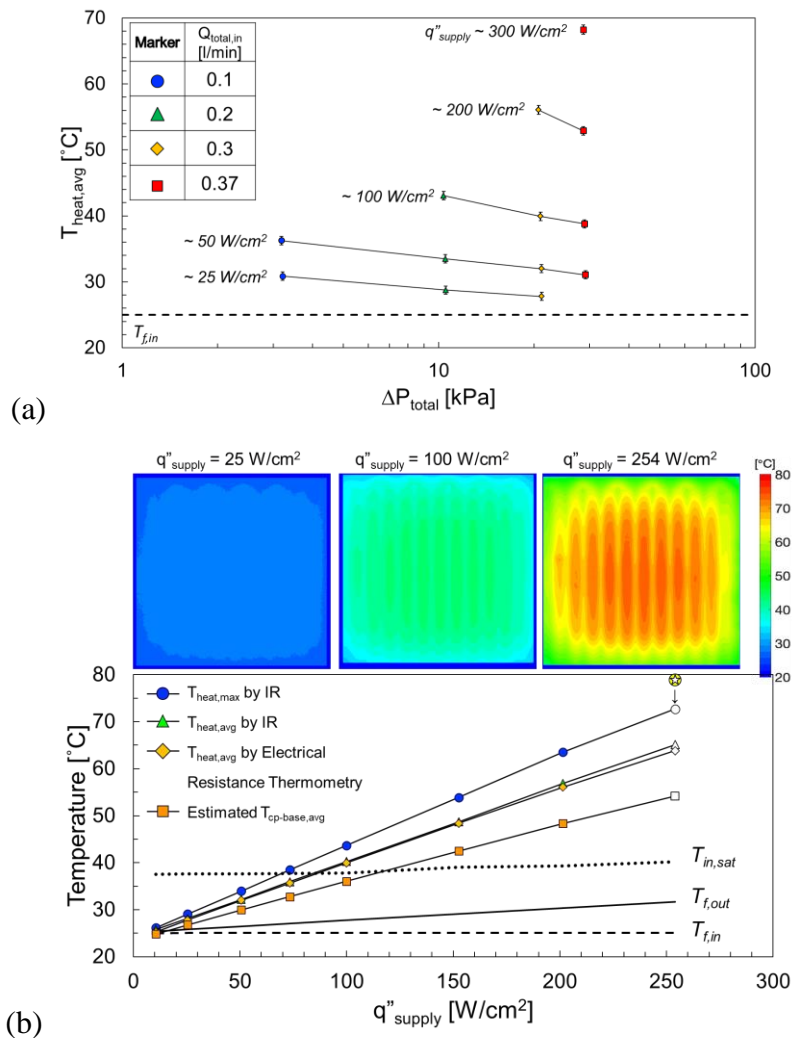


**Figure 5. 20** Experimental results, (a)  $T_{\text{heat,avg}}$  vs.  $\Delta P_{\text{total}}$ , the supplied heat and the fluid flow rate are up to 300 W/cm<sup>2</sup> and 0.37 l/min, respectively, (b) measured temperatures vs. supplied heat flux at a given flow rate of 0.3 l/min, open marker represents the ONB or two-phase regime (see Appendix B.2 for details)

Figure 5.20b depicts the measured  $T_{\text{heat,max}}$ ,  $T_{\text{heat,avg}}$ ,  $T_{\text{f,out}}$  at a constant flow rate of 0.3 l/min, and they all increase linearly with the increase heat flux as expected for single-phase flow. The measured average temperature of the heater using IR and electrical resistance thermometry method agree well with each other.

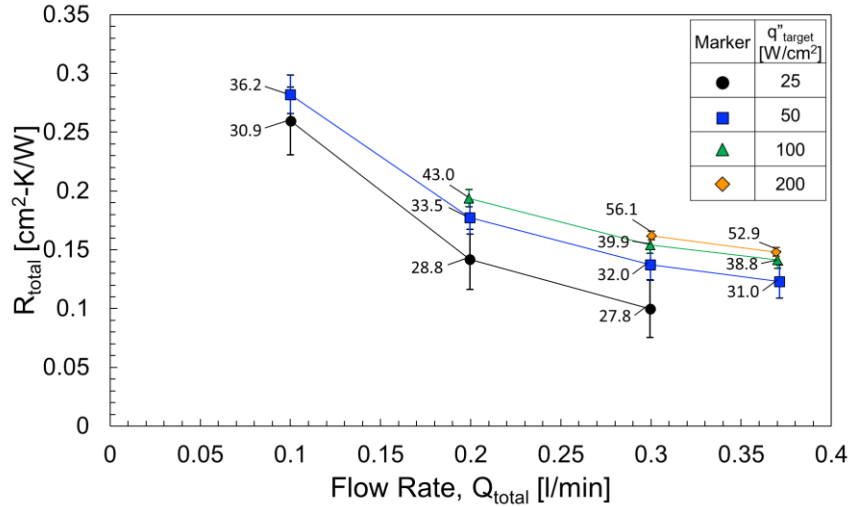
The inlet pressure is changing as the flow rate increases from 0.1 to 0.37 l/min, therefore, the saturated fluid temperature at the outlet (see Table 5.3) also increases due to a combination of the total pressure drop and the inlet pressure shift. In Appendix B.2, we take the pressure shift into account for the analytic estimation of the ONB points.

**Table 5. 3** Gradual increase in the saturated fluid outlet temperature

Flow Rate [l/min]	Range of $P_{\text{in}}$ [kPa]	Range of $P_{\text{out}}$ [kPa]	Saturated Fluid Outlet Temperature [ $^{\circ}\text{C}$ ]
0.1	219 – 224	216 – 221	35.9 – 36.6
0.2	235 – 241	225 – 230	38.1 – 38.7
0.3	254 – 267	233 – 247	40.4 – 41.9
0.37	332 – 358	303 – 329	48.8 – 51.2

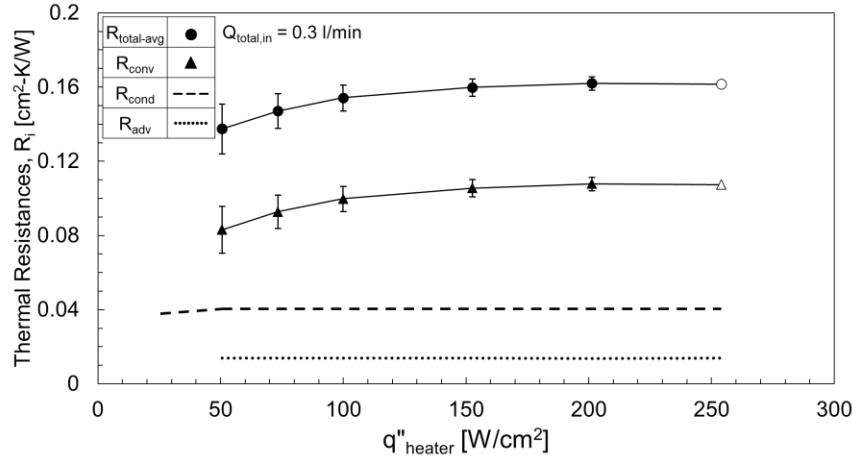
### 5.2.2.2 Thermal resistance and heat transfer coefficient

Figure 5.21 shows that for a given heat flux, the total thermal resistance,  $R_{\text{total}}$ , decreases with the increased flow rate. More specifically, both the convection and advection thermal resistances,  $R_{\text{conv}}$ ,  $R_{\text{adv}}$ , are decreasing because of the reduced microchannel base temperature,  $T_{\text{cp,base,avg}}$ , and the reduced fluid temperature,  $T_{\text{f,ref}}$ , respectively (Eqn. 5.4). At higher flow rate, the rate of reduction in the total resistance  $R_{\text{total}}$  decreases since the  $R_{\text{conv}} \sim \text{Re}^{-1/2}$ , and as we approach the conduction resistance limit of  $R_{\text{cond}} \sim 0.04 \text{ cm}^2\text{-K/W}$  (due to 400  $\mu\text{m}$  thick silicon substrate). Therefore, further reduction in  $R_{\text{total}}$  by increasing the flow rate higher than 0.37 l/min should not be expected.



**Figure 5. 21** Behavior of total thermal resistance as the flow rate changes and the supplied heat flux changes is presented by  $R_{total}$  vs.  $Q_{total,in}$ . Numbers next to the markers are  $T_{heat,avg}$

The  $R_{total}$  at a given flow rate increases as the supplied heat flux increases, which is somewhat counterintuitive and unexpected. The uncertainty bars for the 25 W/cm<sup>2</sup> are large because the error associated with the temperature difference between the inlet fluid and average chip temperature (~3-5 °C). At higher heat fluxes 50-200 W/cm<sup>2</sup>, the thermal resistance data are closer and small differences can be partially attributed to the temperature-dependent thermophysical properties of R-245fa. More details are presented and discussed in Figure 6. In general, CFD modeling at low heat fluxes and high flow rates are recommended due to large uncertainty in the experimental results. There seems to be a systematic error in calculation of the net heat transferred to the fluid,  $q_{trans}$ , at low heat fluxes of 25-50 W/cm<sup>2</sup>. For the microchannel with 3D-manifold, it is extremely hard to get access to the inlet and outlet plenums in order to insert thermocouples for measuring the inlet and outlet temperatures. As a result, the thermocouples are located at some distance away in the sample holder, and therefore susceptible to error associated with the heat loss from the fluid at the exit and heat gain at the entrance. Therefore, it is expected to see larger (and possibly systematic) error in calculation of  $q_{trans}$ , at the low heat fluxes. We have decided to share the thermal resistance results in order to demonstrate low fidelity results to be expected at low heat fluxes.



**Figure 5. 22** Behavior of total thermal resistance as the flow rate changes and the supplied heat flux changes is presented by  $R_{total}$  vs.  $Q_{total,in}$ . Numbers next to the markers are  $T_{heat,avg}$

In Figure 5.22, the total thermal resistance,  $R_{total}$ , as well as contributing components are plotted as a function of applied heat flux at the fixed flow rate of 0.3 l/min. As expected,  $R_{cond}$  and  $R_{adv}$  are nearly constant as the supplied heat flux increases. Such large increase in  $R_{conv}$  (and thus  $R_{total}$ ) with heat flux is not expected but could be partially attributed to the temperature-dependent thermophysical properties of R-245fa, see Table 5.4. Both  $Pr$  and  $k_f$  decrease as the supplied heat flux increases, therefore, increasing trend in the thermal resistance would be expected but cannot explain the large variation in HTC between 50 to 250 W/cm<sup>2</sup>. As we discussed, this is due to larger uncertainty in measurement of inlet and outlet fluid temperatures that are used in calculation of net heat transferred to fluid,  $q_{trans}$ .

The size of  $R_{total}$  and  $R_{conv}$  uncertainty bars decrease as the supplied heat flux increases because the main sources of  $R_{total}$  and  $R_{conv}$  uncertainties are  $\frac{U_{T_{heat,avg}}}{q''_{trans}}$ ,  $\frac{U_{T_{cp-base,avg}}}{q''_{trans}}$ , respectively (refer Eqn. B.6, B.7 in Appendix B.1), therefore, both of the uncertainties decrease as the  $q''_{trans}$  increases. Detailed description regarding the uncertainty calculation of the thermal resistances is discussed in Appendix B.1.

**Table 5. 4** Prandtl and Reynolds numbers, and thermal conductivity of R-245fa at given heat fluxes with 0.3 l/min flow rate

$q''_{\text{heat}}$ [W/cm <sup>2</sup> ]	Pr	Re	$k_f$ [W/m-K]
51	6.00	739	0.0898
73	5.98	741	0.0897
100	5.97	743	0.0896
153	5.94	750	0.0894
201	5.91	756	0.0892

Heat transfer coefficients of the tested sample,  $h_{\text{effect}}$  (or HTC), are estimated by Eqn. 5.5, and plotted in Figure 5.23. In Figure 5.23, HTC increases with the increased  $Q_{\text{total}}$ . In single-phase, HTC increases with the increased fluid flow rate. The uncertainty bars for the 25 W/cm<sup>2</sup> are large but at higher heat fluxes 50-200 W/cm<sup>2</sup>, the HTC data are closer and small differences can be partially attributed to the temperature-dependent thermophysical properties of R-245fa. The size of the HTC uncertainty,  $U_{\text{HTC}}$ , increases with the increased fluid flow rate,  $Q_{\text{total}}$ , at constant  $q''_{\text{heater}}$  because the temperature difference between the microchannel base,  $T_{\text{cp-base,avg}}$ , and the average fluid temperature,  $T_{\text{f,ref}}$ , decreases with the increased  $Q_{\text{total}}$  (refer Eqn. B.8 in Appendix B.1).

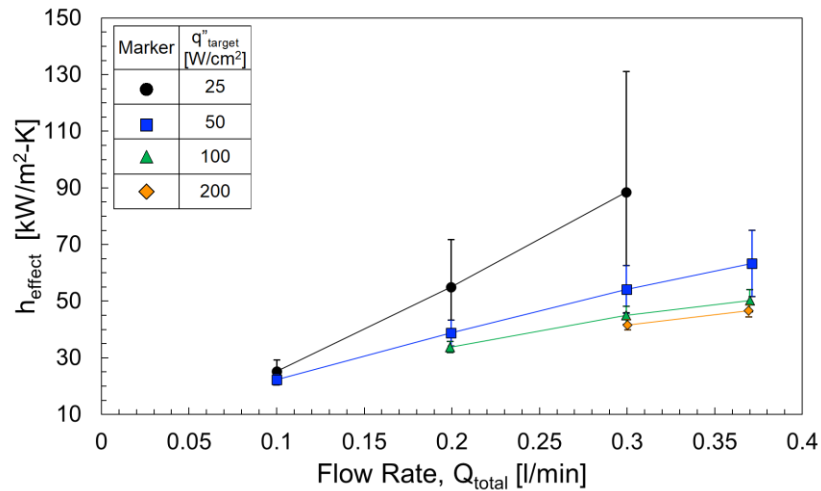


**Figure 5. 23** The measured HTC at the cold-plate microchannel walls vs. flow rate, the overall fin efficiency is from 98.4 to 99.4 %.

### 5.2.2.3 Hydraulic performance: pressure drop

Some general descriptions regarding the changing trends of the pressure drop can be stated as:

- (i) The total pressure drop increases with the increased flow rate,
- (ii) the total pressure drop decreases as the supplied heat flux increases because the dynamic viscosity of the coolant decreases with the increased fluid temperature.

In Figure 5.24a, the resulting plot shows that the change in  $\Delta P_{total}$ ,  $\Delta P_{2,est}$ , and  $\Delta P_{3,est}$  at a supplied heat flux of  $100 \text{ W/cm}^2$ . The experimental pressure drop results are compared with the CFD simulation results. As we discussed in the Data Reduction part,  $\Delta P_1$  and  $\Delta P_4$  are less than 5 % of  $\Delta P_{total}$  and the estimation of  $\Delta P_2$  and  $\Delta P_3$ ,  $\Delta P_{2,est}$ , and  $\Delta P_{3,est}$  respectively, can be obtained using the Bernoulli equation with kinetic energy correction factors (see Eqn. B.11 – B.13 in Appendix B.3). By checking  $\Delta P_2$  and  $\Delta P_3$  values from the CFD results, we are able to calculate the kinetic energy correction factors in the Bernoulli equation, and these estimated kinetic energy correction factors are used to calculate  $\Delta P_{2,est}$  and  $\Delta P_{3,est}$  of the experimental results.

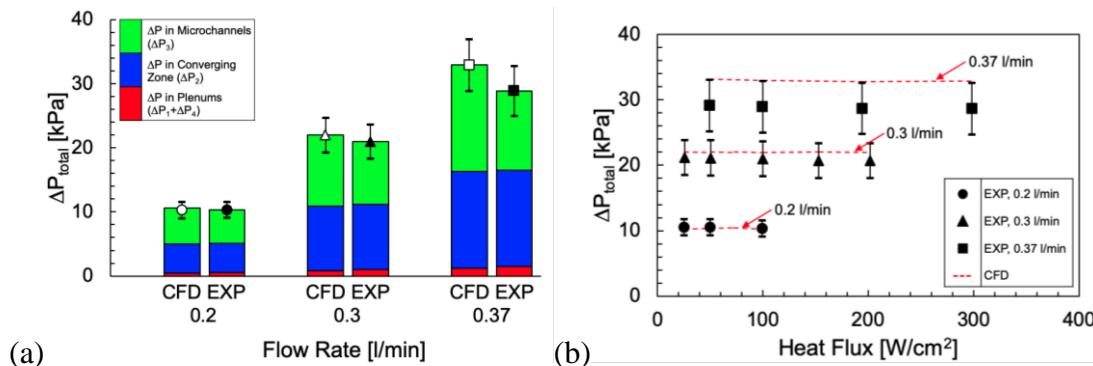


**Figure 5. 24** Pressure drop results from the experiments are compared with the conjugate CFD simulation results. The total pressure drops from the CFD simulations are within the error of the total pressure drops from the experiments. (a) Pressure drops vs. flow rate at a constant heat flux of  $100 \text{ W/cm}^2$ . (b) The total pressure drop results are plotted as a function of supplied heat flux. Since the tested fluidic flow is single-phase, change in the total pressure drop is less than 4 %.

The values of the  $\Delta P_{2,est}$ ,  $\Delta P_{3,est}$  and other important fluidic conditions for the estimation are listed in Table 5.5. The pressure drop results from the CFD simulations are within the uncertainty of the experimental pressure drop results (Figure 5.24a, 5.24b).

Since the flow regime of interest in this paper is single-phase, the  $\Delta P_{\text{total}}$  only changes less than 4 % before it changes to two-phase (Figure 5.24b). Lastly, the size of uncertainty bars in  $\Delta P_{2,\text{est}}$ , and  $\Delta P_{3,\text{est}}$  increase as the flow rate increases. The details regarding calculation of  $\Delta P_{2,\text{est}}$ , and  $\Delta P_{3,\text{est}}$  and their uncertainties are described in Appendix B.3.

**Table 5. 5** Rough estimation of fluid velocities and Reynolds numbers within the gradual contraction region at the constant heat flux of  $100 \text{ W/cm}^2$

Flow Rate [l/min]	$v_1$ [m/s]	$v_2$ [m/s]	$Re_1$	$Re_2$	$\Delta P_{2,\text{est}}$ [kPa]	$\Delta P_{3,\text{est}}$ [kPa]
0.2	4.78E-1	2.37E0	1.41E3	2.88E3	4.60E0	5.25E0
0.3	7.19E-1	3.57E0	2.13E3	4.34E3	1.01E1	9.84E0
0.37	8.88E-1	4.41E0	2.63E3	5.36E3	1.51E1	1.24E1

Figure 5.25 shows the change of measured total pressure drop at the flow rate of 0.3 l/min. As the supplied heat increases, the total pressure drop slowly decreases because the dynamic viscosity of the coolant decreases with the increased fluid temperature. After the onset of nucleate boiling is visually observed at the heat flux of  $254.0 \text{ W/cm}^2$ , the gradual decrease in the total pressure drop is levels off and  $\Delta P_{\text{total}}$  starts to increase as the heat flux increases. As the heat flux increases after the ONB event, the amount of generated vapor keeps increasing and this phenomenon leads to the drastic increase in the total pressure drop.

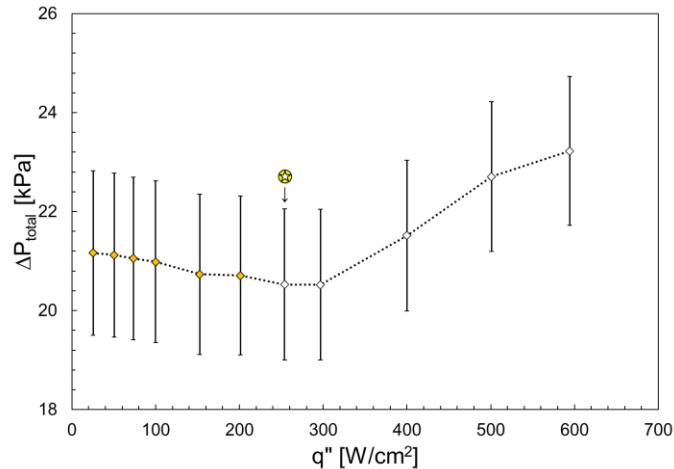


**Figure 5. 25** Total pressure drop vs. supplied heat flux. The void markers indicate that the flow regime is changed to two-phase. Inlet pressure is between 254 – 283 kPa.

### 5.2.3 Two-phase R-245fa

In the two-phase experiments with R-245fa, forced-convective subcooled boiling is dominant heat transfer mechanism. We could achieve heat transfer coefficients up to 61 kW/m<sup>2</sup>-K with low exit vapor quality up to 13 %. The strong condensation effects in the rectangular microchannels prohibits bubbles from growing and coalescing at the microchannel’s wall, and delays transition to slug or annular flow for high heat fluxes [64-66]. In this section, we propose a model that predicts exit vapor quality,  $x_{\text{exit}}$ , near the outlet of the EMMC, and investigate the change of the thermo-fluidic behavior of the EMMC in two-phase cooling regime.

#### 5.2.3.1 Estimation of exit quality

First of all, the exact type of the flow boiling has to be determined. Since the measured fluid temperatures at the inlet and outlet of the EMMC have never reached to the saturated fluid temperature, we can conclude that forced-convective subcooled boiling is the dominant flow boiling type. The energy balance is considered to calculate the exit quality.

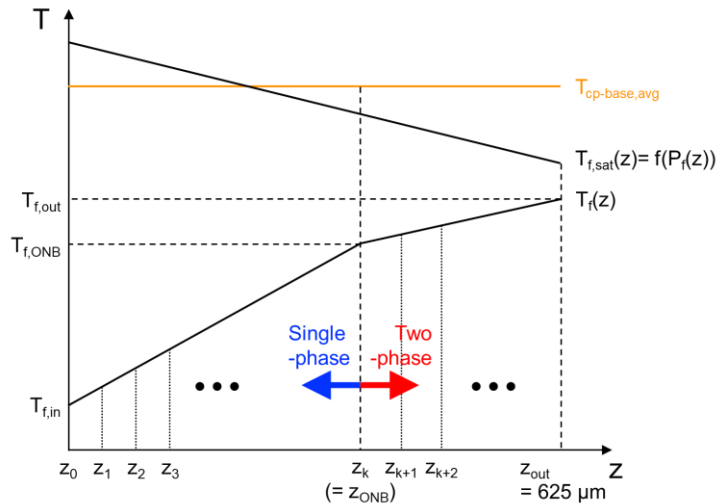


**Figure 5. 26** A schematic to explain the energy balance model for single-/two-phase heat transfer.

A brief schematic is given in Figure 5.26 to explain the principle of estimating exit quality of two-phase heat transfer results. For single-phase flow, the supplied heat only

increases the sensible heat of the liquid except small amount of heat loss ( $< 10\%$ ). For two-phase flow, the supplied energy is transferred into three different forms: i) the latent heat of generated vapor, and ii) increased sensible heat of the remaining liquid (apart from the heated wall), and iii) increased sensible heat of the liquid that is about to be saturated near the heated wall.

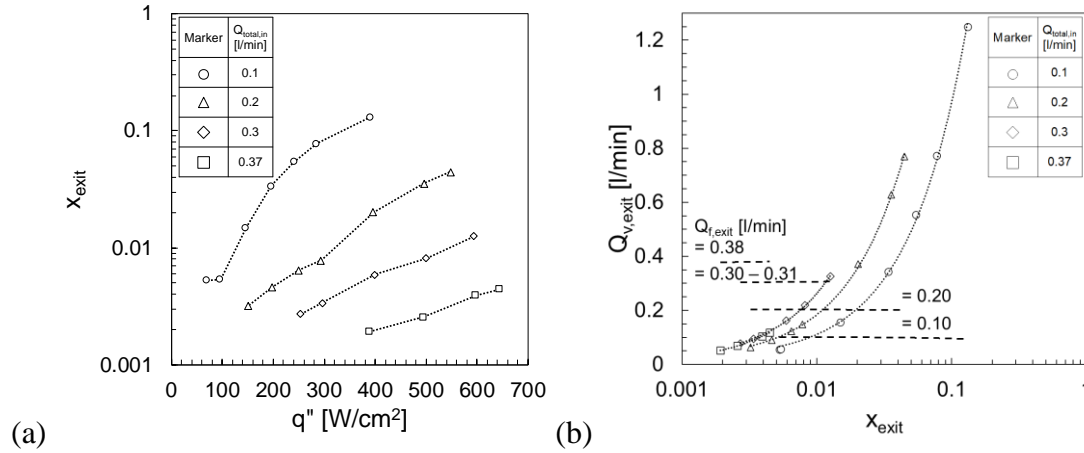
A few assumptions are made for the estimation of  $x_{\text{exit}}$ : i) pressure and temperature in a microchannel linearly change along the flow direction, ii) no heat loss is considered during the two-phase cooling. If we consider the local energy balance in the discretized control volume of the microchannel, the equation can be written as:

$$dq_{\text{supply}} = \dot{m}_{\text{channel}} \cdot \left[ \begin{array}{l} \Delta x(n) \cdot h_{fg}(n) \\ +(1-x(n)) \cdot C_{p,f}(n) \cdot (T_f(n+1) - T_f(n)) \\ +\Delta x(n) \cdot C_{p,f}(n) \cdot (T_{f,\text{sat}}(n+1) - T_f(n+1)) \end{array} \right] \quad (5.11)$$

where  $\Delta x(n) = x(n+1) - x(n)$ , and  $n \geq k$  in Figure 5.26. The exact ONB point has not been observed directly due to limited access inside of the EMMC structure, so the ONB location is assumed to be near the outlet when we first observe the bubbles. As the heat flux increases from the heat flux that initiates the ONB, the ONB location shifts toward upstream of the fluid flow. Since the temperature and pressure values at  $z(0)$  and  $z_{\text{out}}$  are known as the boundary conditions,  $\Delta x(n)$  is the only unknown in Eqn. 5.11. Other thermal properties in Eqn. 5.11 can be estimated by temperature and pressure at the location  $z$ .

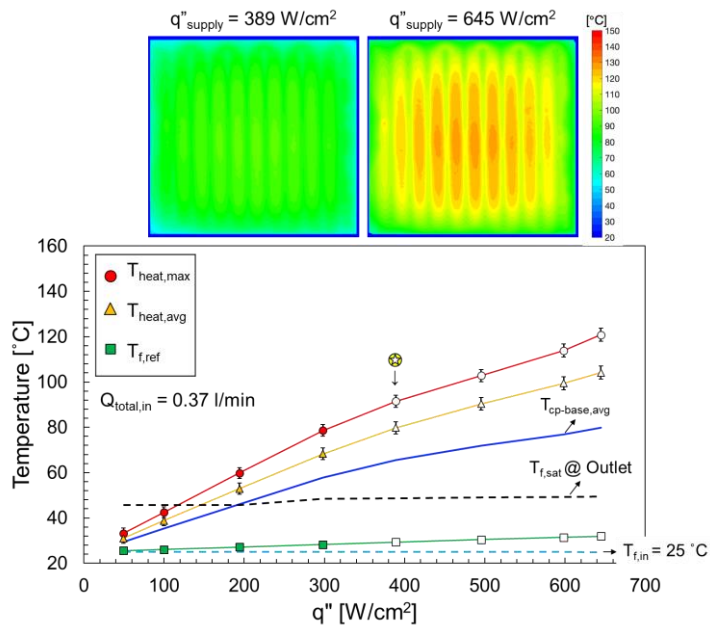
In Figure 5.27a, the exit quality increases with the higher heat fluxes. Among all the test cases with R-245fa, the  $x_{\text{exit}}$  of 13% is the highest with the flow rate of 0.1 l/min. Since more flow rate inhibits bubble generations, the exit vapor quality becomes smaller as the flow rate increases with a given heat flux. In Figure 5.27b, the outlet vapor volume flow rate,  $Q_{v,\text{exit}}$ , is compared to the outlet liquid volume flow rate,  $Q_{f,\text{exit}}$ . The vapor quality is the ratio of generated vapor mass to the total fluid mass. If we assume the velocity is same for the liquid and the vapor in the channel, the volume flow rate of liquid and vapor are the mass flow rate of liquid and vapor divided by the density of liquid and vapor, respectively. Since the vapor density is about 100 times smaller than the liquid density in R-245fa, the volume flow rate of vapor is almost identical to that of liquid

when the exit quality is 1 %. This is the reason we have noticed a lot of bubbles in the tube even with the low exit qualities during the experiments.



**Figure 5. 27** (a) Exit quality vs. heat flux for the flow rates from 0.1 to 0.37 l/min, (b) generated vapor flow rate at the outlet vs. exit quality.

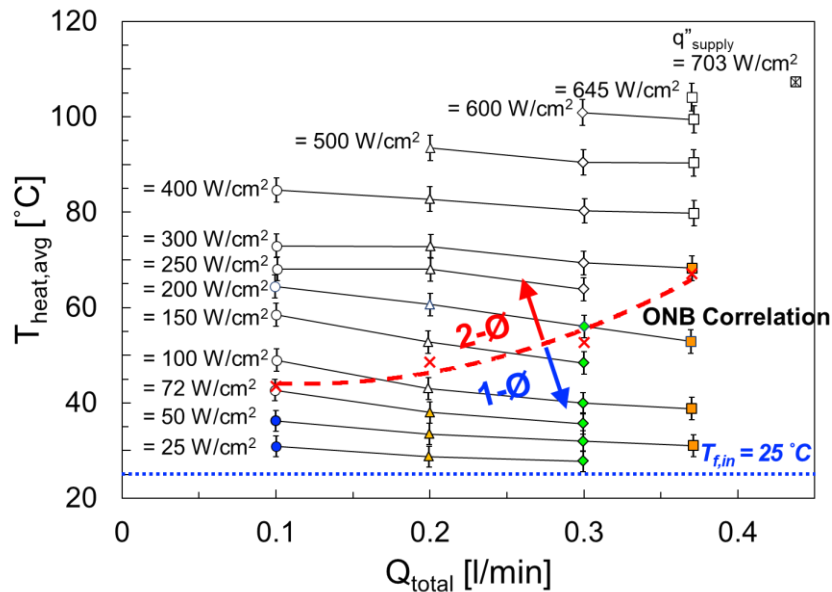
### 5.2.3.2 Temperature behavior



**Figure 5. 28** Temperature behavior against the supplied heat fluxes for the flow rate of 0.37 l/min, IR images taken at the ONB and at the highest heat flux, respectively

During the heat transfer experiments with R-245fa, the heated surface temperature is monitored by an IR camera. The average base temperature of the microchannels under

the heated surface,  $T_{cp-base,avg}$ , is deduced from the measured  $T_{heat,avg}$  by 1-D conduction, and it is adjusted by a few percentages as the heat flux increases. The details about the adjustment in  $T_{cp-base,avg}$  is described in Appendix C.2. The incipient of boiling is captured by a marker (☼) in Figure 5.28 and later figures. At the heat flux of  $194 \text{ W/cm}^2$ ,  $T_{cp-base,avg}$  first exceeds  $T_{f,sat}$ , but no bubble generation is noticed. The incipient bubbles are observed for the first time at  $q'' = 389 \text{ W/cm}^2$ , when the difference between  $T_{cp-base,avg}$  and  $T_{f,sat}$  is  $16.8 \text{ }^\circ\text{C}$  (Figure 5.28). However, the curvature of  $T_{heat,avg}$ ,  $T_{heat,avg}$ ,  $T_{cp-base,avg}$  trendlines is changed and the  $T_{f,sat}$  at the outlet starts shifting up at  $q'' = 300 \text{ W/cm}^2$ . Therefore, these findings may be an indication of early stage of ONB before the incipient bubbles are departed from the microchannel's wall.



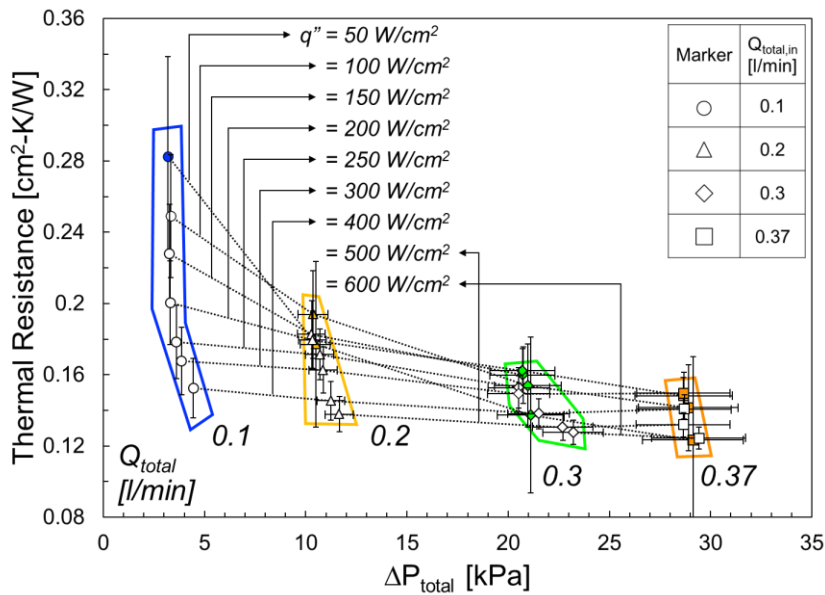
**Figure 5. 29** Summarized  $T_{heat,avg}$  vs.  $Q_{total,in}$  with an ONB estimation line. Colored markers represent single-phase, and empty markers represent two-phase.

Figure 5.29 summarized  $T_{heat,avg}$  as a function of flow rate at given heat fluxes. In addition, the estimated ONB line is superimposed on top of the graph and it shows that the observed ONB points agree well with the estimated ONB line. As flow rate increases from 0.1 to 0.37 l/min, the heat flux for the ONB shifts to higher heat fluxes. However, the current effort to predict the ONB has a clear limitation: the ONB correlation only predicts whether there is initiation of nucleate boiling near the outlet, not at a random location along the microchannel's wall. Since there would be an entrance effect in the

microchannel, the microchannel's wall temperature should show a gradient along the flow direction. If this temperature gradient is taken into account for the ONB estimation, we are able to calculate the ONB at any location along the microchannel wall. However, the local temperature distribution on the microchannel wall cannot be captured in the current experiments and it will be a great subject to study in near future.

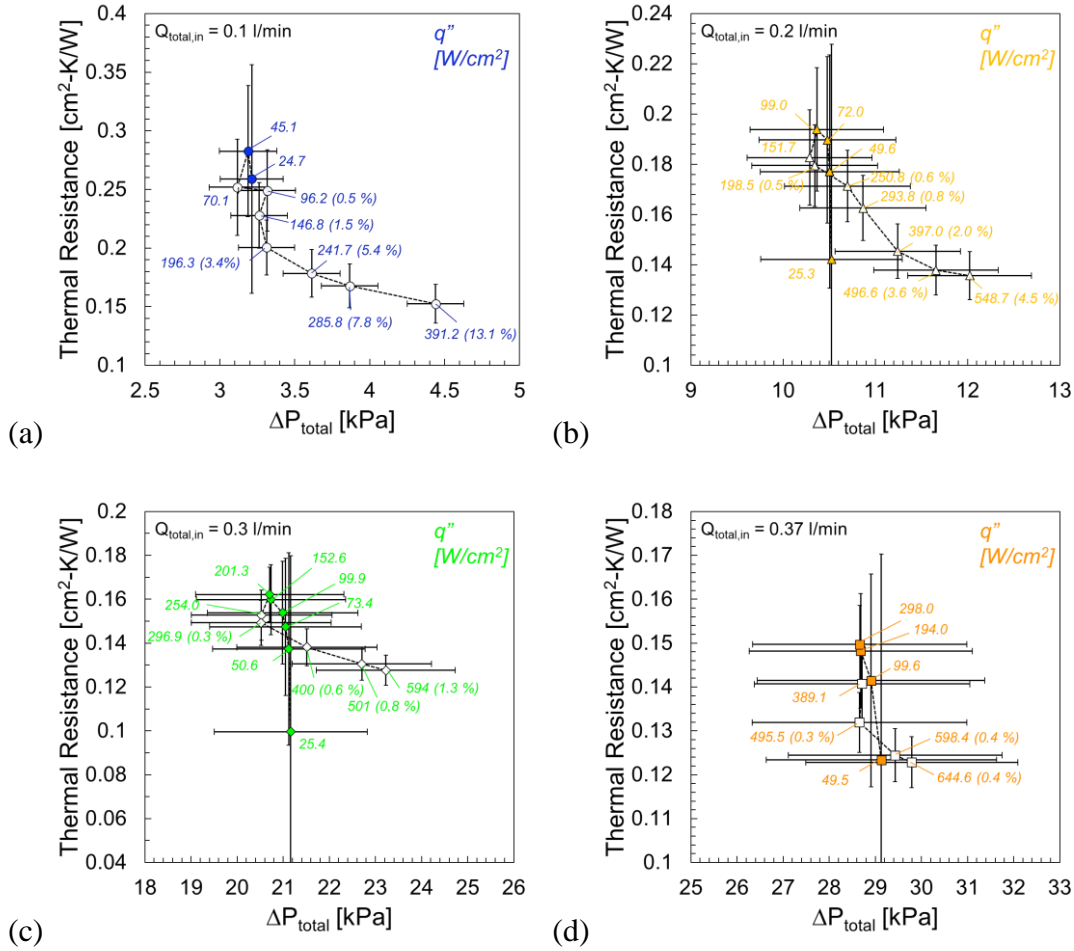
### 5.2.3.3 Thermal resistance and heat transfer coefficient

Figure 5.30 summarizes the thermal resistance as a function of pressure drop for various heat fluxes ranging from 50 to 600 W/cm<sup>2</sup>. In general, the  $R_{total-avg}$  decreases and  $\Delta P_{total}$  increases with the increased flow rates at a given heat flux.



**Figure 5. 30** Summarized  $R_{total,avg}$  vs.  $\Delta P_{total}$  for various heat fluxes from 50 W/cm<sup>2</sup> to 600 W/cm<sup>2</sup>.

Figure 5.31 summarizes the change in  $R_{total,avg}$  as a function of  $\Delta P_{total}$  for single- and two-phase flows. In single-phase cooling regime, thermal resistance slightly goes up which has been discussed in Section 5.2.2.2.



**Figure 5.31**  $R_{total,avg}$  vs.  $\Delta P_{total}$  at a given flow rate from (a) 0.1 to (b) 0.2 to (c) 0.3 to (d) 0.37 l/min. Supplied heat flux and exit vapor quality values are written next to the two-phase markers

In two-phase cooling regime, thermal resistance decreases with the increased heat fluxes because the latent heat starts to contribute to the heat transfer. With the higher heat fluxes, increased liquid superheat near the wall creates more active nucleating sites and more bubbles are generated. Further increase in the heat flux, the more active nucleating sites are created and they are expanding toward upstream of the channel. As the size and the number of bubbles increases with the higher heat fluxes, the bubbles start to coalesce to create a thin air layer near the wall. This air layer plays a role as a thermal insulation barrier between the solid-liquid interface before it departs from the superheated wall. Therefore, the reduction rate of thermal resistance slows down as the heat flux keeps increasing. The indication of this phenomenon is also captured in Figure 5.31a and Figure 5.31b.

We also investigate the effect of exit quality to the heat transfer coefficient of the system in two-phase cooling regime. With the increased heat fluxes, the heat transfer coefficients also increase in Figure 5.32. Interestingly, heat transfer coefficients in the single-phase regime shows a strong correlation with the flow rates. Higher heat transfer coefficients are achieved with higher flow rates (Figure 5.32a). In two-phase flow, the vapor quality is another important parameter to determine the heat transfer coefficient at a given heat flux. In Figure 5.32a, the  $h_{\text{effect}}$  at a heat flux of 390 – 400  $\text{W}/\text{cm}^2$  are 50.8, 50.9, 51.6 and 48.4  $\text{kW}/\text{m}^2\text{-K}$  with the flow rates of 0.1, 0.2, 0.3, and 0.37  $\text{l}/\text{min}$ , respectively. This is because the exit quality is the highest with the flow rate of 0.1  $\text{l}/\text{min}$  and more heat is dissipated in the form of latent heat rather than sensible heat. However, the stronger condensation effect appears with the increased flow rate. During the experiments, the inlet and outlet pressure of the fluid increases with the increased flow rate and it suppresses bubble growth and coalescence, and delays transition to slug or annular flow to higher heat fluxes [64-66]. Eventually, the  $h_{\text{effect}}$  with the flow rate of 0.37  $\text{l}/\text{min}$  shows the best cooling performance among others in Figure 5.32b.

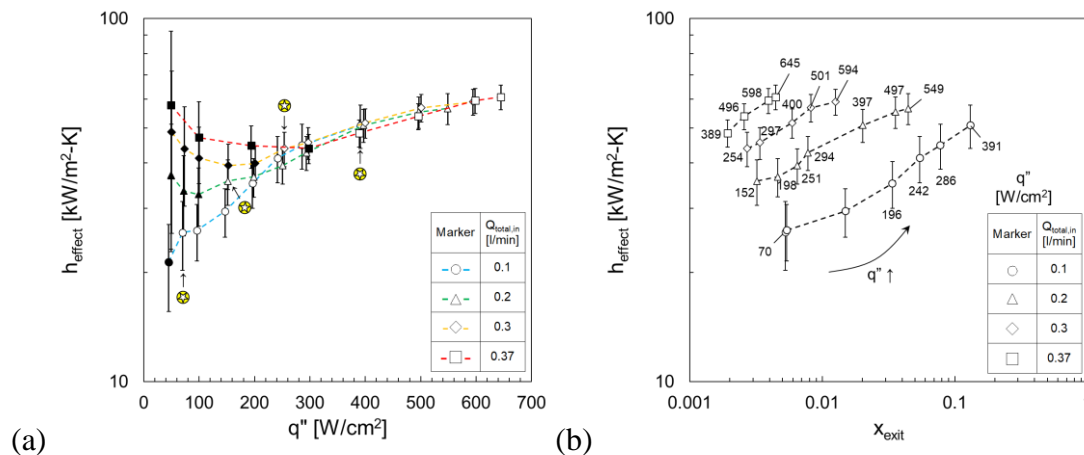


**Figure 5. 32** (a) The  $h_{\text{effect}}$  as a function of heat flux, and (b) the  $h_{\text{effect}}$  as a function of  $x_{\text{exit}}$ . Four different flow rates are tested in single and two-phase regime.

### 5.2.3.4 Hydraulic performance: pressure drop

The change of  $\Delta P_{\text{total}}$  in two-phase flow is also affected by the vapor quality. In Figure 5.33a, the  $\Delta P_{\text{total}}$  decreases as the heat flux increases in single-phase because the dynamic viscosity of the fluid decreases. However, the gradual reduction in the  $\Delta P_{\text{total}}$  levels off and the  $\Delta P_{\text{total}}$  starts to increase after the onset of boiling. Further increase in the heat flux, the void fraction in the microchannel also increases and eventually the  $\Delta P_{\text{total}}$  shoots up.

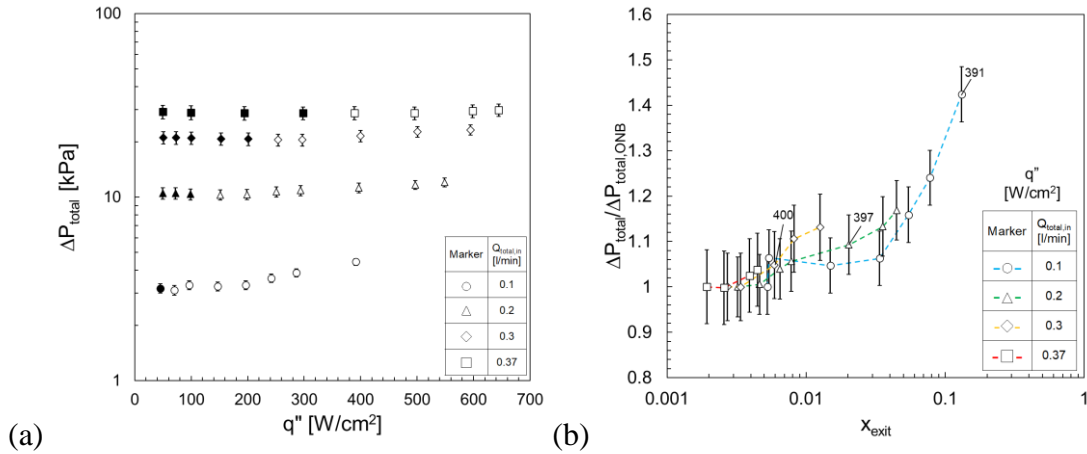


**Figure 5. 33** (a) The  $\Delta P_{\text{total}}$  as a function of heat flux, and (b) normalized  $\Delta P_{\text{total}}$  as a function of  $x_{\text{exit}}$

Since the effect of  $x_{\text{exit}}$  on  $\Delta P_{\text{total}}$  is of our interest, the  $\Delta P_{\text{total}}$  is normalized by  $\Delta P_{\text{total}}$  at the ONB for each flow rate. As shown in Figure 5.33b, the growth rate of  $\Delta P_{\text{total}}$  after ONB is strongly impacted by  $x_{\text{exit}}$ . At the heat flux of 391 – 400 W/cm<sup>2</sup>, the increase in the normalized  $\Delta P_{\text{total}}$  is 42 % when  $x_{\text{exit}}$  is 13 %. However, the increase in the normalized  $\Delta P_{\text{total}}$  is less than 10 % when  $x_{\text{exit}}$  is < 2 % at the same heat fluxes. Again, the increased flow rate leads to the stronger condensation effect in the flow and the generation of bubbles is effectively suppressed [64-66]. Therefore, the growth rate of  $\Delta P_{\text{total}}$  is also effectively suppressed with the reduced exit quality at a given heat flux.

# Chapter 6

## Conclusion and future works

### 6.1 Summary of results and contributions to the field

This dissertation document is a summarized report to study thermofluidic performance of Embedded Microchannels-3D Manifold Cooler (or EMMC) system in single and two-phase regime. At the time the study was started the conceptually similar manifold-microchannel heat exchangers were found but the operational cost of those heat exchangers was not acceptable due to large hydraulic pressure drop [32,71,77]. The Stanford Nanoheat group started to develop more practical designs to be applied to real-world electronics applications and the current EMMC design has been confirmed after multiple design iterations by analytic modeling [44] and conjugate CFD simulations [55].

The overall study of this document consists of three major topics:

- i) Design and microfabrication of the EMMCs for single and two-phase heat transfer experiments,
- ii) Construction of experimental setup and configuration of appropriate measurement procedure
- iii) Data reduction and validation with analytic modeling and CFD simulations

Our first step to develop an EMMC design started with studying thermo-fluidic performance of conventional heat sink designs [44].

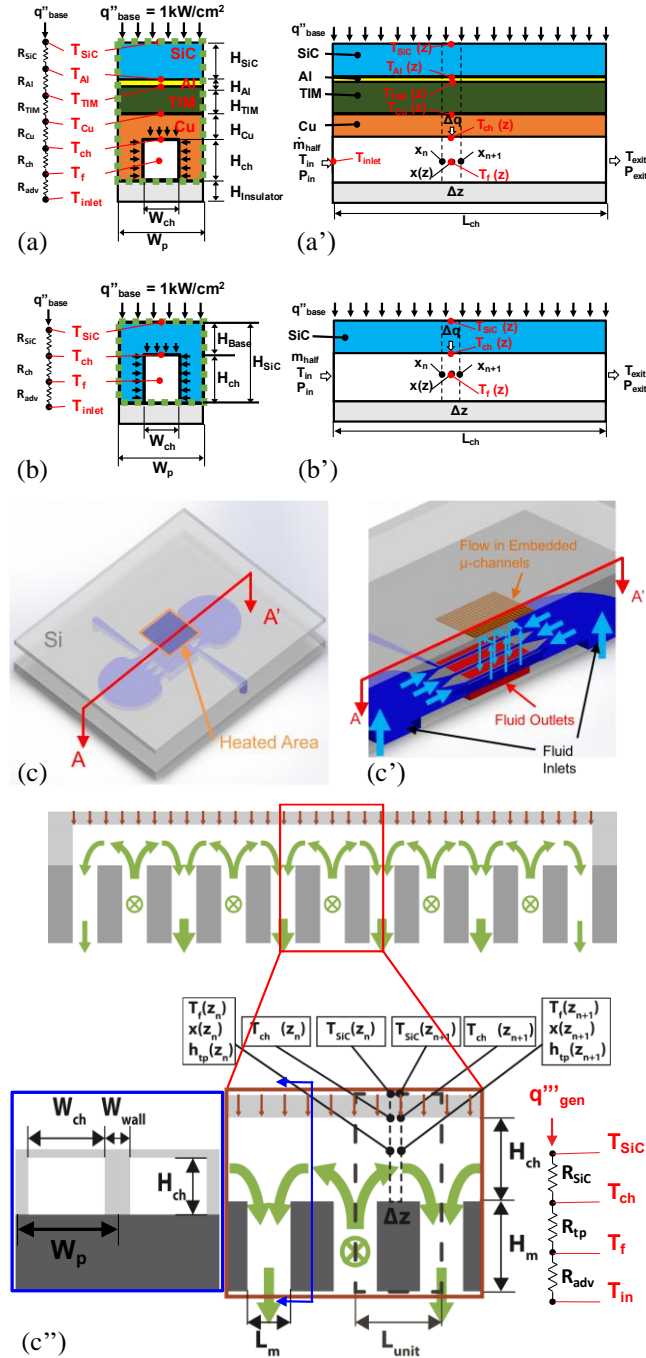


**Figure 6. 1** Configurations of three different cooling strategies. (a, a') **Design A**: cross-sectional views and associated thermal resistance components, (b, b') **Design B**: cross-sectional views and associated thermal resistance components; (c, c', c'') **Design C**: explains embedded cooling with 3D manifold concept, direction of flow from 3D-manifold inlet to channel inlet, traversing channel length, moving out of the channel and entering the outlet of 3D-manifold. Also, thermal resistance components are included.

At the beginning, a reduced order thermofluidic model is used to predict the thermal resistance and pressure drop of the given heat exchanger designs in Figure 6.1. Key findings from the initial study are:

- i) Single-phase flow utilizing water as the working fluid performs worse than that of two-phase flow utilizing R-245fa as the working fluid.
- ii) Embedded cooling strategy (Design B, Figure 6.1) provided lower thermal resistance in comparison to attached heat sink (Design A, Figure 6.1) for the same hydraulic diameters due to the longer conduction path in the attached heat sink approach.
- iii) Total pressure drop decreases with increased hydraulic diameters, but embedded cooling strategy (Design B, Figure 6.1) is limited in channel height and therefore it is difficult to achieve low pressure drop (less or equal to 10 kPa) in single and two-phase flows.
- iv) Embedded cooling with 3D manifold architecture (Design C, Figure 6.1) combines the advantages of lower conduction resistance of embedded cooling approach with shorter flow path of the working fluid providing low pressure drops in the system.

As a result, the embedded microchannels-3D manifold with two symmetric inlets and one vertical outlet design was confirmed for single and two-phase heat transfer applications. The following step is microfabrication of the EMMC samples in Si substrates.

Despite the Si-based MEMS fabrication technique has been studied and well defined by many others, the unique characteristics in the EMMC design require many fabrication challenges.

- i) Microstructures in the EMMC are defined from both top and bottom surface of the Si substrates, and they are etched into the substrates from top and bottom surface.
- ii) Some of the etched microstructures are interconnected and create through-hole features during the etching process.
- iii) Two separate substrates have to be precisely aligned for a eutectic bonding.

The listed fabrication challenges are well documented in Chapter 2. A novel double-sided anisotropic Si etch process has been developed by the Stanford-Toyota alliance and it was documented for a US patent [patent]. In addition to that, the Stanford Nanoheat group has investigated the optimal Au-Si eutectic bonding process conditions and a unique Au-Si eutectic bonding recipe was characterized and developed.

After the microfabrication of the EMMC has finished, a closed-loop flow system is utilized to conduct single and two-phase heat transfer experiments. We have upgraded the existing flow loop for more functionalities: i) installation of an electric circuitry to measure supplied electric power, ii) adding an immersion heater to the customized liquid reservoir to remove noncondensable gas components, iii) implementation of a PI feedback control in the operating program for an accurate control over the flow rate, iv) construction of a new sample holder system with metal frames for the IR measurement setup.

The fabricated EMMC samples have been tested in the flow loop with DI water and R-245fa. The test results are documented in Chapter 5. Thermo-fluidic performance of the tested samples are examined by multiple parameters, maximum and average temperatures of the chip, pressure drop, thermal resistance, average heat transfer coefficient. For the single-phase heat transfer experiments, the experimental results are compared to conjugate numerical simulations for validation purpose. With single-phase DI water, the EMMC is able to remove heat fluxes up to  $1111 \text{ W/cm}^2$  with maximum pressure drop of 30 kPa, while the flow rate is limited up to 400 g/min. The measured total thermal resistance is  $< 0.1 \text{ W/cm}^2\text{-K}$ , but we have confirmed that there is enough room to reduce the convection and conduction thermal resistance in the EMMC [JEP\_CFD]. R-245fa has been used for single and two-phase heat transfer experiments and we confirmed that two-phase boiling in the tested samples are forced convective subcooled boiling. Thanks to the strong condensation effect in the two-phase flow, the nucleate boiling event is delayed by increasing loop pressure followed by increased flow rate. The maximum removable heat flux with R-245fa is  $703 \text{ W/cm}^2$  with maximum pressure drop of 38 kPa, while the flow rate is 586 g/min. The measured thermal resistance at the maximum heat flux (but not CHF) is  $0.15 \text{ W/cm}^2\text{-K}$ , which is higher than the thermal resistance of single-phase DI water.

As we recall the first part of the conclusion, the existing reduced order thermofluidic model is not sufficient to predict the thermofluidic performance of the EMMC based on the experimental results. To fill the gap between the analytic model and the experimental data, we have utilized conjugate numerical simulations and try to develop new correlations to predict friction factors and average Nusselt numbers for EMMCs with single-phase DI water. In Section 5.2.1.4 and 5.2.1.5, we confirmed that the experimental results agree well with the CFD results, falling within  $\pm 10 - 30$  % error bands of the CFD results.

Lastly, the conjugate CFD simulations are proven to be a good method to estimate the thermofluidic performance of EMMCs with single-phase coolants. To extend the discussion from this standpoint, the CFD simulation can be used to optimize the thermofluidic performance of the EMMC design. The ultimate goal of the EMMC geometric design improvement is to lower the hotspot surface temperature as well as the system pressure drop for a given heat flux and flow rate. In general, three strategies are proposed to improve the EMMCs thermofluidic performance in Chapter 4: (1) Symmetric placement of manifold inlet/outlet conduits for single-phase increases the flow path length, resulting in 38% and 5.5% reduction in pressure drop and thermal resistance from the baseline EMMC design, respectively. (2) Reduction in the thickness of the cold-plate substrate from 500 to 200  $\mu\text{m}$ , nearly archives the lower bond of silicon substrate conduction thermal resistance of  $0.03 \text{ cm}^2\text{-K/W}$ . (3) The cold-plate microchannels fluid-solid effective surface area increase can be increased wither by reducing the microchannel's width,  $W_{\text{cp}}$  (D8), or fin width,  $W_{\text{cp,fin}}$  (D9) However, the pressure drop increases in the first approach but the trend is reversed for the second approach due to the reduced mass flux (velocity) within CP's microchannels.

## 6.2 Directions for future work

The biggest hurdle to understand thermofluidic behavior of the EMMCs in two-phase flow is the lack of measurement data. Several important two-phase flow data can be found by the flow visualization: i) finding onset-of-nucleate boiling sites and their density change, ii) the transition of flow regimes, and iii) measurement of film thickness.

However, the visual access is limited to the EMMC structure due to its structural complexity. Cetegen [40] reported flow visualization results in a single manifold microchannel unit with a channel height of 2.42 mm, channel width of 70  $\mu\text{m}$  and 225  $\mu\text{m}$ , and a channel length of 3.875 mm with HFE-7100. The reported flow regimes were similar to the traditional microchannels of the same dimensions for the tested mass fluxes and heat fluxes [40].

However, the geometries used in the current EMMC are much smaller than the reported single manifold microchannel [40] and we need to generate the visualization data from our own geometries. If the visualization data is added to the current study, it will complete the discussion regarding onset-of-nucleate boiling in subcooled developing flow regime which is reported in this document. In addition, the accurate measurement of fluid velocity and pressure change along the microchannel will be the first step to develop the accurate correlations to predict friction factors and Nusselt numbers from experiments.

Another interesting topic is additive manufacturing of the EMMC. Since the microfabrication of the EMMC samples takes huge amount of production time and cost, the additive manufacturing is one of the promising options for prototyping future EMMC structures.

Figure 6.2 shows three design candidates for future manifold structure. The minimum dimension for the 3D printing required by many vendors is 500  $\mu\text{m}$  which is still acceptable compared to the current geometry. However, we are hoping to push this limit down to 200  $\mu\text{m}$  to further improve thermofluidic performance of the EMMCs.

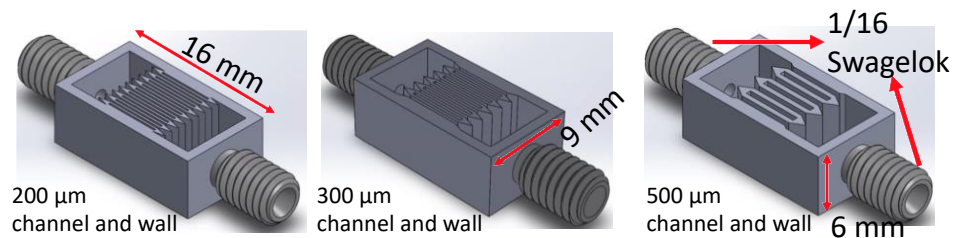


**Figure 6. 2** Sample designs for manufacturability test, the minimum wall thickness dimension used in each design is 200/300/500  $\mu\text{m}$ , respectively.

The target material for the additive manufactured 3D manifold is Titanium. The first reason to choose Ti as the most promising material is that the coefficient of thermal expansion of Titanium is  $8.6 \mu\text{m}/\text{m}\cdot^\circ\text{C}$  [69], which is comparable to that of Si or SiC,  $2.5 - 4.5 \mu\text{m}/\text{m}\cdot^\circ\text{C}$  [70]. In addition, Professor Ohadi's group from the University of Maryland has reported successful Sn-Ag bonding of Titanium manifold to Si wafer [71]. They reported that the pressure required to burst was 9 MPa, which is about 9 times higher than the maximum expected operating pressure for their two-phase system [71]. Therefore, Ti is a promising material for new manifold structures for two-phase heat transfer experiments.

From an industrial application standpoint two strategies should be pursued. First, the flow visualization study on various unit microchannel-manifold geometries has to be conducted to give a comprehensive understanding of the EMMC's thermo-fluidic performance to people. The effect of geometry and thermo-fluidic properties of various working fluids on the device's performance are always the number one interest to the industry. Second, try to investigate the manufacturing capability of the existing 3D printing technology and propose the most practical option for real applications. The size, cost, and turnaround time should be considered for the EMMC production and eventually we need to think about the integration of the 3D printed samples to the actual power electronics.

# Appendix A

## A.1 Experimental test conditions

Since inlet or outlet pressure is not maintained constant during the experiments, the inlet pressure of the test section is changing by the flow rates as well as the heat fluxes. Inlet fluid temperature is the only parameter that is kept constant, 25 °C, in all test cases.

**Table A. 1** Experimental test conditions with single-phase DI water

$Q_{total,in}$		$q''_{supply}$ [W/cm <sup>2</sup> ]	$P_{f,in}$ [kPa]	$T_{f,in}$ [°C]
[g/min]	[l/min]			
33	0.03	60 – 239	146 – 157	25
66-69	0.07	60 – 248	191 – 202	25
101-104	0.10	61 – 252	234 – 247	25
200	0.20	51 – 891	203 – 223	25
300	0.30	49 – 1004	261 – 289	25
400	0.40	101 – 1111	323 – 355	25

**Table A. 2** Experimental test conditions with single-/two-phase R-245fa

$Q_{total,in}$		$q''_{supply}$ [W/cm <sup>2</sup> ]	$P_{f,in}$ [kPa]	$T_{f,in}$ [°C]
[g/min]	[l/min]			
133 – 135	0.10	10 – 391	219 – 257	25
266 – 268	0.20	25 – 549	241 – 290	25
401	0.30	10 – 594	254 – 301	25
495 – 497	0.37	49 – 645	332 – 369	25

## A.2 Test conditions for conjugate CFD simulations

Uniform heat flux is applied on the very top surface of the serpentine heater, and the exposed surfaces are assumed to be adiabatic. Therefore, the sensible heat calculated from the experimental results is used in the CFD simulations ignoring heat loss to the surroundings (i.e. natural convection).

**Table A. 3** Test matrix for the conjugate CFD simulations with single-phase DI water

$Q_{total,in}$		$q''_{supply}$ [W/m <sup>2</sup> ]	$T_{f,in}$ [K]	# of Iteration	# of mesh elements	CFD Domain
[g/min]	[kg/s]					
33	5.42EE-4 – 5.50E-4	8.98E5 – 3.58E6	298.15	5000	5.39E6	Full-scale
66-69	1.10E-3 – 1.14E-3	8.99E5 – 3.72E6	298.15	5000	5.39E6	Full-scale
101-104	1.68E-3 – 1.72E-3	9.07E5 – 3.77E6	298.15	5000	5.39E6	Full-scale
200	8.32E-4 – 8.33E-4	6.01E5 – 1.30E7	298.15	15000	11.03E6	¼-cut
300	1.25E-3	5.60E5 – 1.47E7	298.15	15000	11.03E6	¼-cut
400	1.67E-3	1.23E6 – 1.63E7	298.15	15000	11.03E6	¼-cut

**Table A. 4** Experimental test conditions with single-phase R-245fa

$Q_{total,in}$		$q''_{supply}$ [W/m <sup>2</sup> ]	$T_{f,in}$ [K]	# of Iteration	# of mesh elements	CFD Domain
[g/min]	[kg/s]					
133 – 135	5.42EE-4 – 5.50E-4	1.57E5 – 6.75E5	298.15	5000	2.50E7	¼-cut
266 – 268	1.11E-3 – 1.12E-3	1.57E5 – 1.48E6	298.15	5000	2.50E7	¼-cut
401	1.67E-3 – 1.68E-3	1.57E5 – 3.02E6	298.15	5000	2.50E7	¼-cut
495 – 497	2.06E-3 – 2.07E-3	7.41E5 – 4.46E6	298.15	5000	2.50E7	¼-cut

### A.3 Mesh dependence study

*Single-phase DI water,  $Q_{total,in} < 0.1$  l/min:* A mesh size independence study is conducted with four different number of mesh elements, from 1.11E6 to 10.9E6, and the results are plotted in Figure A.1. There is less than 0.31% change in the average heater temperature,  $T_{heater,avg}$ , and 1.7% change in the total pressure drop,  $\Delta P_{total}$ , if the number of mesh element is higher than 3.19E6. Therefore, the number of mesh element used in this study was 5.39E6 based on the mesh independence study.

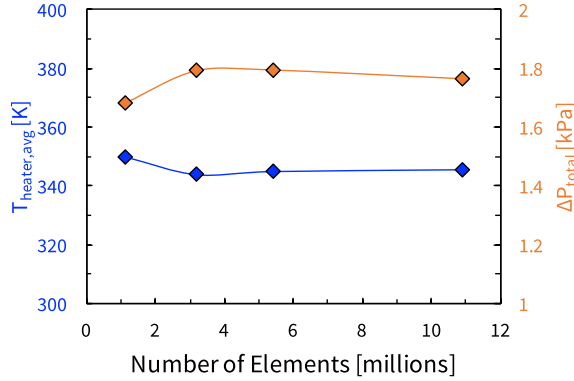


**Figure A. 1** A study of mesh element independence at  $T_{f,in} = 293$  K,  $Q_{total,in} = 0.001$ kg/s,  $q'' = 4,494,517$  W/m<sup>2</sup> conditions. The number of mesh elements used in the study are from 1.11E6 to 3.19E6 to 5.40E6 to 1.09E7.

**Single-phase DI water,  $Q_{total,in} \geq 0.2$  l/min:** A mesh size independence study is conducted with six different number of mesh elements, from 3.27E6 to 1.42E7, and the results are plotted in Figure A.2. There is less than 0.13% change in the average heater temperature,  $T_{\text{heater,avg}}$ , and 0.91 % change in the total pressure drop,  $\Delta P_{\text{total}}$ , if the number of mesh element is higher than 1.10E7. Therefore, the number of mesh element used in this study was 1.10E7 based on the mesh independence study.

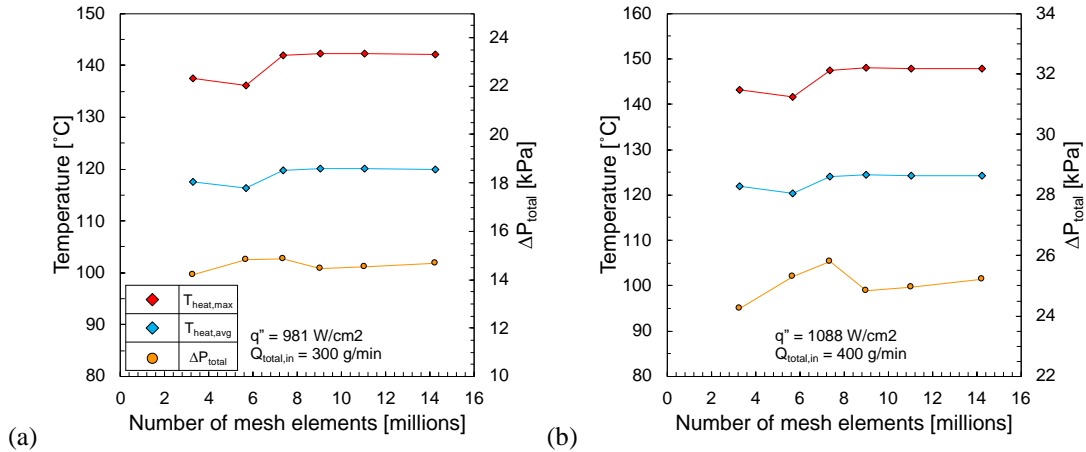


**Figure A. 2** A study of mesh element independence at  $T_{f,in} = 293.15$  K,  $Q_{total,in} = 5.0 - 6.67E-3$  kg/s,  $q'' = 14,703,889 - 16,296,666$  W/m<sup>2</sup> conditions. The number of mesh elements used in the study are from 3.27E6 to 1.42E7.

**Single-phase R-245fa:** The experimental results are validated by conjugate numerical simulations, ANSYS Fluent 18.1, for the exact EMMC geometry (Table 2.1). The thermo-fluidic and the solver conditions for the mesh independence study are listed in Table A.5.

**Table A. 5** Experimental test conditions with single-phase R-245fa

Parameter	Unit	Value
Supplied Heat Flux	W/m <sup>2</sup>	4.464E6
Mass Flow Rate	kg/s	8.263E-3
Inlet Temperature	K	2.981E2
Solver model	-	SST k-omega (turbulent)

The number of mesh elements varies from 5 to 32 millions, and the results are plotted in Figure A.3. There are less than 0.6 % change in the average and maximum heater temperature, and the total pressure drop if the number of mesh elements is more than 25 millions. In addition, the experimentally measured temperature and pressure drop values are superimposed in Figure A.3 and the CFD simulation results are well matched to the experimental results. Therefore, we have used 25 millions of mesh elements in this study.

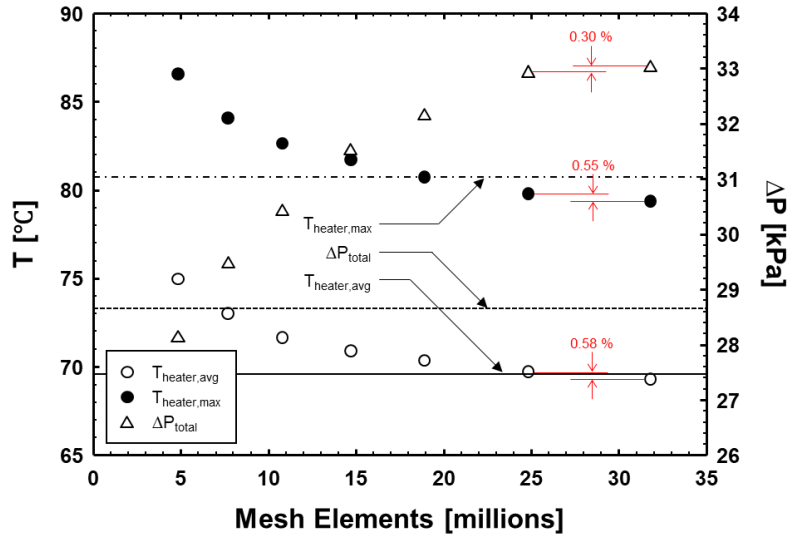


**Figure A. 3** Summarized heater temperatures and pressure drop results for the mesh independence study. The results are plotted as a function of the mesh elements. The results with more than 25 millions of mesh elements show good simulation convergence, < 0.6 %.

#### A.4 Summarized CFD simulation results

*single-phase DI water,  $Q_{total,in} \leq 0.10$  U/min:* Numerical simulations are conducted for the single-phase DI water test cases outlined in Table A.1, the results for total

pressure drop, maximum and average heater temperatures, total thermal resistance of the  $\mu$ -cooler are given in the Table A.6.

As noted in Section 2.1, due to microfabrication defects only four RTD5, 6, 7, and 9 were functional (see Figure 2.2a) for the lower flow rate cases (equal or less than 0.1 l/min of  $Q_{\text{total,in}}$ ) with single-phase DI water. Therefore, the calculated average surface temperature using these four RTDs,  $T_{\text{heat,avg-local}}$ , is not a precise representation of the average temperature over the entire surface of the heater,  $T_{\text{heat,avg-global}}$ . The scaling factors  $f_1$  and  $f_2$ , are calculated using CFD simulations, represent the ratios between  $T_{\text{heat,avg-local}}$  to  $T_{\text{heat,avg-global}}$ ,  $T_{\text{heat,max}}$ , respectively, and are given columns 6 and 7 of Table A.6.

**Table A. 6** Numerically predicted thermo-fluidic information in single-phase DI water test cases,  $Q_{\text{total,in}} \leq 0.10$  l/min

$q''_{\text{supply}}$ [W/cm <sup>2</sup> ]	$Q_{\text{total,in}}$ [l/min]	$\Delta P_{\text{total}}$ [kPa]	$T_{\text{heat,max}}$ [°C]	$T_{\text{heat,avg-global}}$ [°C]	$f_1 =$ $T_{\text{heat,avg-global}} / T_{\text{heat,avg-local}}$	$f_2 =$ $T_{\text{heat,max}} / T_{\text{heat,avg-local}}$	$R_{\text{total-avg}}$ [cm <sup>2</sup> -K/W]
60	3.28E-2	0.3679	42.78	39.78	1.0604	1.1404	0.2466
60	6.61E-2	1.0321	37.68	35.90	1.0546	1.1069	0.1817
61	1.01E-1	2.0377	35.66	34.36	1.0520	1.0919	0.1546
99	3.26E-2	0.3522	54.09	49.25	1.0815	1.1877	0.2448
100	6.74E-2	1.0496	45.70	42.86	1.0768	1.1482	0.1787
100	1.02E-1	2.0491	42.39	40.29	1.0742	1.1303	0.1533
239	3.31E-2	0.3237	91.82	81.26	1.1184	1.2638	0.2356
248	6.87E-2	1.0389	74.28	67.84	1.1219	1.2282	0.1728
252	1.04E-1	2.0649	67.63	62.63	1.1240	1.2138	0.1495

# Appendix B

## B.1 Uncertainty study in EMMC

Here we carefully investigate the uncertainty [72] in the experimental data for surface temperature, thermal resistance and heat transfer coefficient as well as pressure drop.

As  $q_{\text{heater}}$  is calculated by two measured values,  $\Delta V_{\text{heater}}$ , and  $I_{\text{heater}}$ , in Eqn. 1, the measurement error is considered to calculate the uncertainty of  $q_{\text{heater}}$ :

$$(U_{q_{\text{heater}}})^2 = \left[ \begin{array}{l} (I_{\text{heater}} \cdot U_{\Delta V_{\text{heater}}})^2 \\ + (\Delta V_{\text{heater}} \cdot U_{I_{\text{heater}}})^2 \end{array} \right] \quad (\text{B.1})$$

the measurement errors,  $\frac{U_{\Delta V_{\text{heater}}}}{\Delta V_{\text{heater}}}$ ,  $\frac{U_{I_{\text{heater}}}}{I_{\text{heater}}}$ , are  $\pm 0.1\%$  and the uncertainty of  $q_{\text{heater}}$  is calculated to be  $\pm 0.14\%$ . The uncertainty of the transferred heat,  $q_{\text{trans}}$ , is sum of the uncertainty of  $dq_{\text{trans},i}$ :

$$(U_{dq_{\text{trans},i}})^2 = \left( \dot{m} \cdot \frac{C_{p,i} + C_{p,i+1}}{2} \right)^2 \cdot \left[ \begin{array}{l} \left( \delta_T \cdot \frac{U_{\dot{m}}}{\dot{m}} \right)^2 + \left( \frac{U_{T_{f,\text{in}}}}{n} \right)^2 \\ + \left( \frac{U_{T_{f,\text{out}}}}{n} \right)^2 + \left( \delta_T \cdot \frac{U_n}{n} \right)^2 \end{array} \right] \quad (\text{B.2})$$

$$U_{q_{\text{trans}}} = \sqrt{\sum_{i=1}^n (U_{dq_{\text{trans},i}})^2} \quad (\text{B.3})$$

the uncertainty of the saturated specific heat of the fluid is not considered in Eqn. B.2 and B.3. As noted, the uncertainty of  $dq_{\text{trans},i}$  is proportional to mass flow rate in Eqn. B.2.

The uncertainties of  $T_{\text{heater,avg}}$ ,  $Z_{\text{heater}}$  are given by:

$$\left( U_{T_{\text{heater,avg}}} \right)^2 = \left[ \begin{array}{l} (U_{T_0})^2 + \left( \frac{Z_{\text{heater}}}{\alpha \cdot Z_0} \cdot \frac{U_{Z_0}}{Z_0} \right)^2 \\ + \left( \frac{U_{Z_{\text{heater}}}}{\alpha \cdot Z_0} \right)^2 + \left( \frac{Z_{\text{heater}} - Z_0}{\alpha \cdot Z_0} \cdot \frac{U_{\alpha}}{\alpha} \right)^2 \end{array} \right] \quad (\text{B.4})$$

$$\left( U_{Z_{\text{heater}}} \right)^2 = \left( \frac{U_{\Delta V_{\text{heater}}}}{I_{\text{heater}}} \right)^2 + \left( Z_{\text{heater}} \cdot \frac{U_{I_{\text{heater}}}}{I_{\text{heater}}} \right)^2 \quad (\text{B.5})$$

Based on the Eqn. B.4 and Table 5.5, the error in  $T_{\text{heater,avg}}$  is less than 0.8 °C.

The uncertainties of  $R_{\text{total}}$ ,  $R_{\text{conv}}$  are expressed as:

$$\left( U_{R_{\text{total}}} \right)^2 = \left[ \begin{array}{l} \left( \frac{U_{T_{\text{heater,avg}}}}{q''_{\text{trans}}} \right)^2 + \left( \frac{U_{T_{f,\text{in}}}}{q''_{\text{trans}}} \right)^2 \\ + \left( R_{\text{total}} \cdot \frac{U_{q''_{\text{trans}}}}{q''_{\text{trans}}} \right)^2 \end{array} \right] \quad (\text{B.6})$$

$$\left( U_{R_{\text{conv}}} \right)^2 = \left[ \begin{array}{l} \left( \frac{U_{T_{\text{cp,base,avg}}}}{q''_{\text{trans}}} \right)^2 + \left( \frac{U_{T_{f,\text{ref}}}}{q''_{\text{trans}}} \right)^2 \\ + \left( R_{\text{conv}} \cdot \frac{U_{q''_{\text{trans}}}}{q''_{\text{trans}}} \right)^2 \end{array} \right] \quad (\text{B.7})$$

As the supplied heat flux increases, the size of denominators on the right-side of the Eqn. B.6 and B.7 increases. As a result, the uncertainty of  $R_{\text{total}}$  and  $R_{\text{conv}}$  decrease with the increased heat flux.

The uncertainty of HTC is given by:

$$\left( \frac{U_{h_{\text{effect}}}}{h_{\text{effect}}} \right)^2 = \left[ \begin{array}{l} \left( \frac{U_{q_{\text{trans}}}}{q_{\text{trans}}} \right)^2 + \left( \frac{U_{A_{\text{wet}}}}{A_{\text{wet}}} \right)^2 + \\ \left( \frac{U_{T_{\text{cp-base,avg}}}}{T_{\text{cp-base,avg}} - T_{f,\text{ref}}} \right)^2 + \left( \frac{U_{T_{f,\text{ref}}}}{T_{\text{cp-base,avg}} - T_{f,\text{ref}}} \right)^2 \end{array} \right] \quad (\text{B.8})$$

With a constant heat flux condition,  $T_{f,\text{ref}}$  in the denominator of the third and fourth terms in Eqn. B.8 is constant and  $T_{\text{cp-base,avg}}$  decreases as the flow rate increases. Therefore,  $T_{\text{cp-base,avg}} - T_{f,\text{ref}}$  should decrease as the flow increases at a constant heat flux. As a result, the size of HTC uncertainty bar increases as the flow rate increases. In addition, the size of HTC uncertainty bar also increases as the supplied heat flux decreases. The uncertainty of  $q_{\text{trans}}$  calculated by the Eqn. B.2 and B.3 is a function of  $n$ , which is the number of intervals between  $T_{f,\text{out}}$  and  $T_{f,\text{in}}$ . The  $n$  is reduced as the heat flux decreases because the size of temperature interval is fixed but  $T_{f,\text{out}} - T_{f,\text{in}}$  decreases. In

the Eqn. D-1, the  $(U_n/n)$  is one of the terms to attribute to the uncertainty of  $dq_{\text{trans},i}$ , therefore, the reduced  $n$  leads to the increased uncertainty of  $dq_{\text{trans},i}$ .

For single-phase DI water with flow rate  $\leq 0.1$  l/min, we carefully investigate the uncertainty [72] in the experimental data for i) surface temperature measured using RTDs, ii) thermal resistance and heat transfer coefficient as well as iii) pressure drop.

i) Due to microfabrication defects only four RTD5, 6, 7, and 9 were functional (located at upper-right area of the heater, see Figure 2.2a). Therefore, the calculated average surface temperature using these four RTDs,  $T_{\text{heater,avg-local}}$ , is not a precise representation of the average temperature over the entire surface of the heater,  $T_{\text{heater,avg-global}}$ . The scaling factors  $f_1$  and  $f_2$ , are calculated using CFD simulations, represent the ratios between  $T_{\text{heater,avg-local}}$  to  $T_{\text{heater,avg-global}}$ ,  $T_{\text{heater,max}}$ , respectively (see Table A.5). The associated uncertainty of  $T_{\text{heater,avg-global}}$ , and  $T_{\text{heater,max}}$  are estimated to 1.4 – 3.1 % considering  $\pm 1$  °C uncertainty of the K-type thermocouple to measure  $T_{f,\text{in}}$  and  $T_{f,\text{out}}$ .

ii) The experimental uncertainties of  $q_{\text{trans}}$ ,  $T_{\text{heater,max}}$ ,  $T_{f,\text{in}}$ ,  $T_{f,\text{out}}$  are 6.4 – 63.0 %,  $< 3$  %,  $\pm 1$  °C, and  $\pm 1$  °C, respectively. As a result,  $U_{R_{\text{total-max,EXP}}}$ ,  $U_{R_{\text{adv,EXP}}}$  are estimated to be in the range of 6.8 – 64.4 %, 8.8 – 63.2 %, respectively. The biggest uncertainties in  $R_{\text{total-max,exp}}$  and  $R_{\text{advection,exp}}$  can be found at the lowest heat flux, and the highest flow rate. The smallest uncertainties in  $R_{\text{total-max,exp}}$  and  $R_{\text{advection,exp}}$  can be achieved vice versa.

iii) The experimental uncertainties in  $q_{\text{trans}}$ ,  $A_{\text{wet}}$ ,  $T_{\text{cp-base,avg}}$ ,  $T_{f,\text{ref}}$  are 6.4 – 63.0 %, 3.1 %, 1.6 – 5.2 %, and 1.9 – 2.7 %, respectively. We neglected the uncertainty of  $\eta_o$  which was minimal to account for the uncertainty of  $h_{\text{effect}}$ . The first term in Eqn. B.8 is a main contributor to the uncertainty in  $h_{\text{effect,EXP}}$ , and  $U_{h_{\text{effect,EXP}}}$  is estimated to be in the range of 8.1 to 69.9 %. In addition, the uncertainty of  $h_{\text{effect,EXP}}$  increases as the flow rate increases because the temperature difference between  $T_{\text{cp-base,avg}}$  and  $T_{f,\text{ref}}$  decreases at a given heat flux. Lastly, the error for predicted HTC,  $h_{\text{effect,CFD}}$ , is due to the differences between the target u-cooler dimensions and those of the microfabricated device.

## B.2 Onset-of-Nucleate Boiling study in EMMC

To confirm that flow and heat transfer regime remain single-phase, we evaluated the onset of nucleate boiling for the  $\mu$ -cooler geometry, heat flux levels and flow conditions of the present work using the following correlation [73]:

$$\sqrt{T_{\text{wall}}} - \sqrt{T_{\text{f,sat}}} \geq \sqrt{2 \cdot \frac{\sigma_{\text{f,sat}}(1 + \cos\theta)}{\rho_{\text{v,sat}} \cdot h_{\text{fg,sat}}} \cdot \frac{q''_{\text{wall}}}{k_{\text{f}}}} \quad (\text{B.9})$$

$$q''_{\text{wall}} = \frac{q''_{\text{trans}}}{N_{\text{cp}} \cdot (w_{\text{cp}} + 2\eta_{\text{o}} \cdot H_{\text{cp}}) \cdot L_{\text{cp}}} \quad (\text{B.10})$$

where  $T_{\text{wall}}$  and  $T_{\text{f,sat}}$  are the microchannel wall temperature and liquid saturation temperature, respectively,  $\theta$  is contact angle between Si and water, and  $q''_{\text{wall}}$  is effective wall heat flux on the cold-plate microchannel. For the flow rates of 0.03, 0.06 and 0.1 lit/min and at the maximum heat flux of 250 W/cm<sup>2</sup>, we estimate the  $T_{\text{heat,max}}$ ,  $T_{\text{cp-base,avg}}$  and  $T_{\text{f,out}}$  using the reduced order thermofluidic model detailed in [44], Figure B.1a. The estimated  $T_{\text{cp-base,avg}}$ ,  $T_{\text{heat,max}}$ ,  $T_{\text{f,out}}$  and the outlet saturation temperature,  $T_{\text{f,sat}}$  (a function of liquid pressure) are plotted in Figure B.1b. As the flow rate increases in the closed-loop flow system, the internal pressure also increases. Therefore,  $P_{\text{out}}$  and corresponding  $T_{\text{f,sat}}$  are ranging from 145.38 to 231.64 kPa, from 110.43 to 124.45 °C, respectively, as the fluid flow rate increases from 0.03 to 0.1 lit/min. According to the temperature information in Figure B.1b,  $T_{\text{f,sat}}$  is always higher than  $T_{\text{cp-base,avg}}$  in all the experimental results, and as a matter of fact, the necessary condition for the on-set of nucleate boiling in Eqn. B.9 is not satisfied. Therefore, we can conclude that the fluid remained single-phase at all times.

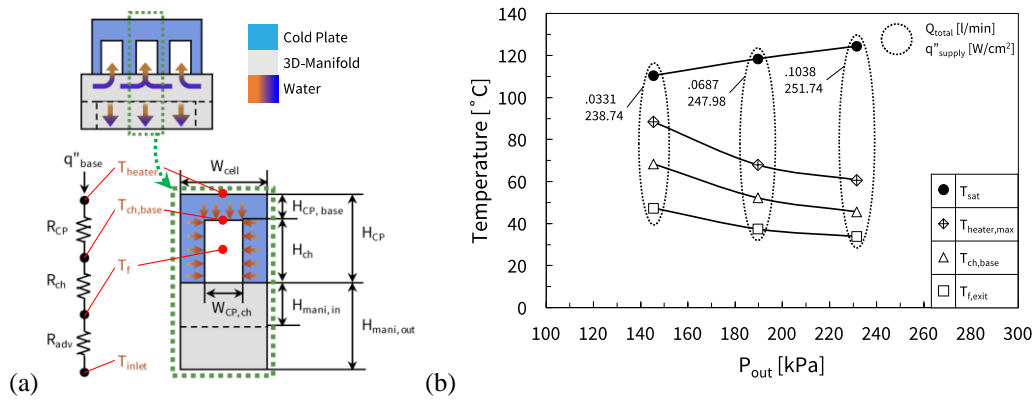


**Figure B. 1** (a) A simplified heat conduction pathway in the embedded microchannel with 3-D manifold heat exchanger and (b) Temperature vs  $P_{out}$  for single-phase water test case at the maximum heat flux 250 W/cm<sup>2</sup>.

We also utilized Eqn. B.9 to explore the maximum heat flux that the current embedded microchannel-3D manifold  $\mu$ -cooler using single-phase water. If the predictions of Eqn. B.9 for the onset of boiling is accurate, the present  $\mu$ -cooler can potentially remove up to 850 W/cm<sup>2</sup> (numerical simulations:  $T_{heater,max} = 158$  °C) with only 2.6 kPa pressure drop for flow rate of 0.1 l/min, see Figure B.2.

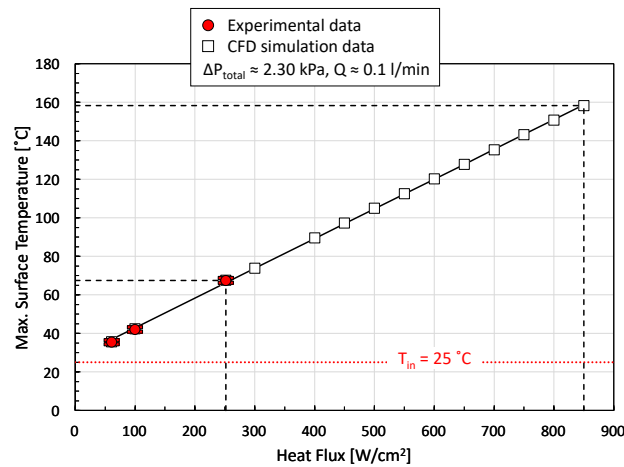


**Figure B. 2** Experimental data and CFD modeling results for single-phase water at inlet temperature  $\sim 25$  °C using a typical embedded microchannel with 3D manifold  $\mu$ -cooler developed at Stanford. The experimental data are for heat flux < 250 W/cm<sup>2</sup>. The CFD simulations are conducted to explore the feasibility of single-phase cooling at much higher heat fluxes; the onset of boiling occurs at 850 W/cm<sup>2</sup> to be verified experimentally. For water at inlet temperature of 25 °C, heat dissipation levels up to 500 W/cm<sup>2</sup> is feasible for target junction temperature of 100 °C.

For R-245fa, we have calculated the onset of nucleate boiling at each test condition by using the ONB correlation from Ref. [73]. The shift in the inlet pressure with the changed flow rate is taken into account for the estimation. The estimated ONB points show good agreement with the visual inspection points in Figure B.3. The uncertainty bar size is mainly attributed to the uncertainty of average heated surface temperature. The measured maximum surface temperature is not used in the ONB estimation because they are local hotspots at the center and the heat is spread through thick Si bulk layer, 425  $\mu\text{m}$ , that has isometric thermal conductivity of 130 W/m-K. The estimation matches well with the visually inspected ONB points.

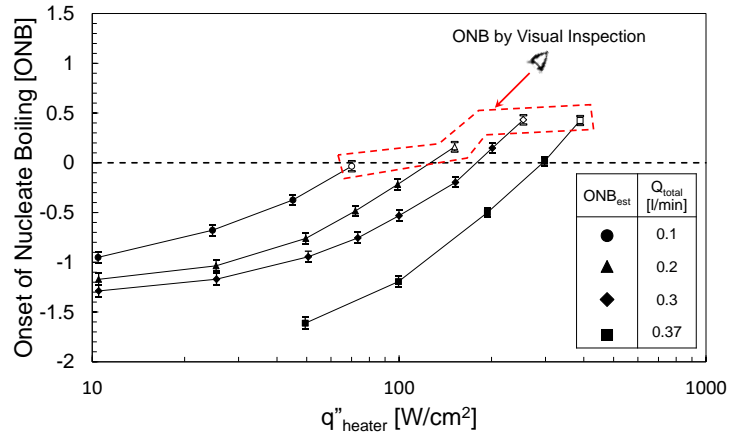


**Figure B. 3** Estimation of onset-of-nucleate boiling points for each test case, ONB estimation vs. supplied heat flux at given flow rates. The dashed line indicates the threshold for ONB by the correlation [73] and the open markers designate the empirically captured ONB moments.

### B.3 Estimation of pressure drop and its uncertainty in EMMC

*Refer Section 5.2.2.3:* Jung, et al. [43] used a conjugate CFD simulation tool to predict the fluid pattern inside the test system and they reported that the experimental results agreed well with the CFD simulation results within the allowable uncertainty of the pressure drop. If we assume that the working fluid is uniformly distributed across the manifold inlet conduits, we can calculate the fluid velocity at the beginning and end of the gradual contraction region,  $v_1$ , and  $v_2$ , respectively (Table 5.5).

$$\frac{P_1}{\rho_{in}g} + \gamma \cdot \frac{v_1^2}{2g} = \frac{P_2}{\rho_{in}g} + \gamma \cdot \frac{v_2^2}{2g} + h_{gc}, h_{gc} = K_{gc} \cdot \frac{v_2^2}{2g} \quad (\text{B.11})$$

$$\Delta P_{2,est} = P_1 - P_2 = \gamma \cdot \frac{\rho_{in}(v_2^2 - v_1^2)}{2} + \rho_{in}g \cdot h_{gc} \quad (B.12)$$

$$\Delta P_{3,est} \cong \phi \cdot \Delta P_{total} - \Delta P_2, \phi = 0.95 \quad (B.13)$$

where  $\rho_{in}$  is the fluid density at the inlet fluid temperature,  $\gamma$  is the kinetic energy correction factor, 1.15 – 1.22,  $h_{gc}$  is the hydraulic head loss due to the gradual contraction,  $K_{gc}$  is the coefficient of gradual contraction resistance, 5.5E-2 [74],  $v_1$ ,  $P_1$ , are the fluid velocity and pressure at the beginning of the gradual contraction region,  $v_2$ ,  $P_2$  are the fluid velocity and pressure at beginning of the active cooling region.  $\phi$  is introduced in Eqn. A-3, representing the contribution of  $\Delta P_{2,est}$  and  $\Delta P_{3,est}$  to  $\Delta P_{total}$  which is assumed as 95 %. The kinetic energy correction factor,  $\gamma$ , is 2 if the flow is fully-developed, and laminar. If the flow is fully-developed, and turbulent,  $\gamma$  is close to 1 [75]. By utilizing Eqn. B.11 through B.13, we can roughly estimate the pressure drop within the gradual contraction regions,  $\Delta P_{2,est}$ , and the pressure drop within the active cooling region,  $\Delta P_{3,est}$  (Figure 5.24). In Figure 5.24,  $\Delta P_{2,est}$  changes linearly, but  $\Delta P_{3,est}$  parabolically changes as the flow rate increases. The estimated fluid velocities, the Reynolds numbers, and the pressure drop information are given in Table 5.5.

$$(U_{\Delta P_{2,est}})^2 = \rho_{in}^2 \cdot \left[ (\gamma \cdot v_1 \cdot U_{v_1})^2 + \{(\gamma + K_{gc}) \cdot v_2 \cdot U_{v_2}\}^2 + \left(\frac{v_2^2}{2} \cdot U_{K_{gc}}\right)^2 + \left(\frac{v_2^2 - v_1^2}{2} \cdot U_{\gamma}\right)^2 \right] \quad (B.14)$$

$$(U_{\Delta P_{3,est}})^2 = (\Delta P_{total} \cdot U_{\phi})^2 + (\phi \cdot U_{\Delta P_{total}})^2 + (U_{\Delta P_{2,est}})^2 \quad (B.15)$$

where the sources of the uncertainty calculation in Eqn. B.14, B.15 are given in Table B.1.

**Table B. 1** Sources to estimate the uncertainties of  $\Delta P_{2,est}$ ,  $\Delta P_{3,est}$

Components	Affected Parameters	Accuracy
Kinetic Energy Correction Factor, $\gamma$	$\Delta P_{2,est}$	$\pm 5 \%$
Gradual Contraction Resistance Coefficient, $K_{gc}$	$\Delta P_{2,est}$	$\pm 5 \%$
Proportion of $(\Delta P_2 + \Delta P_3)$ to $\Delta P_{total}$ , $\phi$	$\Delta P_{3,est}$	$\pm 5 \%$
Fluid Velocities, $v_1$ , $v_2$	$\Delta P_{2,est}$ , $\Delta P_{3,est}$	$\pm 5 \%$

# Appendix C

## C.1 Study of nonlinear Joule-heating effect

Nonlinear Joule-heating effect has been studied by COMSOL Multiphysics 5.3. A gold serpentine heater with the same dimension of the actual heater is defined on top of Si bulk in the simulation. In Figure C.1, the temperature-dependent electric resistivity is defined in the sample on the left side, the temperature-independent electric resistivity is defined in the other sample. The resistivity value of gold is referred from Ref. [76].

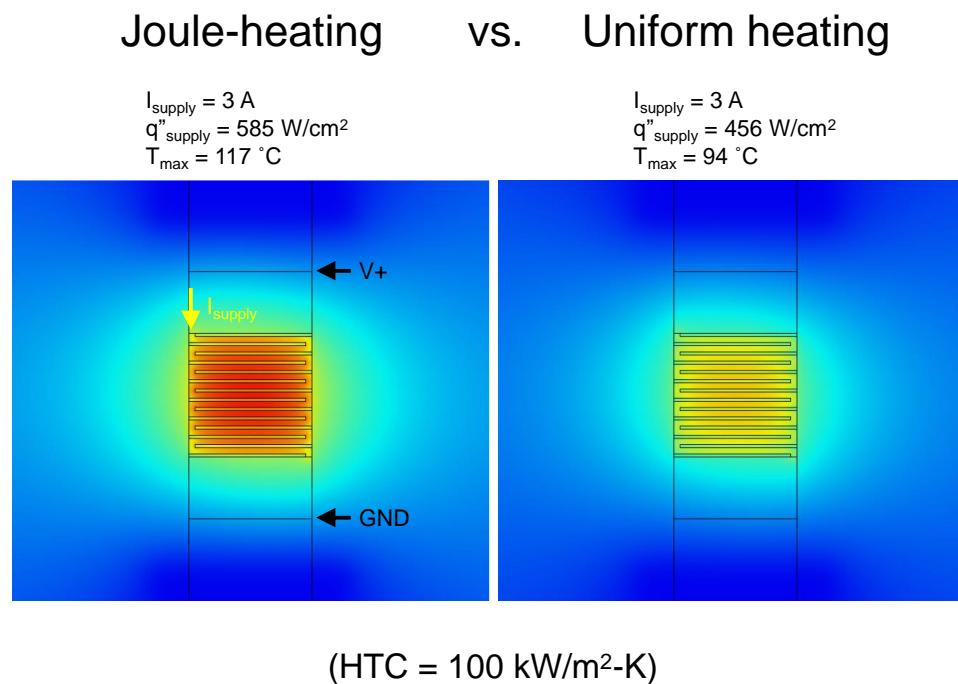


**Figure C. 1** Comparison between Joule-heating case vs. uniform heating case, natural convection is assumed on top surface, forced convection with HTC = 100 kW/m<sup>2</sup>-K is assumed at the bottom surface of the hotspot.

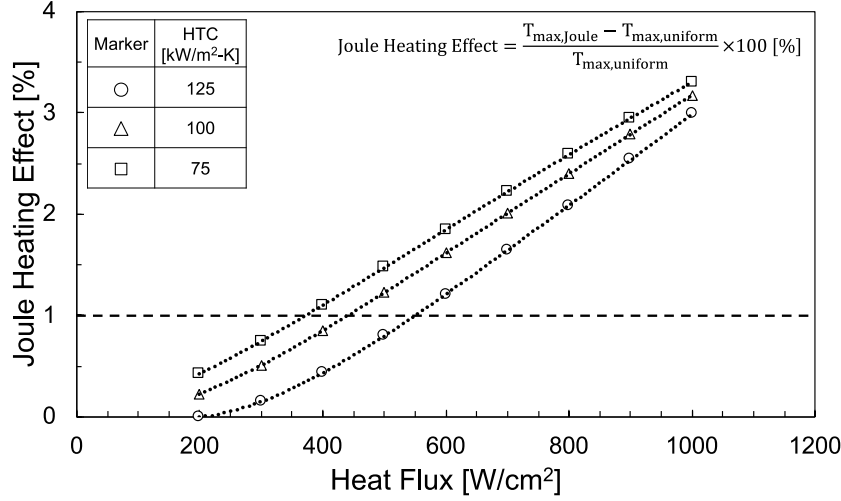


**Figure C. 2** Comparison between Joule-heating case vs. uniform heating case, natural convection is assumed on top surface, forced convection with  $\text{HTC} = 100 \text{ kW/m}^2\text{-K}$  is assumed at the bottom surface of the hotspot.

The size of electric current is same for two cases in Figure C.1, however, the supplied heat to the heater is different due to change in the heater's resistance in the left-side heater. With these two simulation models, multiple heat fluxes are tested in both models and Joule heating effect is calculated for all test cases (Figure C.2). Three different heat transfer coefficients, 75, 100, 125  $\text{kW/m}^2\text{-K}$ , are applied to the bottom of the hotspot in the simulation models, and the natural convection is assumed to the top surface.

The Joule heating effect,  $J$ , is expressed as:

$$J = \frac{T_{\max,\text{Joule}} - T_{\max,\text{uniform}}}{T_{\max,\text{uniform}}} \quad (\text{C.1})$$

where  $T_{\max,\text{Joule}}$  is the maximum surface temperature of the model with nonlinear Joule heating, and  $T_{\max,\text{uniform}}$  is the maximum surface temperature of the model with uniform heating. In Figure C.2,  $J$  keeps increasing as the heat flux increases and it reaches to 3.0 – 3.3 % at the heat flux of 1000  $\text{W/cm}^2$ .

# Appendix D

## D.1 Mesh independence study of the conjugate numerical simulations

A mesh size independence study is conducted in multiple EMMC designs with various number of mesh elements, and the relevant results are listed in Table D.1. The number of mesh elements keeps increasing until the change in  $R_{total}$  and  $\Delta P_{total}$  is less than 1 %. We would like to emphasize that  $q_{trans}$  was used in calculation of the  $R_{total}$ , see Eqn. 4.8a, and while the changes in this parameter was less than 1%, an overall energy balance ( $q_{supply} - q_{trans}$ ) between  $q_{supply}$  (supplied by heater as B.C.) and  $q_{trans}$  (transferred to liquid) calculated from Eqn. 4.7, is less than 3 % of  $q_{supply}$ . This could be due to error associated with integration in Eqn. 4.7. In any case, we take the relative stability of  $R_{total}$  and  $\Delta P_{total}$  values at 1 % as the convergence criteria and accept 3% error in calculation error of  $q_{trans}$  and therefore  $R_{total}$ .

**Table D. 1** Mesh independence study for different EMMC designs (D4, D7)

Parameters \ Design	D4				D7			
	$q''_{supply} = 800 \text{ W/cm}^2$				$q''_{supply} = 800 \text{ W/cm}^2$			
Full-scale Mesh Elements	14.3M	18.9M	24.3M	33.5M	14.9M	19.0M	23.1M	26.8M
$T_{heater,avg}$ [°C]	102.9	102.9	102.6	102.4	78.0	77.8	77.7	77.6
$R_{total}$ [cm <sup>2</sup> -K/W]	.0974	.0974	.0970	0.0968	.0663	.0660	.0659	.0658
$\Delta P_{total}$ [kPa]	7.8	7.9	8.1	8.2	7.9	8.0	8.0	8.0

We have conducted the mesh size dependence study with three different EMMC designs (D4, D7) because the necessary number of mesh elements for the independence highly relies on the size of small features such as the hydraulic diameter of CP microchannels.

There are less than 0.16 – 0.36 % change in the total thermal resistance and 0.34 – 0.64 % change in the total pressure drop if the number of mesh element is higher than

24.3E6, 23.1E6 in D4, D7, respectively. Table D.2 describes the important meshing input parameters to mesh D4 and D7. For the integrity of the current paper’s subject, the results of mesh independence study with another EMMC designs are not included in this paper. However, the EMMC designs similar to or more complicated than D8 and D9 have gone through the mesh independence study, and the results revealed that more than 50 millions of mesh elements for D8 and D9 should be sufficient for the convergence of the CFD simulations. We have used 50.0E6 and 69.2E6 mesh elements for the CFD simulations with D8 and D9, respectively.

**Table D. 2** Important input/output parameters for meshing

<b>Design</b>	<b>D4</b>				<b>D7</b>			
<b>Input Parameters</b>								
Sizing Growth Rate	1.075	1.06	1.05	1.04	1.07	1.058	1.05	1.04
Sizing Max Size	1.024E-3 m				1.024E-3 m			
Curvature Min Size	4E-6 m				4E-6 m			
Proximity Min Size	4E-6 m				4E-6 m			
Proximity Size Function Sources	Edges				Edges			
Assembly Meshing Method	CutCell				CutCell			
Inflation Option	Smooth Transition				Smooth Transition			
Inflation Transition Ratio	0.272				0.272			
Inflation Max Layers	5				5			
Inflation Growth Rate	1.2	1.2	1.15	1.15	1.12	1.09	1.08	1.07
<b>Output Parameters</b>								
Mesh Element Quality Min	1.49E-1	1.46E-1	1.49E-1	1.49E-1	1.48E-1	1.48E-1	1.02E-1	1.22E-1
Mesh Element Quality Max	1	1	1	1	1	1	1	1
Mesh Element Quality Avg	9.81E-1	9.85E-1	9.87E-1	9.89E-1	9.79E-1	9.81E-1	9.83E-1	9.84E-1
Mesh Element Quality STD	5.48E-2	4.86E-2	4.46E-2	4.04E-2	5.07E-2	4.80E-2	4.50E-2	4.34E-2
Number of Mesh Elements	14.3 M	18.9 M	24.3 M	33.5 M	14.9 M	19.0 M	23.1 M	26.8 M

## D.2 Additional information on Designs D4 to D9

Here are key CFD results related to Figure 4.5, see Table D.3:

**Table D. 3** Key CFD results (D4 – D9)

Design	$T_{\text{heater,avg}}$ [°C]	$R_{\text{total}}$ [cm <sup>2</sup> -K/W]	$T_{\text{heater,max}}$ [°C]	$R_{\text{total,max}}$ [cm <sup>2</sup> -K/W]	$T_{\text{f,in}}$ [°C]	$T_{\text{f,out}}$ [°C]	Hydraulic Diameter	Re number (μ-channel)
<b>D4</b>	102.6	0.097	112.8	0.11	25	39.6	100	170
<b>D5</b>	98.3	0.092	107.7	0.10	25	39.7	100	150
<b>D6</b>	85.7	0.076	91.5	0.083	25	39.6	100	150
<b>D7</b>	77.8	0.066	82.9	0.072	25	39.6	60	130
<b>D8</b>	60.0	0.044	62.5	0.047	25	39.2	17.6	92
<b>D9</b>	57.6	0.041	59.9	0.044	25	39.2	17.6	46

The hydraulic diameters of designs D4 to D9 ranges from 100 to 20 μm, which is comparable to values from literature: 100 μm [46], 72 μm [48], 33.3 – 113 μm [49], and 36.4 – 114 μm [53], but much larger than those reported 9.40 – 14.0 μm in reference [39].

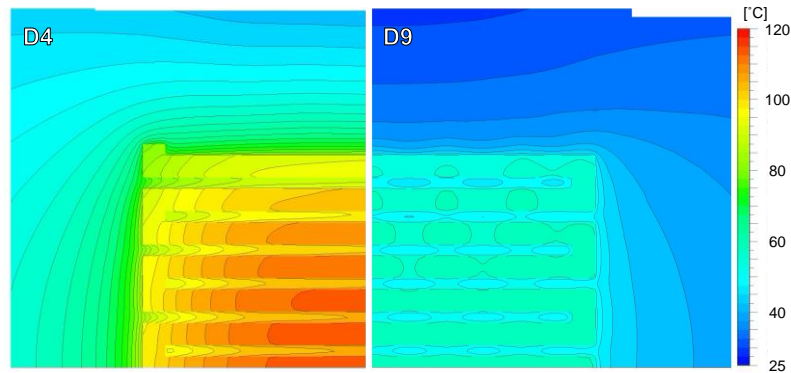


**Figure D. 1** Temperature distributions at the top of the micro-cooler (quarter) designs D4 and D9.

Figure D.1 depicts the temperature distributions at the top surface of the micro-coolers designs D4 and D9. The inner square shows the heated section where the serpentine patterns reflects the heat flux boundary condition imposed by a serpentine heater. The hottest location is at the center of the chip while the temperature drops

sharply outside of the heated square section. Temperature inside the heated square is influenced by the heat transfer coefficient and lateral conduction in the silicon chip, while outside only heat is transferred by conduction in silicon substrate.

### D.3 Discussion of thermo-fluidic behavior in D5 and D6

To further examine the problem, we introduce the general form of energy equation for steady, incompressible flow [75]:

$$\frac{P_1}{\rho g} + \alpha \frac{v_1^2}{2g} = \frac{P_2}{\rho g} + \alpha \frac{v_2^2}{2g} + h_{gc} \quad (D.1)$$

$$\Delta P_2 = P_1 - P_2 = \alpha \frac{\rho(v_2^2 - v_1^2)}{2} + \rho g \cdot h_{gc} \quad (D.2)$$

where  $\alpha$  is the kinetic energy correction factor for the general form of the energy equation,  $\rho$  is the density of the fluid (constant before active cooling region),  $h_{gc}$  is the head loss due to the gradual contraction between zone 1 and zone 2,  $v_1$  and  $v_2$  are average fluid velocity at zone 1 and 2, respectively. Since the contribution of  $\rho g \cdot h_{gc}$  is less than 5 % to the  $\Delta P_2$ , the difference between  $v_2$  squared and  $v_1$  squared is the main contributor to the  $\Delta P_2$ . No geometric change is made to the inlet opening and the inlet plenum of D4 and D5, therefore,  $v_1$  remains constant and  $v_2$  is the only parameter that affects  $\Delta P_2$  in Eqn. D.2.

If we assume that the fluid is uniformly distributed to every manifold inlet conduit, a rough estimation of  $v_2$  is given by

$$Q_{\text{mani,in}} = \frac{Q_{\text{total}}}{2 \cdot N_{\text{mani,in}}} \quad (D.3)$$

$$v_2 = \frac{Q_{\text{mani,in}}}{W_{\text{mani,in}} \cdot H_{\text{mani,in}}} = \frac{Q_{\text{total}}}{2 \cdot N_{\text{mani,in}} \cdot W_{\text{mani,in}} \cdot H_{\text{mani,in}}} \quad (D.4)$$

where  $Q_{\text{total}}$  is the total mass flow rate in the EMMC,  $Q_{\text{mani,in}}$  is the mass flow rate per manifold inlet conduit,  $N_{\text{mani,in}}$ ,  $W_{\text{mani,in}}$ , and  $H_{\text{mani,in}}$  are the number of manifold inlet conduits, the width of manifold inlet conduit, and the height of manifold inlet conduit, respectively. If the  $W_{\text{mani,in}}$  is the only variable and other parameters are constant in Eqn.

D.4,  $v_2$  should decrease as  $W_{\text{mani,in}}$  increases. From D4 to D5,  $W_{\text{mani,in}}$  increases from 150 to 217  $\mu\text{m}$ , therefore,  $v_2$  of D5 decreases from  $v_2$  of D4.

As a result, the decreased  $\Delta P_2$  in D5 is attributed to the increased  $W_{\text{mani,in}}$  based on Eqn. D.1 through Eqn. D.4. In order to test the validity of Eqn. D.3 and D.4, the ratio between  $v_{2,D4}$  and  $v_{2,D5}$  are calculated and they are given as below:

$$\left(\frac{v_{2,D5}}{v_{2,D4}}\right)_{\text{est}} = \frac{(W_{\text{mani,in}})_{D4}}{(W_{\text{mani,in}})_{D5}} \cong 0.69 \quad (\text{D.5})$$

That is very close to the CFD simulation result,

$$\left(\frac{v_{2,D5}}{v_{2,D4}}\right)_{\text{CFD}} = \frac{1.84 \frac{\text{m}}{\text{s}}}{2.65 \frac{\text{m}}{\text{s}}} \cong 0.69 \quad (\text{D.6})$$

This means that the assumption for Eqn. D.3, D.4, the uniform distribution of the fluid across the manifold inlet conduits, is valid.

In order to complete the discussion regarding the change in  $\Delta P_2$  affected by the change of  $W_{\text{mani,in}}$ , we rewrite the Eqn. D.2 to calculate the ratio of  $\Delta P_2$  in D4 and D5:

$$\begin{aligned} \left(\frac{\Delta P_{2,D5}}{\Delta P_{2,D4}}\right)_{\text{CFD}} &= \frac{2409.58 \text{ Pa}}{5357.95 \text{ Pa}} \cong 0.45, \\ \left(\frac{\Delta P_{2,D5}}{\Delta P_{2,D4}}\right)_{\text{est}} &\cong \left[\frac{(v_2^2 - v_1^2)_{D5}}{(v_2^2 - v_1^2)_{D4}}\right]_{\text{est}} = \frac{1.83^2 - 0.49^2}{2.65^2 - 0.49^2} \cong 0.46 \end{aligned}$$

which shows that the estimated and CFD simulation results for the ratio of  $\Delta P_2$  is close, therefore, one can conclude that the change in  $W_{\text{mani,in}}$  affects the change in  $\Delta P_2$ .

In addition to the decreased  $v_2$  in D4 and D5, the wall thickness between the manifold inlet/outlet conduits,  $W_{\text{mani,wall}}$ , is doubled in D4 and D5. Since the frictional pressure drop is linearly proportional to the fluid travel length, and proportional to the average fluid velocity squared, the combined effects reduce the pressure drop,  $\Delta P_3$ , within the active cooling region, by 3.5% for D5 to D4 design (Figure 4.6a).

The changed  $R_{\text{total}}$  is nearly identical to the changed  $R_{\text{comp}}$  and it means that the average surface temperature of the heater decreases while the average exit fluid temperature is maintained (Eqn. 4.8b).  $L_{\text{flow}}$  is defined by  $N_{\text{mani,in}}$  and remains constant, so  $W_{\text{mani,wall}}$  is the parameter that determines the amount of bypassed fluid between the

manifold inlet/outlet conduits. As  $W_{\text{mani,wall}}/L_{\text{flow}}$  in D5 is doubled from D4, the amount of bypassed fluid is reduced. Therefore, improvement in  $R_{\text{total}}$  in D5 is expected due to reduce  $R_{\text{comp}}$ .

## D.4 Further discussion of frictional pressure drop in CP microchannles (D6 – D9)

According to the general frictional pressure drop equation for straight channels [62],  $\Delta P_{\text{friction}}$  across the CP microchannels is inversely proportional to  $D_{\text{h,cp}}$ , and proportional to friction factor,  $f_f$ , and mass flux squared,  $G_{\text{cp}}^2$ . If we assume constant fluid thermophysical property and uniform flow distribution in microchannel, then

$$\begin{aligned} \left( \frac{\Delta P_{\text{friction,D7}}}{\Delta P_{\text{friction,D6}}} \right)_{\text{est}} &\sim \frac{D_{\text{h,cp,D6}} \cdot f_{f,D7} \cdot G_{\text{cp,D7}}^2}{D_{\text{h,cp,D7}} \cdot f_{f,D6} \cdot G_{\text{cp,D6}}^2} \cong 5.91 \\ \left( \frac{\Delta P_{\text{friction,D8}}}{\Delta P_{\text{friction,D7}}} \right)_{\text{est}} &\sim \frac{D_{\text{h,cp,D7}} \cdot f_{f,D8} \cdot G_{\text{cp,D8}}^2}{D_{\text{h,cp,D8}} \cdot f_{f,D7} \cdot G_{\text{cp,D7}}^2} \cong 40.08 \\ \left( \frac{\Delta P_{\text{friction,D9}}}{\Delta P_{\text{friction,D8}}} \right)_{\text{est}} &\sim \frac{D_{\text{h,cp,D8}} \cdot f_{f,D9} \cdot G_{\text{cp,D9}}^2}{D_{\text{h,cp,D9}} \cdot f_{f,D8} \cdot G_{\text{cp,D8}}^2} \cong 0.5 \end{aligned} \quad (\text{D.7})$$

Compared to the CFD simulations results

$$\begin{aligned} \left( \frac{\Delta P_{3,D7}}{\Delta P_{3,D6}} \right)_{\text{CFD}} &\cong 2.28, \\ \left( \frac{\Delta P_{3,D8}}{\Delta P_{3,D7}} \right)_{\text{CFD}} &\cong 15.22, \\ \left( \frac{\Delta P_{3,D9}}{\Delta P_{3,D8}} \right)_{\text{CFD}} &\cong 0.45 \end{aligned} \quad (\text{D.8})$$

While the estimated values from Eqn. D.7 are different form the CFD simulation results (Eqn. D.8) but the trend is consistent with the results in Figure 4.8. Since the motion of the fluid within the CP microchannel is complicated, a more careful investigation is required to characterize the effect of CP microchannel's shape factor on the  $\Delta P_3$ . The efforts presented in Eqn. D.7 give us a general idea of changing trends in  $\Delta P_3$  as the  $N_{\text{cp}}$  changes.

# Bibliography

- [1] List of CPU power dissipation figures,  
[https://en.wikipedia.org/wiki/List\\_of\\_CPU\\_power\\_dissipation\\_figures](https://en.wikipedia.org/wiki/List_of_CPU_power_dissipation_figures)
- [2] Fuller, S.H., Millett, L.I., National Research Council, 2011. The Future of Computing Performance: Game Over or Next Level?, National Academies Press.  
<https://doi.org/10.17226/12980>
- [3] Theis, T.N. and Solomon, P.M., “In quest of the “next switch”: prospects for greatly reduced power dissipation in a successor to the silicon field-effect transistor”, Proceedings of the IEEE, 98(12) (2010), pp. 2005-2014.
- [4] Report to the NSF on The Workshop for Energy-Efficient Computing 2015. April 14-15, 2015 at the Holiday Inn, Arlington, VA.
- [5] H.Y. Zhang, D. Pinjala, T.N. Wong, K. C. Toh, Y.K. Joshi, Single-Phase Liquid Cooled Microchannel Heat Sink for Electronic Packages, Applied Thermal Engineering 25 (2005) 1472–1487.
- [6] E. G. Colgan, B. Furman, M. Gaynes, W. Graham, N. LaBianca, J. H. Magerlein, J. R. Polastre, M. B. Rothwell, J. R. Bezama, R. Choudhary, K. Marston, H. Toy, J. Wakil, J. Zitz, R. Schmidt, A Practical Implementation of Silicon Microchannel Coolers for High Power Chips, Proc. 21st IEEE SEMI-THERM Symposium (2004) 1–7.
- [7] J. Lee, I. Mudawar, Low-temperature two-phase micro-channel cooling for high-heat-flux thermal management of defence electronics, IEEE Trans. Compon. Packag. Manuf. Technol. 32 (2009) 453–465.
- [8] J. Lee, I. Mudawar, Fluid Flow and Heat Transfer Characteristics of Low temperature Two-Phase Micro-Channel Heat Sinks—Part 1: Experimental methods and flow visualization results, Int. J. Heat Mass Transfer 51 (2008) 4315–4326.
- [9] D. Faulkner, M. Khotan, R. Shekarriz, Practical Design of a 1000 W/cm<sup>2</sup> Cooling System, Proc. 19th IEEE SEMI-THERM Symposium, San Jose, USA (2003) 223–230.
- [10] A. Kosar, C. -J. Kuo, Y. Peles, Boiling Heat Transfer in Rectangular Microchannels with Reentrant Cavities, Int. J. Heat Mass Transfer 48 (2005) 4867–4886.

- [11] K. H. Peters, F. A. Kulacki, Flow Boiling in Microchannels, Proc. Heat Transfer Conference and InterPACK '05, San Francisco, USA (2005) 861–870.
- [12] C. R. Kharangate, L. O'Neill, I. Mudawar, M.M. Hasan, H.K. Nahra, R. Balasubramaniam, N.R. Hall, A.M. Macner, J.R. Mackey, Effects of subcooling and two-phase inlet on flow boiling heat transfer and critical heat flux in a horizontal channel with one-sided and double-sided heating, *Int. J. Heat Mass Transfer* 91 (2015) 1187-1205.
- [13] I. Mudawar, Two-phase micro-channel heat sinks: theory, applications and limitations, *J. Electronic Packaging - Trans. ASME* 133 (2011) 041002.
- [14] H.J. Lee, S.Y. Lee, Heat transfer correlation for boiling flows in small rectangular horizontal channels with low aspect ratios, *Int. J. Multiphase Flow* 27 (2001) 2043-2062.
- [15] B. Agostini, A. Bontemps, Vertical flow boiling of refrigerant R134a in small channels, *Int. J. Heat Fluid Flow* 26 (2005) 296–306.
- [16] A. Cioncolini, J. R. Thome, Algebraic turbulence modeling in adiabatic and evaporating annular two-phase flow, *Int. J. Heat Fluid Flow* 32 (2011) 805–817
- [17] G. R. Warrier, V.K. Dhir, L.A. Momoda, Heat transfer and pressure drop in narrow rectangular channels, *Exp. Thermal Fluid Science* 26 (2002) 53–64.
- [18] K. E. Gungor, R. H. S. Winterton, A general correlation for flow boiling in tubes and annuli, *Int. J. Heat Mass Transfer* 29 (1986) 351–358.
- [19] H.K. Oh, C.H. Son, Flow boiling heat transfer and pressure drop characteristics of CO<sub>2</sub> in horizontal tube of 4.57-mm inner diameter, *Applied Thermal Engng* 31 (2011) 163–172.
- [20] S.M. Kim, I. Mudawar, Universal approach to predicting two-phase frictional pressure drop for mini/micro-channel saturated flow boiling, *Int. J. Heat Mass* 58 (2013) 718 – 734.
- [21] S-M. Kim, I. Mudawar, Universal approach to predicting saturated flow boiling heat transfer in mini/micro-channels – Part II. Two-phase heat transfer coefficient, *Int. J. Heat Mass*, 64 (2013).
- [22] I. Mudawar, T.M. Anderson, Optimization of extended surfaces for high flux chip cooling by pool boiling, *J. Electronic Packaging- Trans. ASME* 115 (1993) 89-100.
- [23] J. A. Shmerler, I. Mudawar, Local evaporative heat transfer coefficient in turbulent free-falling liquid films, *Int. J. Heat Mass Transfer* 31 (1988) 731-742.

- [24] W. M. Kays, A. L. London, Compact Heat Exchangers, New York: McGraw Hill (1984).
- [25] R. C. Chu, "Thermal Conduction Module," US Patent 4,226,281 (1980).
- [26] D. B. Tuckerman, R. F. W. Pease, High Performance Heat Sinking for VLSI, IEEE Electron Device Letters 2 (1981) 126-129.
- [27] C. B. Sobhan, S. V. Garimella, A Comparative Analysis of Studies on Heat Transfer and Fluid Flow in Microchannels, Microscale Thermophysical Engineering 5 (2001) 293-311.
- [28] L. Zhang, J.-M. Koo, L. Jiang, M. Asheghi, K. E. Goodson, J. G. Santiago, T. W. Kenny, Measurements and Modeling of Two-phase Flow in Microchannels with Nearly Constant Heat Flux Boundary Conditions, Journal of Microelectromechanical Systems 11 (2002) 12-19
- [29] A. Bejan, M. R. Errera, Deterministic Tree Networks for Fluid Flow: Geometry for Minimal Flow Resistance between a Volume and One Point, Fractals 5 (1997) 685.
- [30] S. M. Senn, D. Poulikakos, Laminar Mixing, Heat Transfer, and Pressure Drop in Tree-Like Microchannel Nets and their Application for Thermal Management in Polymer Electrolyte Fuel Cells, Journal of Power Sources 130 (2004) 178-191.
- [31] W. Escher, B. Michel, D. Poulikakos, Efficiency of Optimized Bifurcating Tree-Like and Parallel Microchannel Networks in the Cooling of Electronics, International Journal of Heat and Mass Transfer 52 (2009) 1421.
- [32] T. Baummer, E. Cetegen, M. Ohadi, S. Dessiatoun, Force-fed Evaporation and Condensation Utilizing Advanced Micro-structured Surfaces and Micro-channels, Microelectronics Journal 39 (2008) 975-980.
- [33] K. E. Goodson, C.-H. Chen, D. E. Huber, L. Jiang, T. W. Kenny, J.-M. Koo, D. J. Laser, J. C. Mikkelsen, J. G. Santiago, E. N.-Y. Wang, S. Zeng, L. Zhang, Electroosmotic Microchannel Cooling System, US Patent 6,942,018 (2005).
- [34] K. E. Goodson, T. W. Kenny, P. Zhou, G. Upadhyaya, M. Munch, M. McMaster, J. Hom, Method and Apparatus for Achieving Temperature Uniformity and Hot Spot Cooling in a Heat Producing Device, US Patent 7,104,312 (2006).
- [35] T. Kenny, M. Munch, P. Zhou, J. Shook, K. Goodson, D. Corbin, M. McMaster, J. Lovette, Method and Apparatus for Efficient Vertical Fluid Delivery for Cooling a Heat-Producing Device, US Patent 7,000,684 (2006).

- [36] T. Kenny, J.G. Shook, D. Corbin, M. Munch, K. E. Goodson, Method and Apparatus for Flexible Fluid Delivery for Cooling Desired Hot Spots in a Heat Producing Device, US Patent 6,988,534 (2006).
- [37] Lee, H., Agonafer, D.D., Won, Y., Houshmand, F., Gorle, C., Asheghi, M., Goodson, K.E., Thermal modeling of extreme heat flux microchannel coolers for GaN-on-SiC Semiconductor Devices, *J. Electron. Packag.* 138(1) (2016) 010907.
- [38] Drummond, K.P., Weibel, J.A., Garimella, S.V., Back, D., Janes, D.B., Sinanis, M.D., Peroulis, D., 2016, “Evaporative intrachip hotspot cooling with a hierarchical manifold microchannel heat sink array”, *Intersociety Conference on Thermal and Thermomechanical Phenomena in Electronic Systems (ITherm)*, pp. 307-315, 31 May – 3 June, Las Vegas, Nevada, USA.
- [39] Drummond, K.P., Back, D., Sinanis, M.D., Janes, D.B., Peroulis, D., Weibel, J.A., Garimella, S.V., 2018, Characterization of hierarchical manifold microchannel heat sink arrays under simultaneous background and hotspot heating conditions, *Int. J. Heat Mass Transf.* 126, pp. 1289–1301.
- [40] Cetegen, E., 2010, Force Fed Microchannel High Heat Flux Cooling Utilizing Microgrooved Surfaces, Ph.D., University of Maryland, College Park.
- [41] Jung, K.W., Harza, S., Kwon, H., Piazza, A., Jih, E., Asheghi, M., Gupta, M.P., Degner, M., Goodson, K.E., 2019, Design optimization of Silicon-based Embedded Microchannels and 3D-Manifold for High Heat Flux ( $> 1\text{ kW/cm}^2$ ) Power Electronics Cooling, *Proceedings of the ASME 2019 InterPACK Conference, IPACK2019-6400*, pp. V001T06A007, October 7 – 9, Anaheim, California, USA.
- [42] Zhou, F., Joshi, S.N., Liu, Y., Dede, E.M., 2019, Near-junction cooling for next-generation power electronics, *Int Commun Heat Mass* 108, pp. 104300-1 – 8.
- [43] Jung, K.W., Kharangate, C.R., Lee, H., Palko, J., Zhou, F., Asheghi, M., Dede, E.M., Goodson, K.E., 2019, Embedded Cooling with 3D Manifold for Vehicle Power Electronics Applications: Single-phase Thermal-fluid Performance, *Int. J. Heat Mass Transf.* 130, pp. 1108–1119.
- [44] Jung, K.W., Kharangate, C.R., Lee, H., Palko, J., Zhou, F., Asheghi, M., Dede, E.M., Goodson, K.E., Microchannel cooling strategies for high heat flux ( $1\text{ kW/cm}^2$ ) power electronic applications, *Thermal and Thermomechanical Phenomena in Electronic Systems (ITherm)*, 2017 IEEE ITherm Conference , pp. 98-105, 29 May–1 June, 2017.
- [45] Bello-Ochende, T., Meyer, J. P., and Ighalo, F., Combined numerical optimization and constructal theory for the design of microchannel heat sinks, *Numerical Heat Transfer, Part A: Applications*, 58 (11) (2010), pp. 882–899.

- [46] Scholl, S., Gorle, C., Houshmand, F., Lee, H., Liu, T., Won, Y., Kazemi, H., Asheghi, M., and Goodson, K., Numerical simulation of advanced monolithic microcooler designs for high heat flux microelectronics, Proceedings of the ASME 2015 InterPACK Conference, pp. V002T06A009, 6 June – 9 June, 2015.
- [47] Husain, A., and Kim, K.-Y., Optimization of a microchannel heat sink with temperature dependent fluid properties, Applied Thermal Engineering, 28 (8) (2008), pp. 1101 – 1107.
- [48] Andhare, R.S., Shooshtari, A., Dessiatoun, S.V., Ohadi, M.M., Heat transfer and pressure drop characteristics of a flat plate manifold microchannel heat exchanger in counter flow configuration, Appl. Therm. Eng. 96 (2016), pp. 178 – 189.
- [49] Arie, M.A., Shooshtari, A.H., Dessiatoun, S.V., Al-Hajri, E., Ohadi, M.M., Numerical modeling and thermal optimization of a single-phase flow manifold-microchannel plate heat exchanger, Int. J. Heat Mass Transf. 81 (2015), pp. 478 – 489.
- [50] Sharma, C.S., Tiwari, M.K., Michel, B., Poulikakos, D., Thermofluidics and energetics of a manifold microchannel heat sink for electronics with recovered hot water as working fluid, Int. J. Heat Mass Transf. 58 (2013), pp. 135 – 151.
- [51] Liu, D., Garimella, S.V., Analysis and optimization of the thermal performance of microchannel heat sinks, Int. J. Numer. Methods Heat Fluid Flow 15 (1) (2004), pp. 7 – 26.
- [52] Brunschwiler, T., Paredes, S., Drechsler, U., Michel, B., Cesar, W., Toral, G., Temiz, Y., Leblebici, Y., Validation of the porous-medium approach to model interlayer-cooled 3D-chip stacks, 2009 IEEE International Conference on 3D System Integration, San Francisco, CA, 2009, pp. 1-10.
- [53] Sarangi, S., Bodla, K.K., Garimella, S.V., Murthy, J.Y., Manifold microchannel heat sink design using optimization under uncertainty, Int. J. Heat Mass Transf. 69 (2014), pp. 92 – 105.
- [54] Solovitz, S.A., Mainka, J., Manifold design for micro-channel cooling with uniform flow distribution, J. Fluids Eng. 133 (5) (2011), pp. 051103-1 – 051103-11.
- [55] Jung, K.W., Cho, E., Lee, H., Kharangate, C., Zhou, F., Asheghi, M., Dede, E.M., Goodson, K.E., Thermal and Manufacturing Design Considerations for Silicon-Based Embedded Microchannel-3D Manifold Coolers (EMMCs): Part 1 – Experimental Study of Single-Phase Cooling Performance with R-245fa, Journal of Electronic Packaging (2020) (submitted).

- [56] Jung, K.W., Zhou, F., Asheghi, M., Dede, E.M., Goodson, K.E., Experimental study of single-phase cooling with DI water in an embedded microchannels-3D manifold cooler, 21<sup>st</sup> Electronics Packaging Technology Conference, Singapore, 4<sup>th</sup> – 6<sup>th</sup> December, 2019 (accepted).
- [57] Shah, R.K., London, A.L., Advances in Heat Transfer, Supplement 1: Laminar Flow Forced Convection in Ducts, Academic Press, New York (1978).
- [58] Harms, T.M., Kazmierczak, M.J., Gerner, F.M., Developing convective heat transfer in deep rectangular microchannels, *Int. J. Heat Fluid Flow* 20 (1999), pp. 149 - 157.
- [59] Nakamura, H., Matsuura, A., Kiwaki, J., Matsuda, N., Hiraoka, S., Yamada, I., The effect of variable viscosity on laminar flow and heat transfer in rectangular ducts, *J. Chem. Eng. Japan* (1979).
- [60] U. Grigull, H. Tratz, Thermischer einlauf in ausgebildeter laminarer rohrströmung. *Int. J. Heat Mass Transf.* 85, 669–678 (1965).
- [61] Bejan, A., Kraus, A.D., Heat transfer handbook, John Wiley & Sons (2003)
- [62] Incropera, F. P., Fundamentals of heat and mass transfer, John Wiley & Sons, 2011.
- [63] Schilder, B., Man, S.Y.C., Kasagi, N., Hardt, S., Stephan, P., Flow visualization and local measurement of forced convection heat transfer in a microtube, *J. Heat Transfer* 132(3) (2010) 031702.
- [64] Lee, J., Mudawar, I., Fluid flow and heat transfer characteristics of low temperature two-phase micro-channel heat sinks - Part 1: Experimental methods and flow visualization results, *Int. J. Heat Mass Transf.* 51 (2008), pp. 4315 - 4326.
- [65] Lee, J., Mudawar, I., Fluid flow and heat transfer characteristics of low temperature two-phase micro-channel heat sinks - Part 2. Subcooled boiling pressure drop and heat transfer, *Int. J. Heat Mass Transf.* 51 (2008), pp. 4327 - 4341.
- [66] Lee, J., Mudawar, I., Two-phase flow in high-heat-flux micro-channel heat sink for refrigeration cooling applications: Part II - heat transfer characteristics, *Int. J. Heat Mass Transf.* 48 (2005), pp. 941 - 955.
- [67] Sood, S., Advanced metal-eutectic bonding for high volume MEMS WLP, IEEE MEMS Bay Area Meeting, 24 Feb, 2014. ([http://site.ieee.org/scv-mems/files/2013/09/2014\\_2\\_26\\_IEEE-MEMS-Sood-Handouts.pdf](http://site.ieee.org/scv-mems/files/2013/09/2014_2_26_IEEE-MEMS-Sood-Handouts.pdf))
- [68] Jing, E., Xiong B., Wang, Y., Low-temperature Au-Si water bonding, *J. Micromech. Microeng.* Vol. 20 (2010) 095015

- [69] Matweb. (2015, 12/30). Titanium Ti-6Al-4V (Grade 5), STA. Available: <http://www.matweb.com!search!DataSheet.aspx?MatGUID=b350a78geda946c6b86a3e4d3c577b39>
- [70] [CTE2] G. A. Slack and S. F. Bartram, "THERMAL- EXPANSION OF SOME DIAMOND-LIKE CRYSTALS, " Journal of Applied Physics, vol. 46, pp. 89-98, 1975 1975.
- [71] Deisenroth, D.C., Raphael K. Mandel, Hannes Greve, Serguei V. Dessiatoun, Patrick McCluskey, Michael M. Ohadi, Direct bonding of a Titanium header to an Embedded Two-phase FEEDS Cooling Device for High-Flux Electronics, 15th IEEE ITherm conference (2016), pp. 1072 - 1077.
- [72] Kline, S. J., McClintock, F. A., Describing Uncertainties in Single-Sample Experiments, Mech. Eng., p. 3, January 1953.
- [73] Liu, D., Lee, P-S, Garimella, S.V., 2005, Prediction of the onset of nucleate boiling in microchannel flow, Int. J. Heat Mass Transf. 48, pp. 5134–5149.
- [74] Mott, R.L., Untener, J.A., 2014, Applied Fluid Mechanics (7th edition), Pearson Education, Inc
- [75] Cengel, Y.A., Cimbala, J.H., Fluid Mechanics, McGRAW-HILL, 2006.
- [76] Matula, R.A., Electrical resistivity of copper, gold, palladium, and silver, J. PHYS. CHEM. REF. DATA 8 (1979), pp. 1147 – 1298.
- [77] Ohadi, M., Choo, K., Dessiatoun, S., Cetegen, E., Next generation microchannel heat exchangers, Springer (2013).
- [78] Besler, R.B., Hicklin, W.H., Temperature coefficients of resistance of metallic films in the temperature range 25°C to 600 °C, J. APPL. PHYS. 30(313) (1959), pp. 313 – 322.